ABSTRACT

Title of dissertation: COARSE GRAINING TO INVESTIGATE PEPTIDE-LIPID INTERACTIONS

Sai Janani Ganesan, Doctor of Philosophy, 2016

Dissertation directed by: Dr. Silvina Matysiak, Assistant Professor
Fischell Department of Bioengineering

Experimental characterization of molecular details is challenging, and although single molecule experiments have gained prominence, oligomer characterization remains largely unexplored. The ability to monitor the time evolution of individual molecules while they self assemble is essential in providing mechanistic insights about biological events. Molecular dynamics (MD) simulations can fill the gap in knowledge between single molecule experiments and ensemble studies like NMR, and are increasingly used to gain a better understanding of microscopic properties. Coarse-grained (CG) models aid in both exploring longer length and time scale molecular phenomena, and narrowing down the key interactions responsible for significant system characteristics. Over the past decade, CG techniques have made a significant impact in understanding physicochemical processes. However, the realm of peptide-lipid interfacial interactions, primarily binding, partitioning and folding of amphipathic peptides, remains largely unexplored compared to peptide folding in solution. The main drawback of existing CG models is the inability to capture environmentally sensitive changes in dipolar interactions, which are indigenous to protein folding, and lipid dynamics.

We have used the Drude oscillator approach to incorporate structural polarization and dipolar interactions in CG beads to develop a minimalistic peptide model, WEPPROM (Water Explicit Polarizable PROtein Model), and a lipid model WEPMEM (Water Explicit Polarizable MEmbrane Model). The addition of backbone dipolar interactions in a CG model for peptides enabled us to achieve α/β secondary structure content *de novo*, without any added bias. As a prelude to studying amphipathic peptide-lipid membrane interactions, the balance between hydrophobicity and backbone dipolar interactions in driving ordered peptide aggregation in water and at a hydrophobic-hydrophilic interface, was explored. We found that backbone dipole interactions play a crucial role in driving ordered peptide aggregation, both in water and at hydrophobic-hydrophilic interfaces; while hydrophobicity is more relevant for aggregation in water. A zwitterionic (POPC: 1-palmitoyl-2-oleoyl-*sn*-glycero-3-phosphocholine) and an anionic lipid (POPS: 1-palmitoyl-2-oleoyl-*sn*-glycero-3-phospho-L-serine) are used as model lipids for WEPMEM. The addition of head group dipolar interactions in lipids significantly improved structural, dynamic and dielectric properties of the model bilayer.

Using WEPMEM and WEPPROM, we studied membrane-induced peptide folding of a cationic antimicrobial peptide with anticancer activity, SVS-1. We found that membrane-induced peptide folding is driven by both (a) cooperativity in peptide self interaction and (b) cooperativity in membrane-peptide interactions. The dipolar interactions between the peptide and the lipid head-groups contribute to stabilizing folded conformations. The role of monovalent ion size and peptide concentration in driving lipid domain formation in anionic/zwitterionic lipid mixtures was also

investigated. Our study suggest monovalent ion size to be a crucial determinant of interaction with lipid head groups, and hence domain formation in lipid mixtures. This study reinforces the role of dipole interactions in protein folding, lipid membrane properties, membrane induced peptide folding and lipid domain formation. Therefore, the models developed in this thesis can be used to explore a multitude of biomolecular processes, both at longer time-scales and larger system sizes.

COARSE GRAINING TO INVESTIGATE PEPTIDE-LIPID INTERACTIONS

by

Sai Janani Ganesan

Dissertation submitted to the Faculty of the Graduate School of the
University of Maryland, College Park in partial fulfillment
of the requirements for the degree of
Doctor of Philosophy
2016

Advisory Committee:
Dr. Silvina Matysiak, Chair/Advisor
Dr. Jose Helim Aranda-Espinoza
Dr. Robert Blumenthal
Dr. Jeffery Klauda
Dr. Garegin Papoian
Dr. Joel P. Schneider

© Copyright by
Sai Janani Ganesan
2016

To Ganesan, Indra Ganesan, Lalitha Ganesan

Visalakshi Ganesan and Preethi Mahalingam.

Acknowledgments

I started graduate school not knowing what it meant to do science or to be successful at it. Over the course of my graduate studies, I have not just learnt how to conduct research and think about scientific questions, but also many essential life lessons that has made me a better person. I would like to thank everyone who has made my graduate school life enjoyable.

I would like to thank my advisor, Dr. Silvina Matysiak for her patience when I failed, support and encouragement through days of unsuccessful research, and for always being available for help and advice; I couldn't have asked more from an advisor. I would like to thank my committee members, Dr. Jose Helim Aranda-Espinoza, Dr. Robert Blumenthal, Dr. Garegin Papoian, Dr. Jeffery Klauda and Dr. Joel P. Schneider, for making themselves available, and for very many valuable discussions over the years.

I would like to thank UMD-NCI partnership and the Graduate Dean's fellowship for funding my research.

I would like to thank my lab-mates, past and present; Gregory Custer, Hongcheng Xu, Anu Nagarajan, Sudi Jawahery, Matt Eckler, Michael McCutchen, Libet Garber, Anastasiya Balyaeva, Danielle Rothermel, and David Peeler; all of whom have immensely contributed to making my graduate school life enjoyable. I can't imagine getting through graduate school without their help, advice, encouragement and valuable input.

I owe a lot to friends and family who have supported me through this process.

I want to thank my parents, Ganesan and Indra Ganesan, for teaching me about integrity, dedication, and perseverance; my aunt, Visalakshi, for being the first to inspire me to learn, to question and to think; and my sisters Lalitha and Preethi, for patiently listening to my graduate school stories only to offer more encouragement and support.

Table of Contents

List of Tables viii

List of Figures ix

List of Abbreviations xix

1 Introduction and Outline of Thesis 1
1.1 Outline of Thesis . . . 5

2 Role of Dipole Interactions in the Formation of Secondary and Super-secondary Protien Structures 8
2.1 Overview . . . 8
2.2 Introduction . . . 8
2.3 Methods . . . 10
2.3.1 Overview . . . 10
2.3.2 Forcefield Parameters . . . 12
2.3.3 Simulation Setup . . . 14
2.3.4 Electrostatic field . . . 15
2.4 Results and Discussion . . . 17
2.4.1 Role of Helix Capping . . . 17
2.4.2 Supersecondary Structures . . . 22
2.4.2.1 Helix Bundles . . . 22
2.4.2.2 Sheet Bundles . . . 28
2.5 Conclusions . . . 30

3 Interplay Between Dipole Interactions and Hydrophobicity In Peptide Aggregation At Interfaces 32
3.1 Overview . . . 32
3.2 Introduction . . . 32
3.3 Methods . . . 36
3.3.1 System Setup . . . 36
3.3.2 Simulation Setup . . . 37
3.3.3 Analysis . . . 38

3.3.3.1 Order Parameter. . . . 38
3.3.3.2 Dipole Moment and Energy. . . . 40
3.3.3.3 Pseudo Hydrogen Bonds. . . . 40
3.3.3.4 Water Expulsion. . . . 42
3.3.3.5 Conformational Analysis and Kinetics. . . . 42
3.3.3.6 Potential Mean Force. . . . 44
3.4 Results and Discussion . . . 44
3.4.1 Effect of Concentration . . . 44
3.4.2 Energetic Contributions and Role of Water . . . 48
3.4.3 Mechanisms of Water Expulsion . . . 52
3.4.4 Effect of Water-Hydrophobic Liquid Interface . . . 54
3.4.5 Pathways of Peptide Aggregation on Hydrophobic Interface . . . 57
3.4.6 Kinetics and Mechanism of Aggregation . . . 59
3.4.7 Role of Dipole Interactions . . . 63
3.5 Conclusion . . . 67

4 Effect of Lipid Head Group Interactions in Membrane Properties and Membrane-Induced Cationic β-Hairpin Folding 71
4.1 Overview . . . 71
4.2 Introduction . . . 71
4.3 Methods . . . 74
4.3.1 Lipid Model . . . 74
4.3.2 Lipid Force Field Parameters . . . 77
4.3.3 Peptide Model . . . 79
4.3.4 Simulation Setup . . . 80
4.3.5 Analysis Methods . . . 84
4.3.5.1 Calculation of Standard Errors . . . 84
4.3.5.2 Density Distribution . . . 85
4.3.5.3 Susceptibility Profile . . . 85
4.3.5.4 Line Tension . . . 86
4.3.5.5 Bilayer Potential . . . 87
4.3.5.6 Cluster Analysis . . . 87
4.3.5.7 Ion Bridge Connectivity . . . 90
4.4 Results and Discussion . . . 90
4.4.1 Structural and Dynamic Membrane Properties . . . 90
4.4.2 Membrane-Induced SVS-1 Folding . . . 104
4.5 Conclusion . . . 122

5 Effect of Monovalent Ion Size on Lipid Domain Formation in Anionic-Zwitterionic Lipid Mixtures 126
5.1 Overview . . . 126
5.2 Introduction . . . 126
5.3 Methods . . . 128
5.3.1 System Setup . . . 128
5.3.2 Simulation Parameters . . . 129

5.3.3 Analysis . . . 130
5.4 Results and Discussions . . . 130
5.4.1 Effect of Ion Size on Cluster Formation . . . 130
5.4.2 Effect of Ion Size on Bilayer Structure Properties . . . 134
5.4.3 Mechanism of Lipid Cluster Formation . . . 136
5.5 Conclusion and Future Work . . . 141

6 Effect of SVS-1 Concentration on POPC and POPS Lipids 142
6.1 Overview . . . 142
6.2 Introduction . . . 142
6.3 Methods . . . 144
6.3.1 System Setup and Simulation Protocol . . . 144
6.4 Results and Discussion . . . 145
6.4.1 Bilayer Simulations . . . 145
6.4.2 Self Assembly Simulations . . . 148
6.5 Conclusion and Future Work . . . 153

7 Thesis Summary 156

A Simulation Parameters 159
A.0.1 Simulation Parameters . . . 159

Bibliography 160

List of Tables

2.1 System Sizes 13
2.2 Interaction strength ϵ of LJ interactions (kJ/mol). In parenthesis is the corresponding MARTINI force-field bead type. 15
2.3 System Sizes 16

3.1 List of Simulations 36

4.1 Table of vaporization, hydration and partition free energy in kcal/mol. The partition free energy is evaluated for water/hexadecane interface. $\Delta G^{\mathbf{M}}$ is the free energy calculated using the MARTINI model [1], $\Delta G^{\mathbf{P}}$, with our water-explicit polarizable coarse-grained model, and $\Delta G^{\mathbf{E}}$ is the free energy from experiment [1]. 75
4.2 Interaction strength ϵ for LJ interactions (kcal/mol) 82
4.3 Bilayer thickness in different systems evaluated over last 100 ns data 94

5.1 Number of M^+ near POPC and POPS for Figure 5.2 134

List of Figures

2.1 CG scheme 11

2.2 Effect of Helix Capping: (a) Potential of mean force plot of a non-capped helical polymer at 300K, as a function of the mean absolute backbone dihedral and H1 parameter. Each contour level marks a kT unit. (b) Representative conformation of the helical protein in the folded ensemble, only backbone beads are shown (green for polar and cyan for hydrophobic residues). The arrows indicate dipole orientation. (c) Probability distribution of angles between oriented dipoles in the folded ensemble, of capped system (red) and non-capped helical polymer (blue). (d) Potential of mean force plot of a capped helical protein at 300K, as a function of mean absolute backbone dihedral and H1 parameter. (e) Representative conformation of the capped helical protein in the folded ensemble. Only backbone beads are shown (green for polar and cyan for hydrophobic residues), except for the negatively charged residue where the side-chain is shown in red. (f) Comparison of the time evolution of second dihedral angle (counting from the charged end) between capped system (red) and non-capped system (blue). . 19

2.3 (a) Probability distribution of alpha dihedral angles for β-strand regions of 6898 non-redundant proteins from the Protein Data Bank (red) in comparison with the folded CG ensemble of β-sheets from Figure S2 (blue). (b) Probability distribution of alpha dihedral angles for α-helical regions of 6898 non-redundant proteins from the Protein Data Bank (red) in comparison with the folded CG ensemble of α-helices from Figure 2 (blue). 20

2.4 (a) Potential of mean force of a β-sheet system as a function of the fraction of sheet contacts (Q) and end-to-end distance (Lc) at 300K. Each contour level marks a kT unit. (b) Representative CG β-sheet conformation of the folded ensemble, only backbone beads are shown (green for polar and cyan for hydrophobic residues). 20

2.5 (a) Potential of mean force plot of a helix bundle at 300K, as a function of the mean absolute backbone dihedral angle and the H1 parameter. Each contour level marks a kT unit. (b) Probability distribution of mean absolute dihedral angle in the folded ensemble of each of the two (red, blue) helix bundles. c) Folding curve of a helix bundle with dipoles (blue) and without dipoles (red).(d) Stages in helix bundle formation, starting from a coil-like conformation. Only backbone beads are shown (green for polar and cyan for hydrophobic residues). . . . 24
2.6 (a) Probability distribution of angles between macrodipole vectors of helices (taking the helix as a whole) in the helix bundles. (b) Representative structure of a helix bundle, white arrows are between i and $i+4$ dummy particles. The black arrows represent the macrodipole vectors of the helices in the bundle. 25
2.7 (a) Potential of mean force of a helix bundle sequence without backbone dipoles, as a function of average α dihedral angle and H1 parameter. Inset is a representative structure of the coil like conformation seen.(b) Potential of mean force plot of a sheet bundle sequence without backbone dipoles, as a function of sheet contacts (Q) and end-to-end distance (Lc). Inset is a representative structure of the coil like conformation seen. 26
2.8 (a) LJ energetic contribution of sheet bundles with (blue) and without dipoles (red), as a function of sheet contacts (Q). (b) LJ energetic contribution of helix bundles with (blue) and without dipoles (red), as a function of H1. (c) Coulombic energetic contribution of sheet bundles with dipoles, as a function of Q. (d) Coulombic energetic contribution of helix bundles with dipoles, as a function of H1. All represented ensembles obtained at 300K. 27
2.9 (a) Potential of mean force plot of a sheet bundle at 300K, as a function of the fraction of sheet contacts (Q) and end-to-end distance (Lc). Each contour level marks a kT unit. (b) Folding curve of a sheet bundle with dipoles (blue) and without dipoles (red). (c) Stages in sheet bundle formation, starting from a coil-like conformation. Only backbone beads are shown (green for polar and cyan for hydrophobic residues). 29

3.1 (a) Coarse-grained representation of $(GV)_4$ peptide, backbone beads (BB) are represented in translucent black, hydrophobic side chain beads in green, and positively and negatively charged dummies in blue and red respectively. (b) Polarizable BB bead; vdW radius of BB bead encloses dummy particles, BBm (negatively charged) and BBp (positively charged). 38
3.2 Initial conformation of (a) system V in water and (b) system VI at water-hexadecane interface. Water is represented in cyan, hexadecane in purple, and peptide backbone in black. 39

3.3 (a) Pairwise distance distribution of positively and negatively charged dummy particles in helical and sheet conformations. (b) Radial distribution function evaluated between hydrophobic side chain and water beads of system V. Red and blue curves represent "fibril-like" and "cross-β" like conformations. (c) Pairwise distance distribution between backbone beads of adjacent peptides in an aggregate. Blue curve represents system V with dipolar particles, and red curve, system V without dipolar particles. 41
3.4 Probability density plots using interpeptide pseudo H-bonds and radius of gyration of the aggregate over squareroot of N (number of monomers) as reaction coordinates for simulations exhibiting (a) "cross β" like and (b) "fibril-like" conformations in system V. Insets show representative conformations. Peptide backbone is shown in black, positive and negative dummies in blue and red, respectively. 43
3.5 Time evolution of average dipole moment per peptide backbone bead for (a) system I, (b) system II, (c) system III, and (d) system IV. . . 45
3.6 Average (a) dipole order and, (b) dipole moment per backbone bead with respect to $(GV)_4$ aggregate size. All error bars represent 95% confidence interval for the mean (assuming normal distribution) of collective data, as standard error of the mean is negligible due to large number of conformational information collected. Representative conformation of (c) 2 peptide aggregate; (d) 3 peptide aggregate; and (e) 4 peptide aggregate. Cyan and purple beads correspond to backbone representation of hydrophobic and neutral residues respectively. . . . 46
3.7 (a) Dipole energy per peptide as a function of aggregate size, linear fit shown in red (b) Average angle between dipole moment vectors and the local electric field, with different aggregate sizes. All error bars represent 95% confidence interval. 48
3.8 Observed aggregation mechanism for $(GV)_4$ peptide in water. Initial conformation of system V (12 peptides with backbone representation) at 0ns; disordered aggregate formed at around 5ns. Inset shows the presence of a hydrophobic core. Ordered aggregates formed at 25ns adopt "cross-β" like (top) or "fibril-like" (bottom) conformations. Cyan and purple beads correspond to backbone representation of hydrophobic and neutral residues respectively. Hydrophobic side chain beads shown in green. 49
3.9 Time evolution of the Lennard-Jones energy from hydrophobic side chain interactions (red), backbone Coulombic interaction (black) and total peptide-peptide energy (blue) for (a) 2 peptide , (b) 3 peptide, (c) 4 peptide, (d) 8 peptide, (e) 12 peptide system. (f) Hydrophobic side chain interactions of 2 (red), 3 (pink), 4 (green), 8 (purple) and 12 (black) peptide systems.Data obtained from one representative run, all energies are normalized by number of peptides in the aggregate. . 51

3.10 Time evolution of the number of water molecules per peptide (N_w) in the first hydration shell of hydrophobic side chain beads (green), and the number of pseudo-interpeptide hydrogen bonds (N_{hb}) formed (blue). (a), (b), (c) and (d) represent four distinct and representative trajectories for system V. Typical conformations shown as insets, side chain beads represented in yellow and backbone beads in black. . . . 53
3.11 Conformational frequency of 12 peptides system V (blue), VI (green), and control system without dipolar particles in a water environment (red). Representative conformations are shown as insets, backbone beads represented in cyan (hydrophobic residue) and purple (neutral residue). Hydrophobic side chain beads shown in green. 55
3.12 (a) Average peptide order parameter of aggregates in system V and VI (blue), the "fibril-like" conformation seen in water is represented by the red points. All error bars represent 95% confidence interval for the mean (assuming normal distribution) of collective data, as standard error of the mean is negligible due to large number of conformational information collected. Representative conformation of fibril-like structure, (b) showing dipole alignment, (c) lateral view displaying hydrophobic bead alignment on either sides. Representative conformation of cross-β structure seen in system V, (d) lateral view displaying hydrophobic core. Green arrows in (b) represent dipole vectors of each peptide, red and blue represent negative and positive dummy particles. Backbone beads in (c) and (d) represented in cyan (hydrophobic residue) and purple (neutral residue). Hydrophobic side chain beads shown in green. 56
3.13 Aggregation pathways observed in system VI, red arrows indicate that peptides aggregate at both interfaces; light blue represents water; black, the protein backbone; red and blue represent negative and positive dummy beads; and cyan represents hexadecane phase. (a), (b) ,(c) ,(d) and (e) represent five different mechanisms, see text for details. . 58
3.14 Time evolution of the fraction of different species in 12 peptides system (a) VI and (b) V. Green represents monomer fraction; blue, intermediate aggregate fraction, pink is a negative exponential fit and red, ordered aggregate conformation. (c) Representative pathway for ordered aggregate formation at hydrophobic-water interface, monomers [M] form ordered aggregates [O] with shortly lived intermediates. (d) Representative pathway for ordered aggregate formation in explicit water, monomers [M] form intermediate aggregates [I] which rearrange to form ordered conformation [O]. 60
3.15 Time evolution of the fraction of different species in (a) system VI and (b) system V. Green represents monomer fraction, blue, intermediate disordered fraction, and red, ordered aggregate conformation. 61
3.16 Fraction of monomer (green curve), disordered aggregate (blue curve) and ordered aggregate (red curve) for system V. Data averaged over 8 runs for each temperature. 62

3.17 Time evolution of the fraction of different species in (a) polyG octapeptides and (b) polyV octapeptides. Green represents monomer fraction, blue, intermediate disordered fraction, and red, ordered aggregate conformation.Dashed lines represent data at interfaces and solid lines, in water. 63
3.18 Representative conformations of 12 peptides system (a) VI and (b) V without dipolar particles. Cyan and purple beads correspond to backbone representation of hydrophobic and neutral residues respectively. Hydrophobic side chain shown in green. (c) Partitioning of hydrophobic side chain beads (green) to the hexadecane phase (cyan) for system VI with dipolar interactions. Peptide backbone shown in black. Time evolution of the fraction of different species, using the backbone distance cutoff in (d) system VI (dashed lines) and system V (solid lines) without dipolar particles, and (e) system VI (dashed lines) and V (solid lines) with dipole particles. Green represents monomer fraction, blue, intermediate aggregate fraction and, red, ordered aggregate. 64
3.19 PMF as a function of the peptide aggregate radius of gyration (Rg). PMF for peptides with dipoles (a) in explicit water and (b) at the interface; and peptide aggregates without dipoles (c) in explicit water and (d) at the interface. All represented ensembles obtained at 300K. 66

4.1 (a) Mapping scheme for POPC and POPS coarse-grained lipids; colors: green, hydrophobic bead; yellow, polarizable beads ; red, negatively charged bead; blue, positively charged bead. (b) Bead types: yellow represents polarizable beads (example : CNO, GL1, GL2), van der Waals radius of the bead encloses positively (+q/P) and negatively (-q/M) charged dummy particles (example:, CNP and CNM, G1P and G1M, G2P and G2M respectively) . The tunable parameters (l, q, θ, k_θ) are depicted. Blue bead represents a positively charged bead, red bead represents negatively charged bead, and green represents hydrophobic bead. 76
4.2 (a) Side view of POPS bilayer showing the lateral structure of the membrane. (b) Top view of POPS bilayer. Colors: serine (cyan), phosphate (tan), ester (pink), alkyl (green). 81
4.3 Bilayer peptide system setup. Peptide is placed 5 nm away from the bilayer. 83
4.4 Line tension ribbon structure. Phosphates are represented in brown, ester groups in pink, choline groups in blue, alkyl groups in green. . 86
4.5 Radial distribution functions for serine-involved (a-b) and ion-involved (c-d) electrostatic interaction pairs. (a) CNP-CNM (blue) and CNP-PO4 (green), (b) CNP-G1M (blue) and CNP-G2M (green), (c) ION-CNM (blue) and ION-PO4 (green), (d) ION-G1M (blue) and ION-G2M (green). 88

4.6 Time evolution of bilayer self assembly using pCG (polarizable coarse-grained) POPS. Phosphates are represented in brown, ester groups in pink, serine groups in blue, other groups in cyan. 91
4.7 Time evolution of bilayer self assembly using pCG POPC. Phosphate beads are represented in brown, ester groups in pink, choline groups are in blue, other groups in POPC in cyan. 92
4.8 Area per lipid change induced by the addition of 1M NaCl. The standard error of mean is within 10^{-3}nm^2. 93
4.9 Density distribution of (a) POPC from all-atom data, (b) POPS from all-atom data, (c) POPC from pCG data, (d) POPS from pCG data, (e) POPC from MARTINI data, (f) POPS from MARTINI data. Solid yellow: GL1; dashed yellow: GL2; red: PO4; blue: NC3/CNO; black: Na^+. 95
4.10 Density profiles of lipid bilayer systems with 1M NaCl. Solid brown: GL1; dashed brown: GL2; red: PO4; blue: NC3/CNO; black: Na^+; green: Cl^-. Density distribution of (a) POPC with 1M NaCl from pCG data, (b) POPS from with 1M NaCl from pCG data, (c) POPC with 1M NaCl from MARTINI data, (d) POPS with 1M NaCl from MARTINI data. 97
4.11 Residency time (τ), as a function of distance from the bilayer center for counter ions in pCG POPS system (black curve) and extra added ions (gray curve). 98
4.12 Residency time (τ), as a function of distance from the bilayer center for ions in all-atom POPS system. 98
4.13 Susceptibility profile of (a) POPC and (b) POPS bilayers. Potential profile of (c) POPC and (d) POPS bilayer. Atomistic profile is represented in red, MARTINI in gray and pCG in black. 99
4.14 Top view of head group clusters for a leaflet (each point represents a phosphate atom, and lines represents lipid connectivity) in (a) all-atom POPS bilayer, (b) pCG POPS bilayer, and (c) MARTINI POPS bilayer. Distinct colors are used to distinguish individual clusters. (d) Probability distribution of number of clusters in POPS bilayer in all-atom (cyan), pCG (blue), and MARTINI (green) systems. 101
4.15 Probability of 1, 2, 3 and 4 ion bridges bound to a POPS lipid at different ion concentrations. 103
4.16 (a) Representative structure of POPS lipid bound to Na^+ . Colors: Na^+ (green), CNO (black), PO4 (brown), GL1(pink), GL2(violet), alkyl (cyan) (b) Probability distribution of the angle made by the GL1-G1M vector of POPS with the bilayer normal in POPS (red). Dashed lines represent the systems with 1M NaCl and solid lines for 0M NaCl. (c) Representative structure of POPC lipid bound to Na^+. Colors: Na^+ (green), NC3 (brown), PO4 (brown), GL1(pink), GL2(violet), alkyl (cyan). (d) Probability distribution of the angle made by PO4-NC3 vector with bilayer normal in POPC. The dashed lines represent the systems with 1M NaCl and solid lines 0M NaCl 105

4.17 Lateral z distance of each side chain bead of SVS-1 strands (residue name on y-axis), from the center of mass of pCG POPS PO4 beads, with time. Color bar represents distance in Å, where negative values indicate deeper side chain penetration, below the com of PO4 layer. (a) and (b) represent different time periods. 107
4.18 Stages in SVS-1 sheet formation: peptide is randomly placed above the bilayer at t=0ns; lysine side chains interact with anionic POPS within a few ns. With lysine side chains buried in the bilayer, the backbone dummies interact to form sheets, which are formed as early as 30 ns in some runs. The peptide is dynamic on the surface of the bilayer and largely retains sheet content by the end of 300 ns. Colors: lipid hydrophobic core(green), peptide backbone(orange), positive and negative dummies in blue and red, phosphates in tan, esters in purple, CNO in cyan and lysines in yellow. 108
4.19 Time evolution of (a) sheet pair fraction (Fr_{sheet})of the peptide; (b) center of mass (com) distance of the peptide from the phosphate beads on the bilayer (Δz); (c) end to end distance (L_c) of the peptide, evaluated between the first and the last backbone bead. Each color represents a single run. Representative snapshots of conformations explored, each with a in-register sheet fraction of (d) 0.28, (e) 0.14, (f) 0.71, (g) 0.57 and (h) 1.0. All data from our polarizable coarse-grained models. 109
4.20 Time evolution of sheet pair fraction of the peptide (Fr_{sheet}) in blue and center of mass (com) distance of the peptide from the bilayer in red, for system with pCG POPS. a-f represents individual trials, and g, h and i are final conformations of trials depicted in c, d and e, respectively. 110
4.21 Time evolution of (a and d) sheet pair fraction of the peptide (Fr_{sheet}); (b and e) center of mass (com) distance of the peptide from the phosphate beads on the bilayer; (c and f) end to end distance (L_c) of the peptide, evaluated between the first and the last backbone bead. Each color represents a single run. (a), (b) and (c) are data from our polarizable coarse-grained model for POPC bilayer (d), (e) and (f) are data using our peptide model with dipoles and a POPS bilayer without dipole particles (POPSnd). 111
4.22 Time evolution of (a) sheet fraction (Fr_{sheet}) of the peptide in water, (b) end to end distance (L_c), (c) average dihedral angle per frame and (d) average 1-4 backbone distances (H1). Each color represents a single run. 112
4.23 LJ pairwise (dashed lines) and Coulombic energies (solid lines) as a function of Fr_{sheet} for (a) PO4-BB (green), CNO-BB(red) and BB-BB (blue), GL2-BB (cyan), GL1-BB (brown); (b) hydrophobic side chain self interaction (black) and hydrophobic side chain-alkyl (magenta); (c) PO4-SC_{C+} (green) and CNO-SC_{C+} (red), GL2-SC_{C+} (cyan), GL1-SC_{C+} (brown). Data from pCG POPS bilayer system. 113

4.24 Number density distribution of PO4 (red curves), lysine side chain (SC_{C+}) (black curves) and valine side chain beads (blue curves) over a time period of (a) 0-25 ns, (b) 25-50 ns, (c) 50-75 ns and (d) 75-100 ns. Side chain distributions are scaled by a factor of 5 for easy comparison. 115
4.25 Top view of a representative conformation of folded SVS-1 on POPS membrane. Peptide backbone is depicted in black, red and blue represent negatively and positively charged dummy beads. Brown vectors represent backbone dipoles and green vectors, CNO dipoles. Purple box denotes an example of dipolar connections or contacts within a peptide, that play a role in secondary structure content. Blue box denotes an example of peptide-membrane dipolar connections formed between backbone and CNO dummies. 116
4.26 Number density distribution of PO4 (red curves), lysine side chain (SC_{C+}) (black curves) and valine side chain beads (blue curves) for POPS system, over a time period of (a) 0-25 ns, (b) 25-50 ns, (c) 50-75 ns and (d) 75-100 ns. Side chain distributions are scaled by a factor of 5 for easy comparison. 117
4.27 LJ pairwise (dashed lines) and Coulombic energies (solid lines) as a function of L_c for (a and d) PO4-BB (green), CNO-BB(red) and BB-BB (blue), GL2-BB (cyan), GL1-BB (brown); (b and e) hydrophobic side chain self interaction (black) and hydrophobic side chain-alkyl (magenta); (c and f) PO4-SC_{C+} (green) and CNO-SC_{C+} (red), GL2-SC_{C+} (cyan), GL1-SC_{C+} (brown). Data for POPS bilayer without dipole particles represented on top (a, b, and c), and pCG POPC bilayer-SVS-1 system below (d, e and f). 118

5.1 Cluster time evolution of system with (a) $1.00\sigma M^+$, (b) $0.90\sigma M^+$, (c) $0.80\sigma M^+$ and (d) $0.70\sigma M^+$. 131
5.2 Representative snapshots of bilayer system with (a) $1.00\sigma M^+$, (b) $0.90\sigma M^+$, (c) $0.80\sigma M^+$ and (d) $0.70\sigma M^+$. Colors: POPC in blue, POPS in red, M^+ in yellow. 132
5.3 Distribution of lipid cluster size for system with (a) $1.00\sigma M^+$, (b) $0.90\sigma M^+$, (c) $0.80\sigma M^+$ and (d) $0.70\sigma M^+$. 132
5.4 Number of differently sized ions around POPC (green) or POPS (red) over the last 100ns of data collected. 133
5.5 Order parameters for POPC and POPS lipids for systems with (a) $1.00\sigma M^+$, (b) $0.90\sigma M^+$, (c) $0.80\sigma M^+$ and (d) $0.70\sigma M^+$. 135
5.6 Density distribution of phosphates (black curve), CNO (red curve), M^+ (green curve) and NC3 (blue curve) for (a) $1.00\sigma M^+$, (b) $0.90\sigma M^+$, (c) $0.80\sigma M^+$ and (d) $0.70\sigma M^+$. 136

5.7 Number of ions near (a)PO4 and (b)CNO. $0.70\sigma M^+$ in solid black, $0.80\sigma M^+$ for dashed black line, $0.90\sigma M^+$ in solid grey line and $1.00\sigma M^+$ in dashed grey line. (c) Representative snapshot of typical cluster of 3 POPS lipids with $0.80\sigma M^+$, shown in green is ion, serine in cyan, phosphate in tan and ester in pink. (d) Number of differently sized ions bound to PO4 (red) and CNO (green). 138
5.8 Total LJ (black bordered bars) and Coulombic energies (red bordered bars) for (a) $1.00\sigma M^+$, (b) $0.90\sigma M^+$, (c) $0.80\sigma M^+$ and (d) $0.70\sigma M^+$. 139
5.9 Hydration curves for POPC (grey curve) and POPS (black curve) lipids for (a) $0.70\sigma M^+$, (b) $0.80\sigma M^+$, (c) $0.90\sigma M^+$ and (d) $1.00\sigma M^+$. . . . 140

6.1 Time evolution of sheet fraction (a,d), end to end distance of peptide (b,e) and CoM distance between peptide and the bilayer for POPC and 1:1: POPC/POPS bilayer systems respectively. Different colors represent data for different peptides. 146
6.2 Number of POPS PO4 (blue), POPC PO4 (cyan), POPS alkyl tail (yellow), POPC alkyl tail (brown) residues around Lys and Val SC beads of SVS-1 bound to (a) 1:1 POPC/POPS bilayer and (b) POPC bilayer. Snapshot of POPC lipids with SVS-1 after 100ns of self-assembly simulation. 147
6.3 Time evolution of sheet fraction (a,d), end to end distance of peptide (b,e) and CoM distance between peptide and the bilayer for POPC and 1:1: POPC/POPS bilayer systems respectively. Different colors represent different peptides. 148
6.4 Representative SVS-1 conformations seen in water in systems with POPC bilayers. Colors: BB represented in black and LYS in orange. . 149
6.5 Stages in self assembly (SA) simulation with POPC, POPS and SVS-1 peptides.Front view of (a) initial conformation at time t=0ns, (b) conformation at t=20ns, (c) conformation at t=30ns and (d) top view of bilayer at t=40ns. The gap in the bilayer denotes inserted peptide. Colors: peptides in black, POPC in blue and POPS in red. 151
6.6 Representative snapshot of 1:1 POPC/POPS lipids with SVS-1 after 300ns of self-assembly simulation. Colors: PO4 in yellow, Lys SC in orange, Val SC in green, peptide backbone in BB, water in cyan, NC3 in purple, CNO in pink, POPS within 5 Å around peptide in red,and POPC within 5 Å around the peptide in blue. 152
6.7 (a) Saturated and (b) Unsaturated tail order parameters for POPC near inserted peptide (blue solid curve), POPS near inserted peptide (red solid curve), POPC away from inserted peptide (blue dashed curve) and POPS away from inserted peptide (red dashed curve). . . 153
6.8 Angle distribution between tails and bilayer normal for POPC near inserted peptide (black), POPS near inserted peptide (blue), POPC away from inserted peptide (red) and POPS away from inserted peptide (green). 154

6.9 (a) Number of POPS PO4 (green), POPC PO4 (cyan), POPS CNO (yellow) and POPC NC3 (purple) around Lys SC beads of inserted SVS-1 peptide in the last 100ns of the trajectory. (b) Number of POPS alkyl tail (blue), POPC alkyl tail (red) residues around Val SC beads of inserted SVS-1 peptide (see Figure 6.6), in the last 100ns of the trajectory. 155
6.10 Total number of water molecules present in the alkyl region between (a) 225-250ns, (b) 250-275ns and (c) 275-300ns of the the SA simulation. Color bar denotes number of water, X and Y axis, bilayer axis. . . . 155

List of Abbreviations

MD	Molecular Dynamics
CG	Coarse Graining
FF	Force Field
NPT	Isothermal-Isobaric Ensemble
NVT	Canonical Ensemble
PMF	Potential Mean Force
WEPPROM	Water Explicit Polarizable PROtein Model
WEPMEM	Water Explicit Polarizable MEmbrane Model
H-bond	Hydrogen Bond
BB	Backbone
H	Hydrophobic CG Residue
P	Polar CG Residue
N	Neutral CG Residue
Q+	Positively Charged CG Residue
Q-	Negatively Charged CG Residue
LJ	Lennard-Jones Interactions
ϵ	LJ strength
σ	Bead Size
μ	Dipole Moment
q	Charge
M^+	Monovalent Ion
Fr_{sheet}	Sheet Fraction
L_c	Peptide end to end distance

Chapter 1: Introduction and Outline of Thesis

Molecular simulations, both all-atom and coarse-grained (CG), have immensely contributed towards our understanding of molecular processes and complimented experimental observations. Processes such as membrane fusion, phase separation in lipidic mixtures, protein aggregation, membrane induced peptide folding and aggregation, can all be better explored with the help of coarse graining due to time and length scale constraints in these processes. The use of CG models have resulted in critical contributions by approximating key, essential interactions. One of the main advantages of CG force fields over all-atom ones, is the decrease in the system's degrees of freedom, which in turn (a) decreases computational costs, hence allowing for exploration of larger systems and time scales, and (b) smoothen the free energy landscape, thus facilitating better sampling of conformational space. However, one of the main challenges in biomolecular modeling remains building accurate and transferable models that can be used to investigate a wide range of molecular processes.

Understanding interactions between peptides and phospholipid bilayers is of key importance in a variety of biological phenomena, with relevance in bionanotechnological applications, materials and drug design [2, 3]. Since (a) all membrane proteins exhibit only two types of secondary structures : α helices (larger proportion) and β

sheets [4], and (b) secondary structure or hydrogen bond formation on the surface of the bilayer can decrease the thermodynamic barrier of peptide and protein insertion into cellular membranes; it is crucial to investigate the driving forces in membrane-peptide interfacial interactions. Coarse-grained models are especially useful in the investigation of protein-lipid interactions due to time scale and size constraints of relevant events like peptide membrane fusion, membrane induced peptide folding and aggregation etc. Over the course of the last few decades, multiple CG models for proteins and lipids have been developed, some of which are discussed below.

Simple models where residues are represented by a few beads have been very valuable in advancing our understanding of the protein folding process [5–8]. But the main drawback of them is that the parameters are normally tuned for a particular system and are not transferable. Therefore, they have to be re-calibrated according to the system of interest. On the other hand, there exist intermediate resolution models where the backbone is modeled with fine-resolution and the side-chain coarse-grained [9, 10]. A detailed backbone representation is essential to explore any secondary content changes in protein-lipid or protein-protein interaction. Upon inclusion of an hydrogen bonding interaction, these models are able to fold into helical structures without the addition of biases towards a native fold but fail toward stabilizing β-sheet structures [9,10]. The inclusion of explicit dipole-dipole interactions to these type of models has been shown to stabilize β-sheets [11–13]. However, all the above-mentioned models renormalize the role of the solvent through effective short-range, inter-residue interactions. Thus, they are not appropriate for studying the effect of the environment in protein folding since explicit solvent is needed. The importance

of the role of dipole interactions became evident from the work done by Scheraga *et al.* [14,15]. His group has shown that an optimization of the electrostatic interaction, by aligning the dipole of each backbone plane to a protein's electric field, is enough to fold small peptides using Monte-Carlo simulations without solvation [16–18].

Phospholipids are a fundamental component of cellular membranes, and many phospholipids are known to spontaneously form bilayers in water due to their amphiphilicity. The defining characteristic of these bilayers is the presence of two distinct regions; the hydrophobic tail and a hydrophilic region [19]. This hydrophilic region extends from the head group to the oxygen rich ester groups in phospholipids, and is known to have a dielectric constant between 34-4 [20]. Smit et al. developed one of the first CG model for lipids [21]. Today's CG lipid models are vast with varying degrees of resolution. The models that map 3-6 heavy atoms to one bead, thus maintaining chemical specificity, are more popular and widely used [22–24]. Ashcroft *et al.* [19] modeled phosphatidylcholine, one of the most prominent zwitterionic lipids in cellular membranes, as a five layered dielectric sandwich consisting of three electrically distinct membrane regimes: a higher dielectric head group, an intermediate dielectric ester group and a lower dielectric of hydrophobic alkyl tails. The polar groups in the lipid bilayer possess a substantial dipole potential of several hundred millivolts that arises from their organization at the membrane-water interphase, thus contributing to the total membrane potential profile [25]. This potential thus remains an important regulator of membrane structure and function, by modulating lipid-lipid, lipid-ligand interactions [26]. The recently developed water-explicit MARTINI CG force field [27] has been parameterized using water/oil and water/vacuum partitioning coefficients.

By doing so, the model parameters are transferable and do not depend on a particular system. This CG model is able to capture many lipid bilayer and transmembrane protein properties. However, it fails in capturing changes in secondary structure and cannot be used to study protein folding.

Even though there are many CG models that have been successfully used to study protein folding and aggregation [28, 29], the major drawbacks thus far have been (a) the inability to capture the effect of different dielectric environments explicitly and (b) their noncompatibility with membrane models. This makes these models inept for studying membrane induced peptide folding, ordered peptide aggregation or peptide folding in different environments.

The objective of this work is threefold:

- To gain a better understanding of the balance of physical forces (charged, weak-dipolar and hydrophobic interactions) in peptide folding and ordered peptide aggregation.

- To investigate the role of peptide-peptide, peptide-lipid and lipid-lipid interactions in driving membrane induced peptide folding and lipid-peptide co-aggregation.

- Development of polarizable CG models for peptides and lipids that are sensitive to changes in environment and can be used to investigate a multitude of physicochemical processes.

1.1 Outline of Thesis

In Chapter 2, we present a generic solvated coarse-grained protein-like model (Water Explicit Polarizable Protein Model (WEPPROM)) that can be used to characterize the driving forces behind protein folding. Each amino acid is coarse-grained with two beads, a backbone and a side-chain. While the backbone beads are modeled as polar entities, side-chains are either hydrophobic, polar or charged, thus allowing the exploration of how sequence patterning determines a protein fold. The change in orientation of the atoms of a polar coarse-grained unit is captured by the addition of two oppositely charged dummy particles inside a backbone coarse-grained bead. These two dummy charges represent a dipole which can fluctuate thus introducing structural polarization into the coarse-grained model. Realistic alpha/beta content is achieved *de novo* without any biases in the force-field toward a particular secondary structure. The dipoles created by the dummy particles interact with each other and drive the protein models to fold into unique structures depending on the amino acid patterning and presence of capping residues. We have also characterized the role of dipole-dipole and dipole-charge interactions in shaping the secondary and tertiary structure of proteins. Formation of helix bundles and beta-strands is also discussed.

In Chapter 3, WEPPROM is extended to study peptide aggregation at hydrophobic-hydrophilic interfaces and we draw comparisons to aggregation in explicit water solvent. Elastin-like octapeptides $(GV)_4$ are used as a model system for this study. A condensation-ordering mechanism of aggregation is observed in water. Our results suggest that backbone interpeptide dipolar interactions, not hydrophobicity, play a

more significant role in fibril-like peptide aggregation. We observe a cooperative effect in hydrogen bonding or dipolar interactions, with increase in aggregate size in water and interface. Based on this cooperative effect, we provide a potential explanation for the observed nucleus size in peptide aggregation pathways. The presence of a hydrophobic-hydrophilic interface both (a) increases order of aggregates formed, and (b) rate of aggregation process. Without dipolar particles, peptide aggregation is not observed at the hydrophilic-hydrophobic interface. Thus, the presence of dipoles, not hydrophobicity plays a key role in aggregation observed at hydrophobic interfaces.

In Chapter 4, we present a coarse-grained(CG) model for anionic and zwitterionic lipids that accounts for dipolar intricacies in the head group region (Water Explicit Polarizable MEmbrane Model (WEPMEM)). Two dummy particles with opposite charges are added to CG polar beads. These two dummy charges represent a fluctuating dipole that introduces structural polarization into the head group region. We have used POPC (1-palmitoyl-2-oleoyl-*sn*-glycero-3-phosphocholine) and POPS (1-palmitoyl-2-oleoyl-*sn*-glycero-3-phospho-L-serine) as our model lipids. We characterize structural, dynamic, and dielectric properties of our CG bilayer, along with the effect of monovalent ions. We observe head group dipoles to play a significant role in membrane dielectric gradient and lipid clustering induced by dipole-dipole interactions in POPS lipids. In addition, we have studied membrane-induced peptide folding of a cationic antimicrobial peptide with anticancer activity, SVS-1. We find that membrane-induced peptide folding is driven by both (a) cooperativity in peptide self interaction and (b) cooperativity in membrane-peptide interaction. In particular, dipolar interactions between peptide backbone and lipid head groups contribute to

stabilizing folded conformations.

In Chapter 5, we discuss the use of WEPMEM in understanding monovalent ion (M^+) mediated lipid domain formation using POPS and POPC lipid mixtures. Our study shows that at a certain size range of M^+, lipid domains of anionic PS and zwitterionic PC are formed. The domains of PS are more ordered, dehydrated and gel-like, whereas, the domains of PC are more disordered, hydrated and liquid-like. The formation of these domains are dependent on binding modes, certain binding modes lead to lipid phase separation, while others do not. The difference in binding between $Na^+, K^+ and\ Li^+$ to anionic lipids, could potentially explain the difference in monovalent ion induced binding, partition and domain formation.

In Chapter 6, the effect of SVS-1 peptide concentration in POPC: POPS (1:1) and pure POPC lipid mixtures is discussed using both fixed bilayer and self-assembly simulations. SVS-1 selectively partitions to POPS lipids when a mixed bilayer is present in the system. Peptide insertion is observed with mixed lipids, and the inserted peptide maintains its secondary structure content. The inserted peptide also pulls in lipids and water to the center of the bilayer, thus creating a polar patch in the bilayer assembly. Our results suggest that peptide folding and membrane leakage are coupled, as suggested by experiments with SVS-1 and SVS-2.

Chapter 2: Role of Dipole Interactions in the Formation of Secondary and Super-secondary Protien Structures

2.1 Overview

This chapter is based on the author's publication: Role of Backbone Dipole Interactions in the Formation of Secondary and Supersecondary Structures of Proteins; Sai J. Ganesan and S. Matysiak; Journal of Chemical Theory and Computation, 2014, 10 (6), 2569-2576

2.2 Introduction

Proteins are marginally stable and rely on cooperative effects to keep them in their folded structure [8,13,31]. A balance between charge interactions, hydrogen bonding and hydrophobicity is responsible for the formation of stable native folds. A simple description of an hydrogen bond can be based on an electrostatic dipole-dipole interaction. The formation of a protein backbone's hydrogen bonds leads to a particular orientation of dipoles in various types of secondary structural elements [32]. For example, it is well established that the CO and NH dipoles in an α-helix are

Reprinted with permission from [30] Copyright (2014) American Chemical Society.

electrostatically aligned and almost parallel to the axis of the helix [33]. Furthermore, studies have shown that the helical macrodipole can be exploited to stabilize or destroy a helical moiety by charge capping at the chain ends [34–36]. Placement of a positive amino acid at the C-terminus or negative at the N-terminus enhances helicity by a charge-macrodipole interaction.

Protein design studies have revealed that it is possible to design helix-bundle proteins and β-strands considering mainly the pattern of polar and non polar amino acids. Statistical analysis of folded structures has shown that non-polar amino acids appear in the protein sequence, every three to four amino acids in α-helical structures, and every two amino acids in solvent exposed β-sheets [7, 37].

In this chapter, we present a generic water-explicit CG model of proteins that can be used to characterize the driving forces behind protein folding without the addition of biasing potentials such as dihedrals potentials or dependencies in the bending potential with secondary structure propensities. The model has roots in the MARTINI CG force-field and thus it has the potential for extending it to model membrane protein folding. In the current implementation, each amino acid is coarse-grained with two beads, backbone and side-chain. The change in orientation of the atoms underlying the backbone coarse-grained unit, is captured by a flexible dipole that is created by oppositely charged dummy particles inside each backbone coarse-grained bead. These dipoles interact with each other through Coulombic potentials and introduce structural polarization into the model. Here we explore if just the addition of effective dipole interactions, in addition to Lennard-Jones interactions, is sufficient to produce secondary and supersecondary folds depending on sequence

patterning. We have evaluated the performance of the model by folding protein structures based on the sequence of amino acids. A molecular picture of how charge-capping stabilizes helical structures is also provided.

We use the sequence patterning of helices (-HHPPHH-) and sheets (-HPHPHP-) [37] to fold into distinct secondary structures. We then explore the role of helix capping by terminating helices with charged residues. Helix and sheet bundles are designed based on the above *de novo* patterns with the inclusion of turning regions.

2.3 Methods

2.3.1 Overview

An amino acid is modeled by two beads, a polar backbone bead (BB), that embeds a dipole, and a side chain bead (SC). The SC beads are broadly classified into hydrophobic (H), polar (P), positively and negatively charged (C+/C-) as depicted in Figure 2.1a.

The protein model explores the role of backbone dipoles in driving secondary and super-secondary structure formation. Therefore, the beads P and BB are treated differently. The distinction between H and P beads are purely pairwise interactions. The CG protein model is combined with the recently developed polarizable coarse grained water model [38]. The spherical backbone coarse grained bead consists of three interaction sites, the center bead BB, and two dipole particles, BBm and BBp, similar to the polarizable water model and depicted in Figure 2.1b. The main site, the center of the BB bead, interacts with other CG beads through a pairwise Lennard-Jones

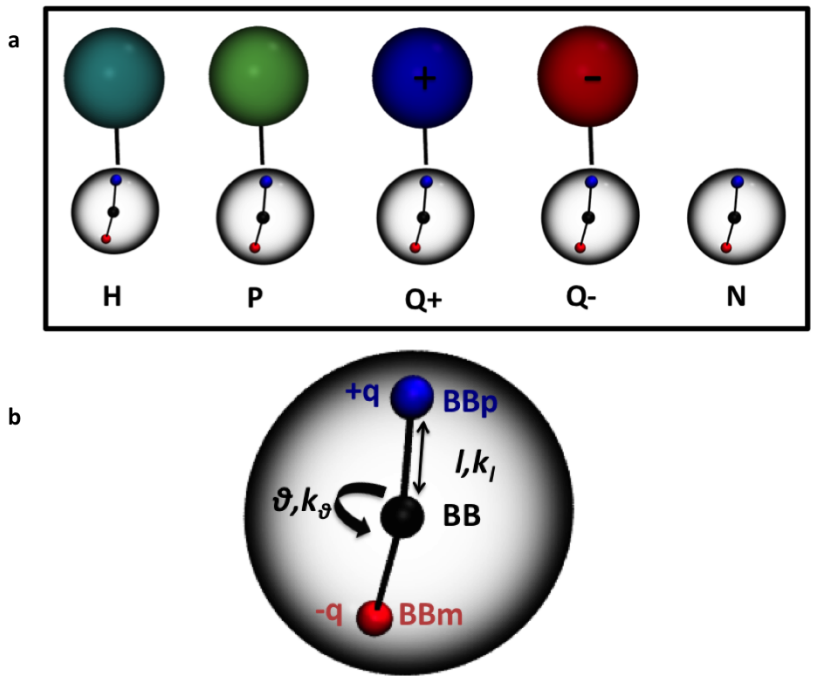

Figure 2.1: CG scheme: (a) Bead types (left to right); C- is the negatively charged residue, C+ is the positively charged residue, P and H are the polar and hydrophobic residues respectively. Gray represent the polarizable backbone (BB) bead and red, blue, green, cyan beads represent the side-chain (SC) beads. (b) Polarizable BB bead; VdW radius of BB bead encloses dummy particles, BBm (negatively charged) and BBp (positively charged). The 5 tunable parameters (l, q, θ , k_l, k_θ) are depicted.

potential. Dipole particles BBm and BBp are harmonically bound to the central particle BB (equilibrium distance (l), force constant (k_l)), and carry a positive and negative charge of equal magnitude (q) respectively. These dipole particles interact with other particles via electrostatic interactions. An harmonic angle potential (equilibrium angle (θ) and angular force constant (k_θ)) is used to control the rotation of BBm and BBp particles. Since the location of the dipole particles are not fixed, the

model is polarizable, i.e. the dipole orientation and moment of the backbone bead is dependent on the electric field of the surrounding environment. The rationale for using a polarizable backbone dipole as opposed to a fixed dipole is to make the dipoles environment sensitive, thus enabling in the future to study structural changes induced by backbone dipoles in different dielectric environments. To avoid overpolarization, a small repulsive core is added to the dipolar particles as commonly done in polarizable all-atom force fields. Since each main coarse grained site is covalently bonded to its nearest neighbors by a harmonic bond potential, and adjacent bonds are connected by a harmonic angle potential, all the 1-2 and 1-3 non-bonded interactions are excluded from the main coarse-grained sites and the corresponding embedded dipole particles. In addition, the nonbonded interactions between dipole particles inside the backbone CG bead are excluded as well. The mass of the whole bead (72 a.m.u) is distributed equally among the three particles (24 a.m.u each) in backbone beads.

2.3.2 Forcefield Parameters

The forcefield consists of bonded parameters (harmonic bonded and angular potential, dihedral potential is not included) and non-bonded parameters (12-6 Lennard-Jones (LJ) potential and Coulombic potential). The dipole moment distribution of the BB bead is parameterized to match that of a peptide bond (3.5 Debye) [39]. It is worth mentioning that with dipole moments of BB less than 3.5 Debye, helices are not formed. There are five parameters for the backbone CG bead that can be tuned to obtain the desired average dipole moment (l, q, θ , k_l, k_θ). For the backbone

CG bead, the following set of parameters yields an average dipole moment of 3.5 Debye: l=0.14nm, q=0.34, θ=0 degrees, k_l=5000kJ/mol and k_θ=7.2kJ/mol. Each BB bead is covalently bound to the adjacent BB bead by a bond distance of 3.85 $\mathring{A}$ and k_l=5000kJ/mol, distance parameterized from the average Cα-Cα bond distance observed from a 12mer polyalanine atomistic simulation with GROMOS force-field [40]. Other bonded interactions and LJ interaction strengths are borrowed from Marrink *et al.* [27]. The SC-BB harmonic bond distance is chosen as 0.4nm with k_l=5000kJ/mol based on a typical two bead residue in the MARTINI force-field. The BB-BB-BB harmonic angle is defined by θ=105° and k_θ=75 kJ/mol [41], and the SC-BB-BB harmonic angle by θ=100° and k_θ=75kJ/mol [27] .

Table 2.1: System Sizes

System	Box Size (X x Y x Z)	Water Molecules
Helix	7 x 6 x 4	1625
Capped Helix	7.5 x 6 x 4	1722
Helix Bundle	13.5 x 10 x 4	5036
Sheet Bundle	9 x 7.5 x 4	2572

The interaction strength ϵ of the LJ potential for the different non-bonded interactions is listed in Table 2.2. An effective size of $\sigma = 0.47nm$ is assumed for all

main CG interaction pairs in the LJ potential. With the interaction strengths taken from the MARTINI force-field, sheets are not formed. It has been observed that hydrophobic interactions play a dominant role in stabilizing β-sheets conformations [42]. The most hydrophobic bead type (a.k.a. C1 bead in the MARTINI force-field) is not hydrophobic enough to stabilize *de novo* sheet formation in the current model. A 12 mer chain of backbone beads only folds into a helical structure (results not shown). If hydrophobic side-chains have low hydrophobicity then the conformational ensemble is dominated by backbone properties that have an inherent preference over helical conformations. To correct for this, the ϵ between H beads and water (C1-POL) has been decreased from 2 kJ/mol to 0.2 kJ/mol, and between two H beads (C1-C1) increased from 3.5 kJ/mol to 3.75 kJ/mol; where sheet formation is observed. In addition, the charge SC (C+/C-) - backbone interaction strength is decreased from 5 kJ/mol to 4 kJ/mol to observe helix capping effects.

2.3.3 Simulation Setup

All system sizes are reported in the supplementary material (Table 2.3). Refer Appendix A for simulation parameters. Only for the construction of melting curves NVT simulations instead of NPT were performed from 300K to 600K. The starting conformation for all simulations was an extended random coil. For each system, the simulation data was collected over a 320ns NPT run, and the last 300ns was analyzed. A speedup of 6 times faster than atomistic simulations is observed when compared to a fully atomistic system. However, since coarse-graining smooth the

Table 2.2: Interaction strength ϵ of LJ interactions (kJ/mol). In parenthesis is the corresponding MARTINI force-field bead type.

Bead (bead type)	BB (P5)	H (C1)	P (P4)	C+ (Qd)	C- (Qa)	W (POL)
BB (P5)	5	2	5	4	4	4.5
H (C1)	2	3.75	2	2.3	2.3	0.2
P (P4)	5	2	5	4	4	5
C+ (Qd)	4	2.3	4	3.5	4	5
C- (Qa)	4	2.3	4	4	3.5	5
W (POL)	4.5	0.2	5	5	5	4

energy landscape more transitions from folded to unfolded states are observed when compared to atomistic simulations.

2.3.4 Electrostatic field

The alignment of the of the backbone dipoles with respect to the protein electric field is determined from the angle θ_i between the local electrostatic field, $\mathrm{E}_i(\mathrm{r}_i)$, and the ith dipole moment (μ_i) using the following equation:

$$\theta_i = arccos[\mu_i(r_i).E_i(r_i)/|\mu_i(r_i)||E_i(r_i)|] \tag{2.1}$$

Table 2.3: System Sizes

System	Box Size (X x Y x Z)	Water Molecules
Helix	7 x 6 x 4	1625
Capped Helix	7.5 x 6 x 4	1722
Helix Bundle	13.5 x 10 x 4	5036
Sheet Bundle	9 x 7.5 x 4	2572

where

$$\mu_i(r_i) = q_{BBm}(r_{BBm_i} - r_i) + q_{BBp}(r_{BBp_i} - r_i) \tag{2.2}$$

The quantities r_{BBm_i}, r_{BBp_i}, q_{BBm}, q_{BBp} represent position vectors and charge of the two dummy particles, and r_i is the position vector:

$$r_i = (|q_{BBm}|r_{BBm_i} + |q_{BBp}|r_{BBp_i})/(|q_{BBm}| + |q_{BBp}|). \tag{2.3}$$

The electric field due to the protein molecule is computed using Coulomb's law:

$$E_i(r_i) = \sum_j{}' q_j(r_i - r_j)/(|r_i - r_j|^3) \tag{2.4}$$

where the summation runs over all other charged sites in the structure, except the ones belonging to i, i $\pm$ 1 and i $\pm$ 2, as these interactions are excluded in the model and do not contribute to the local electric field of the considered dipole i.

2.4 Results and Discussion

Molecular dynamics simulation of different test systems, representing fundamental secondary and supersecondary motifs were performed. Different patterns of polar and non-polar amino acids, with and without the presence of capping charge residues were used to test the capability of our model to predict different types of motifs, and explore folding landscapes.

2.4.1 Role of Helix Capping

In agreement with previous findings [37,43–45], a 12mer sequence of -HHPP- folds into an α helix. Figure 2.2a depicts the potential mean force (PMF) of the helical system, using two reaction coordinates, the average absolute dihedral angle between backbone beads (50° corresponds to a perfect helix, a comparison of α dihedral angle of CG helix and sheet ensembles with PDB structures is shown in Figure 2.3) and the i to i+3 distance of backbone beads, H1 [46] (5.5 $\mathring{A}$ for a perfect helix). The two minima correspond to the folded helical state and the unfolded ensemble. Figure 2.2b depicts a typical folded conformation of the 300ns trajectory. Similarly, a 12mer sequence of -HPHP- folds into a β-sheet. Refer Figure 2.4 for PMF of the sheet system using two reaction coordinates, pair contacts (Q) and end-to-end distance (L_c).

To explore charge capping effects, we have introduced at one end of the 12-mer peptide a negatively charged amino acid (C-). The PMF plot for the capped system is shown in Figure 2.2d, and displays two distinct minima which correspond to a

fully folded helical state and a partially unfolded state that has some helical content. It is evident from a comparison of Figures 2.2b and 2.2d, that capping one end with a charge residue leads to an increase in helicity in the folded ensemble since the minima of the folded state is shifted towards H1=5.5 $\mathring{A}$. Also, upon helix capping the unfolded state becomes partially unfolded with a shift of H1 distances to lower values indicating more helical content.

Since the dipoles in the model act as pseudo hydrogen bonds, we also characterize the micro-dipole angles present in the folded helical structures . A dipole vector is defined from the negatively charge dipole bead of BB i (BBm) to the positively charge dipole bead of BB i+4 (BBp), as depicted by the arrows in Figures 2.2b and 2.2e. In Figure 2.2c, the effect of charge capping is evident from the probability distribution of dipole angles, which shows better alignment of the dipole angles of the capped system over the non-capped system. The hydrogen bonds in helices of crystal structures have the CO and NH dipole aligned, and almost parallel to the axis of the helix. Therefore, the enhancement of dipole alignment with capping signals an increase in helicity.

The time evolution of the second dihedral angle (counting from the charged end) depicted in Figure 2.2f clearly shows that the charged end contains a helical turn, which is stable throughout the whole trajectory, even in the partially unfolded state that helical turn is most of the time formed. On the other hand, the second dihedral angle of the non-capped system displays more coil-like conformations, as evident from the large fluctuations from 50 degrees. As shown in Figure 2.2e, the negatively charged SC bead of C- residue (red bead), groups the positively charged dipole par-

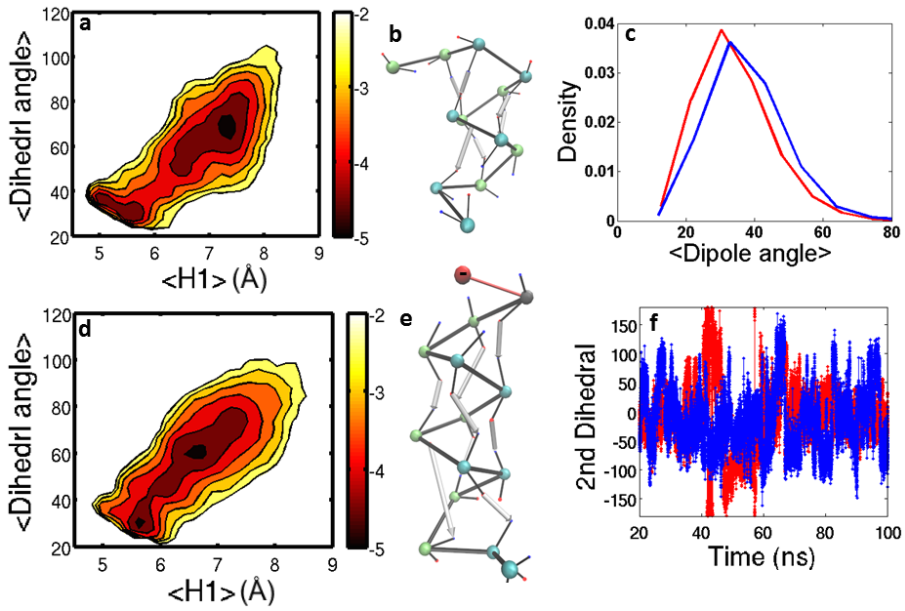

Figure 2.2: Effect of Helix Capping: (a) Potential of mean force plot of a non-capped helical polymer at 300K, as a function of the mean absolute backbone dihedral and H1 parameter. Each contour level marks a kT unit. (b) Representative conformation of the helical protein in the folded ensemble, only backbone beads are shown (green for polar and cyan for hydrophobic residues). The arrows indicate dipole orientation. (c) Probability distribution of angles between oriented dipoles in the folded ensemble, of capped system (red) and non-capped helical polymer (blue). (d) Potential of mean force plot of a capped helical protein at 300K, as a function of mean absolute backbone dihedral and H1 parameter. (e) Representative conformation of the capped helical protein in the folded ensemble. Only backbone beads are shown (green for polar and cyan for hydrophobic residues), except for the negatively charged residue where the side-chain is shown in red. (f) Comparison of the time evolution of second dihedral angle (counting from the charged end) between capped system (red) and non-capped system (blue).

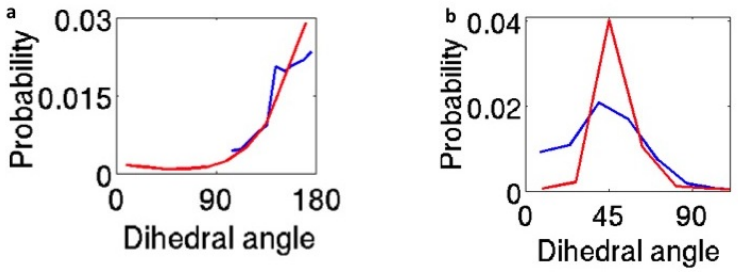

Figure 2.3: (a) Probability distribution of alpha dihedral angles for β-strand regions of 6898 non-redundant proteins from the Protein Data Bank (red) in comparison with the folded CG ensemble of β-sheets from Figure S2 (blue). (b) Probability distribution of alpha dihedral angles for α-helical regions of 6898 non-redundant proteins from the Protein Data Bank (red) in comparison with the folded CG ensemble of α-helices from Figure 2 (blue).

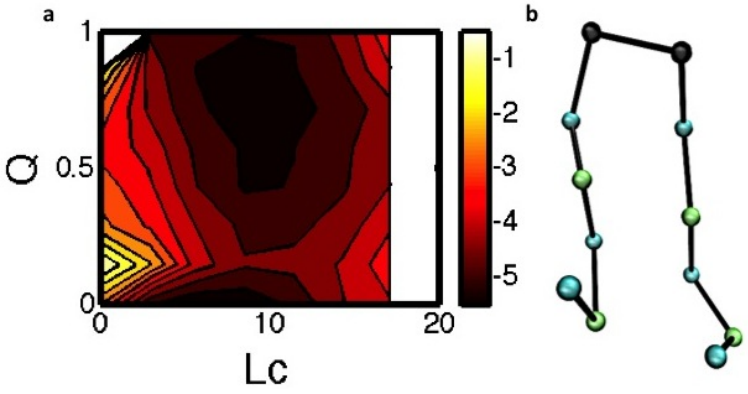

Figure 2.4: (a) Potential of mean force of a β-sheet system as a function of the fraction of sheet contacts (Q) and end-to-end distance (Lc) at 300K. Each contour level marks a kT unit. (b) Representative CG β-sheet conformation of the folded ensemble, only backbone beads are shown (green for polar and cyan for hydrophobic residues).

ticles of bonded neighboring backbone beads and creates a helical turn. It is worth mentioning that similar results are obtained when using a positively charged amino acid at one end. In that case, the dipole particles of bonded neighboring BB beads re-orient pointing the negatively charged dipole particles towards the positively charged SC bead, creating a helical turn (results not shown). Our model mimics the fact that N-terminus of a helix has amide groups that lack hydrogen bonds and the C-terminus has carbonyl groups that also lack hydrogen bonds, therefore the four residues of the ends are unable to satisfy the classical α helix hydrogen bonding interactions without proper capping, thus causing helix destabilization [47, 48]. Our results indicate that the enhancement of helicity by charge capping is due to a charge-dipole interaction. The dipole alignment caused by charge capping, promotes the formation of subsequent dipoles, thus promoting helix stabilization. This observation is in agreement with experimental data, showing that positively charged amino acids have a preference to C terminus and similarly, negatively charged side chains to the N terminus [49]. However, it is important to note that our model cannot distinguish N- and C- termini, as the BB beads are identical. As mentioned in the Method section, the LJ interaction strength between the charge side-chain and backbone beads (Qa/Qd-P5 pair interaction of the MARTINI force-field) had to be decreased, to allow for stabilization of helical structure as observed in Figure 2.2d. Without this change, the C- SC bead was interacting strongly with the backbone beads by LJ interactions thru the main CG sites, which did not allow for the dipole particles of the bonded nearest neighbor BB beads to re-orient towards the negatively charge that creates a helical turn (results not shown).

To further evaluate the effect of dipolar interactions in stabilizing secondary folds, we have computed the angle θ_i between the local electrostatic field, $E_i(r_i)$ and the ith dipole moment (μ_i) using equation 1. The folded ensembles of the 12-mer α-helix and 12-mer β-sheet are used in the calculation. An angle of 30.1° ± 8.7° is observed for the α-helix and 54.8° ± 12° for the β-sheet. These values agree very well with the reported values from Scheraga et al. work on a non-redundant set of PDB structures with atomistic resolution [16]. Those authors have found that the angle between the peptide bond dipole angle with the protein's local electrostatic field yields approximately 35° for α-helices and 50° for β-sheets. Furthermore, the average dipole energy ($<-(\mu.E)>$) of the CG helix is 4.5 times higher than the CG sheet. This value is slightly greater than the one reported from atomistic PDB structures by Scheraga et al. (average dipole energies between helix and sheets was found to be between 2.64 to 3.24) [16]. However, the same effect is observed, helices are more stabilized by the backbone dipoles than sheets. Also, helices are better aligned with the electric field than sheets.

2.4.2 Supersecondary Structures

2.4.2.1 Helix Bundles

Since the peptide with the repeating sequence of -HHPP- folds into a helix without any added bias, we have tested our model in predicting supersecondary structures such as helix bundles. Hydrophilic loops are very common in proteins and statistical analysis of protein structures has shown that the most common loop lengths in helix

bundles are between three to six amino acids [50–52]. Taking all this into account, we have designed turning regions (T) with five polar residues. We have tested the behavior of our model in *de novo* folding of a 33 residue with the sequence : $(HHPP)_{14}$-$(T)_5$-$(PPHH)_{14}$. As shown in Figure 2.5d, the chain folds into an α-helix bundle by a hierarchical manner where initially the peptide folds into two distinct helices on either ends. This is followed by the collapse of the chain into the helix bundle. Similar results were obtained when using a turning region of three, four or six residues (results not shown). The initial folding of the helices is induced by the orientation of the backbone dipoles, which is a local effect. Therefore helix and supersecondary structure formation is uncoupled. Clearly, the secondary structure is sufficiently stable in the absence of tertiary interactions, thus, folding proceeds in a hierarchical manner as observed for several proteins, such as the engrailed homeodomain [53, 54]. It is evident from the PMF (Figure 2.5a), using as reaction coordinates the average absolute dihedral angle between backbone beads and the distance H1, that there is a distinct folded and unfolded state. The unfolded state is very broad due to the fact that unfolded structures have different degree of helical content. This is in agreement with experimental observations, that for some helix bundle systems such as α3D, the thermal unfolded state is biased towards local helical content [55] .

It is known that right or left handed helices are present in helix bundles [56] with more proportion in nature of right handed helices. For the sequence pattern explored here, we observe that the helix bundles have either right or left handed helices (Figure 2.5b). This is because of the minimalist description of the backbone which does not have any chirality. By adding the micro-dipoles of each helix (arrows in Figure 2.6b)

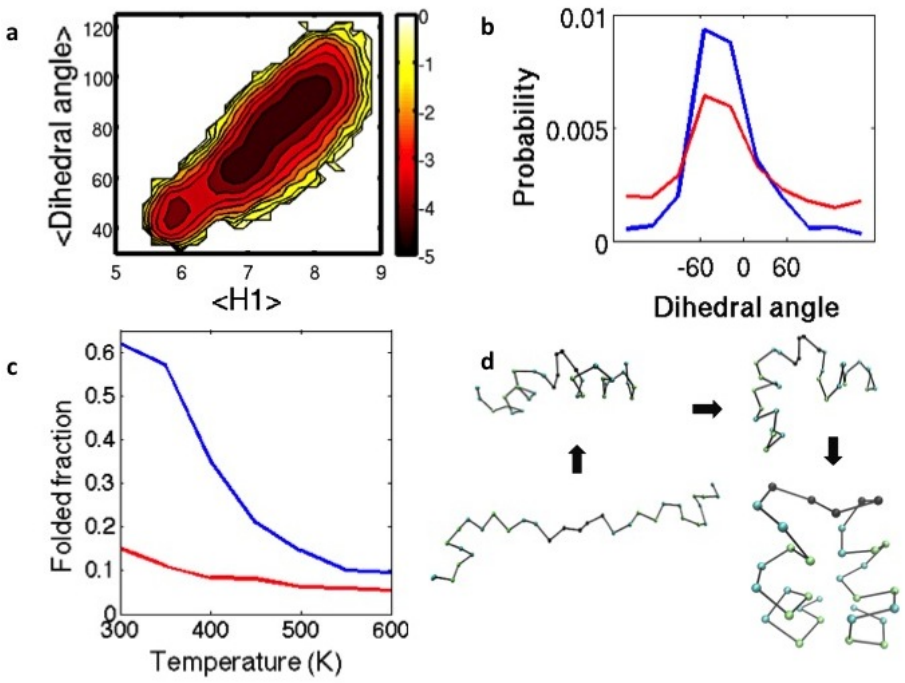

Figure 2.5: (a) Potential of mean force plot of a helix bundle at 300K, as a function of the mean absolute backbone dihedral angle and the H1 parameter. Each contour level marks a kT unit. (b) Probability distribution of mean absolute dihedral angle in the folded ensemble of each of the two (red, blue) helix bundles. c) Folding curve of a helix bundle with dipoles (blue) and without dipoles (red).(d) Stages in helix bundle formation, starting from a coil-like conformation. Only backbone beads are shown (green for polar and cyan for hydrophobic residues).

of the helix bundle we have computed the macro-dipole that exist in each helix. Figure 2.6 depicts the probability distribution of the angle between the two macro-dipoles (big black arrows in Figure 2.6b) for folded conformations. The macro-dipole angular distribution has a peak around 160°, which signals an almost anti-parallel dipole orientation that provides a favorable electrostatic interaction energy for helix

bundle formation. Known helix bundles of protein structures in the literature, exhibit the same anti-parallel orientation [57].

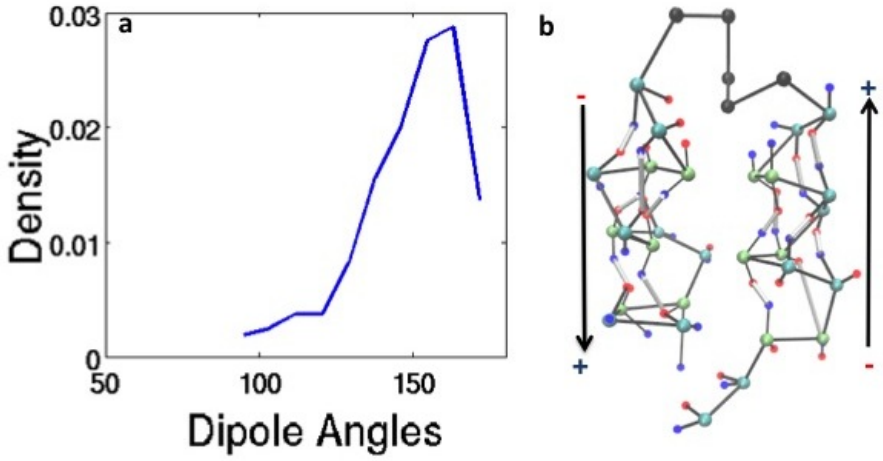

Figure 2.6: (a) Probability distribution of angles between macrodipole vectors of helices (taking the helix as a whole) in the helix bundles. (b) Representative structure of a helix bundle, white arrows are between i and $i+4$ dummy particles. The black arrows represent the macrodipole vectors of the helices in the bundle.

To further explore the effects of dipolar interactions in the folding of helix bundles, we have computed the folded fraction as a function of temperature in Figure 2.5c. A folded structure is considered if the average backbone dihedral of the whole protein structure is between 40° to 60° (Figure 2.5a). The blue curve in Figure 2.5c is for our model and the red one is without the inclusion of dipole particles. Clearly, without backbone dipoles, the folded fraction is almost constant at around 0.1 folded fraction at all temperatures. The effect of the addition of backbone dipoles is that the folding process becomes cooperative, achieving a folding fraction of 0.6 at 300K, as evident from the sigmoidal shape of the blue curve. Furthermore, Figure 2.7 shows

that without the inclusion of dipoles the system (T=300K) does not fold into a helix bundle, a representative of a collapse structure is shown as an inset of that Figure. Also, the system without the dipole particles do not exhibit any helicity.

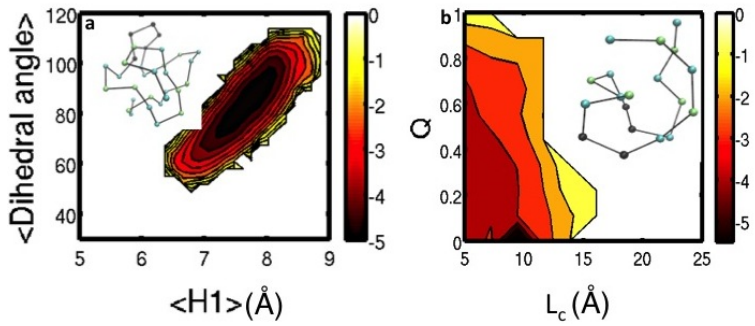

Figure 2.7: (a) Potential of mean force of a helix bundle sequence without backbone dipoles, as a function of average α dihedral angle and H1 parameter. Inset is a representative structure of the coil like conformation seen.(b) Potential of mean force plot of a sheet bundle sequence without backbone dipoles, as a function of sheet contacts (Q) and end-to-end distance (Lc). Inset is a representative structure of the coil like conformation seen.

Clearly, the folding of helical bundles is influenced by both the effect of dipolar interactions and pairwise LJ interactions, i.e it is a combination of the sequence patterning and electrostatic interactions. However, we observe that even though there are two major energetic contributions, the effect of dipoles is largely significant in the systems considered. To further elaborate, we characterized these two energetic quantities at 300K as a function of the reaction coordinate H1. It is clear from Figure 2.8b, that the effect of dipoles has a marginal effect on the LJ energetic contribution, which is lowest in the helical ensemble. It is also interesting to note that the helical

ensemble is more stabilized by the Coulombic contribution (refer Figure 2.8d), as can be seen by the larger energetic difference between folded (H1 around 6 nm) and unfolded conformations. Also, the presence of dipoles, increases cooperativity in folding the helical bundles, this is supported by both a) the large drop in Figure 2.8d, seen between folded and unfolded ensemble, and b) the sigmoidal behavior displayed by the melting curves of the helix bundles with dipoles (Figure 2.5c).

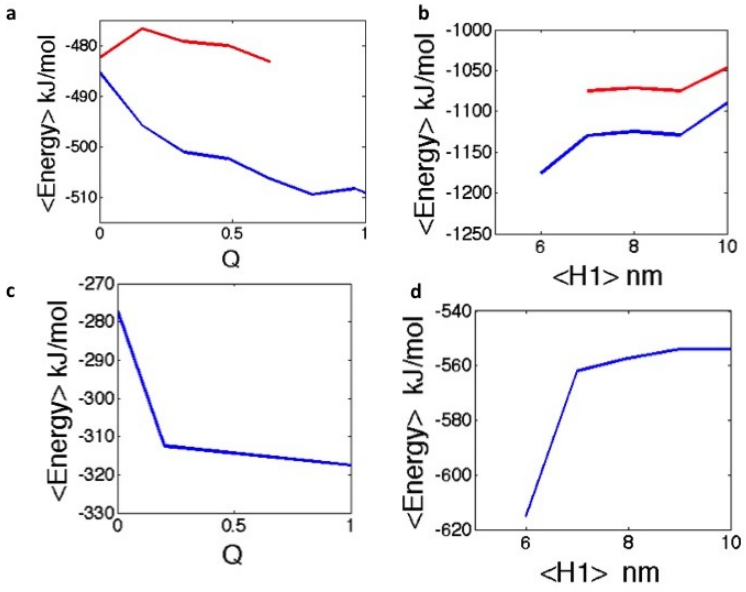

Figure 2.8: (a) LJ energetic contribution of sheet bundles with (blue) and without dipoles (red), as a function of sheet contacts (Q). (b) LJ energetic contribution of helix bundles with (blue) and without dipoles (red), as a function of H1. (c) Coulombic energetic contribution of sheet bundles with dipoles, as a function of Q. (d) Coulombic energetic contribution of helix bundles with dipoles, as a function of H1. All represented ensembles obtained at 300K.

2.4.2.2 Sheet Bundles

Finally, we tested the ability of the model in predicting β-strand bundles, solely based on sequence patterning. Statistical analysis of β-sheets structures have shown that hydrophilic short turning regions of two amino acids are very common [58–60]. Therefore, to model sheet bundles we decided to use 2 polar residues to create turns. The sequence pattern:HPHPHTTHPHPHTTHPHPH- folds without any biases into a three-strand antiparallel β-sheet, consisting of two hairpins, whose structure is reminiscent to the β3s protein [61, 62]. This sequence pattern is common in solvent exposed β-sheets [37]. The folding of the three-stranded β-sheet occurs through a hierarchical order of hairpin formation (Figure 2.9c). One hairpin is formed first with the second hairpin forming at the last stage of folding, in agreement with all-atom simulations of β3s [61]. It is worth noticing the matching of hydrophobic and polar residues in the folded structure. Figure 2.9a shows the PMF as a function of the fraction of sheet contacts (Q) and end to end distance (L_c). Q, is defined as the fraction of sheet pairs formed in a bundle. Two residues on neighboring strands within 4 $\mathring{A}$ to 7 $\mathring{A}$ are defined as a pair.

As shown in the PMF (Figure 2.9a), this protein exhibits a two-state folder behavior, characterized by the folded and unfolded state. It is noteworthy, that short sequences with a single turning region (HPHPHTTHPHPH) folds into a β-hairpin, also, four stranded β-sheets can be folded by adding a third turning region and an extra-HP- sequence (results not shown).

The melting curve of the sheet bundle exhibits a sigmoidal behavior characteristic

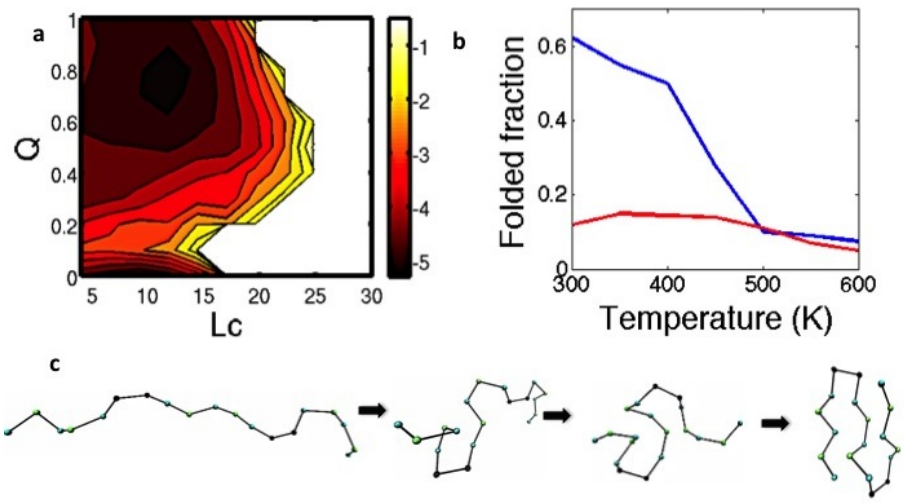

Figure 2.9: (a) Potential of mean force plot of a sheet bundle at 300K, as a function of the fraction of sheet contacts (Q) and end-to-end distance (Lc). Each contour level marks a kT unit. (b) Folding curve of a sheet bundle with dipoles (blue) and without dipoles (red). (c) Stages in sheet bundle formation, starting from a coil-like conformation. Only backbone beads are shown (green for polar and cyan for hydrophobic residues).

of cooperative processes, as shown by the blue curve of Figure 2.9b. A folded structure is defined by using structures with Q¿0.75. A control run without the inclusion of dipole particles was also performed using the sequence HPHPHTTHPHPHTTH-PHPH. As depicted by the red curve of Figure 2.9b, without backbone dipoles the folded fraction remains almost constant at around 0.1. It is also important to note, that the control run at T=300K does not fold into a β-sheet nor exhibit any secondary structure, as shown in Figure 2.7. To further characterize the driving forces behind the folding of sheet-bundles, we have characterized the energetic contributions (LJ

and Coulombic) as a function of Q at 300K. It is evident from Figure 2.8a, that the presence of backbone dipoles has an effect on the LJ contribution of the protein, which is minimum in the fully folded state. Figure 2.8c depicts the changes in Coulombic energy as a function of Q. By comparing Figure 2.8c and Figure 2.8d (helix bundles), it can be said that Coulombic energy plays a larger and a more cooperative role in helix bundles. Therefore, in the model the secondary and supersecondary structures are driven by the presence of the dipoles and the sequence patterning, however the effect of the added dipoles is more significant. The explored sequences do not fold into helix or sheet bundles in the absence of backbone dipoles.

2.5 Conclusions

In conclusion, the presented model introduces polarization into the protein backbone coarse-grained beads, which allows for the *de novo* folding of secondary structure and supersecondary structure assemblies based solely on the primary sequence. We have shown that our model is capable of folding helix bundles and β-sheet strands. Because of the minimalist description of the backbone, the helices fold either with right or left handedness. The chirality can be fixed by introducing *ad hoc* a quadratic term in the potential involving only quadruplets of successive backbone beads [63]. We have also shown that secondary structure formation is driven by backbone dipole interactions and sequence patterning. The charge-dipole interactions are found crucial in stabilizing helical folds. The presence of backbone dipoles increases the cooperativity of the folding process. Interestingly, helical conformations are more stabilized by

dipolar interactions than β-strands. Our model is currently composed of 4 bead types for the side-chain, however, it is possible to extend the model with more degrees of polarity and hydrophobicity (by varying LJ parameters) thus mimicking more amino acids.

Our model provides a step forward towards the development of transferable coarse-grained force field for proteins without biases towards secondary structure. In addition, since some of the model parameters were borrowed from the MARTINI coarse-grained force-field, our new model has the potential for extending it to model membrane protein folding. Also, since dipole interactions are influenced by the dielectric environment, we expect the proposed model to be sensitive to the nature of the environment (low or high dielectric).

Chapter 3: Interplay Between Dipole Interactions and Hydrophobicity In Peptide Aggregation At Interfaces

3.1 Overview

This chapter is based on the author's published work: Interplay Between Hydrophobic Effect and Dipole Interactions in Peptide Aggregation at Interfaces; Sai J. Ganesan and S. Matysiak; Physical Chemistry Chemical Physics, 2016, 18(4), 2449-2458

3.2 Introduction

Elongated protein fibrils are associated with multiple neurological diseases, such as Alzheimer's, Huntington's and prion diseases, among others [65–67]. Studies also suggest that the ability of proteins and peptides to form amyloid fibril structures is not limited to disease conditions, but a generic property of polypeptides [68–70]. The "core structure" of mature amyloid fibrils is known to involve an alignment of short peptide segments, between 6 and 12 residues, into cross-β structures [71]. Many kinetic mechanisms of aggregation have been proposed [72], however, nucleation-

Reproduced from Ref. [64] with permission from the PCCP Owner Societies.

growth process [73, 74] is the more accepted and dominant view. In the nucleation-growth process, a lag phase is observed, during which a nucleus (or a small oligomeric aggregate) is formed, followed by the rearrangement and elongation of the nucleus to fibrillar or ordered structures, known as the growth phase. Studies have revealed a number of potential intermediate species that can either lie on- or off-pathway to aggregation [75–77], thus suggesting the existence of a number of pathways to the final aggregated state.

The exact nature of the "nucleus" is not known, however, the presence of disordered aggregates seem to appear as intermediate states in many cases, and have been suggested to play the role of an "initiation site" for ordered amyloid fibril growth [74, 78, 79]. A condensation-ordering mechanism, where a disordered oligomer is formed initially, which eventually aligns to form a more ordered structure, has been observed in many experimental and theoretical studies of amyloid formation [67, 74, 80–82]. The common β-sheet structured core, seen in ordered fibrils formed by various polypeptides, suggests that intermolecular backbone hydrogen bonding is critical for the assembly of amyloid fibrils [83]. While hydrophobic interactions are crucial in stabilizing native proteins, the backbone hydrogen bonding network is known to be a dominant force in stabilizing amyloid fibrils [84, 85]. The cooperativity of this hydrogen-bond network, observed from first principle calculations, is believed to provide an extra-stabilization to peptide fibrils [86, 87].

The presence of surfaces such as cellular membranes is emerging as an important factor in amyloid formation, especially in the context of *in vivo* biological systems [88]. Solid surfaces have been observed to influence protein aggregation kinetics and mor-

phology in a variety of peptides [89, 90]. Confinement to two dimensions leads to an enhancement of protein concentration, whereas surface interactions promote the formation of aggregation-prone structures via an ordered templating mechanism. Aggregation studies on spherical nanoparticles revealed a condensation-ordering mechanism, similar to what was observed without a surface, independent of hydrophobicity [78, 91]. Experimental studies also suggest changes in conformation and hence aggregation morphologies, induced by the presence of surfaces [92]. In fact, octapeptides have been extensively studied using experiments [93–97].

Water-hydrophobic interfaces have been used as a model system to understand peptide aggregation on membranes. In particular, hexadecane slabs are known to be a good membrane mimetic environment [98]. Experimental and simulation studies have shown $(GV)_n$ peptides to be good models for studying amyloid formation, as these peptides have a propensity for forming β-sheet containing fibrils, both in water and at octane-water interfaces [99, 100]. Coarse-grained (CG) models have made a huge impact on our understanding of how peptides/proteins aggregate in scales difficult to achieve by atomistic simulations [101–103]. While atomistic simulations have given us insights into the first aggregation steps, they are unable to capture the entire aggregation process from monomeric species to fibrillar species [104, 105]. Most on- and off-lattice CG models that successfully capture different aspects of the oligomerization process renormalize the solvent environment through effective short-range, inter-residue interactions and do not take into account dipolar interactions [7, 106–109].

Our new water-explicit off-lattice CG protein model is described in chapter 2, we

now call it WEPPROM (Water-Explicit Polarizable Protein Model) [110]. The inclusion of backbone dipoles allows the protein model to achieve *de novo* helix and sheet content, based on the primary sequence, without any biases. Since hydrogen bonds are a type of dipole-dipole interactions, these added dipoles mimic Hydrogen-bond (H-bond) effect. However, it is important to stress on the fact that H-bonds have a covalent character due to the involvement of orbital interactions, which contributes to the directionality of the hydrogen bond [111, 112]. In water, the hydrogen bond is known to be roughly 90% electrostatic and 10% covalent in nature [113]. Since peptide backbone hydrogen bonds are also weak in nature, we think modeling H-bonds as dipole-dipole interactions is a reasonable approximation. In this chapter, we have used this new WEPPROM to probe the role of dipole interactions and water-hydrophobic interfaces in the aggregation of $(GV)_4$ octapeptides into fibril-like structures. Since in the WEPPROM model, the backbone dipole can fluctuate, we characterize if backbone dipoles exhibit any cooperative effect upon peptide aggregation, and how that translates to the stability and formation of fibril-like peptide aggregates. We investigate the balance between hydrophobic effect and dipole interactions in water and at interfaces. Our results suggest a difference in this balance for aggregation in water and at the interface. That is, hydrophobicity plays a more significant role for aggregating peptides in aqueous solution than at hydrophobic-hydrophilic interfaces. At hydrophobic-hydrophilic interfaces, without backbone dipolar particles, peptide aggregation is not observed.

3.3 Methods

Table 3.1: List of Simulations

System	Peptides	Concentration (M)	Runs	Interface
I	2	0.025	8	No
II	3	0.0375	8	No
III	4	0.05	8	No
IV	8	0.075	8	No
V	12	0.15	8	No
VI	12	0.15	8	Yes

3.3.1 System Setup

The block octapeptide $(GV)_4$ was modeled as a repeat neutral (N) and hydrophobic residue (H) sequence, respectively (see Figure 3.1a). The neutral residue was modeled as a spherical polar backbone bead (BB), which has an embedded dipole, as shown in Figure 3.1b. The hydrophobic residue has a hydrophobic side chain (SC) bead, in addition to the backbone bead. For details on the model, see chapter 2.

A hexadecane molecule was modeled as 4 hydrophobic beads, using 1:4 mapping scheme, with a backbone bond length of $0.47nm$ (bond constant $k_l = 1250kJ/mol$);

angle of θ=180° (angle constant $k_\theta = 25kJ/mol$), taken from the MARTINI forcefield [27]. The pairwise LJ interactions for these hydrophobic beads is the same as that for the hydrophobic side chain bead used in WEPPROM.

3.3.2 Simulation Setup

Peptide concentrations along with assigned system names used in this study are reported in Table 1. A cubic box of 5nm length with water density of $1040kgm^{-3}$ was used for simulations in explicit water. For simulations with hexadecane or an interface, a rectangular simulation box of equivalent volume of water and hexadecane (density $1090kgm^{-3}$) in a 5x5x10nm dimension was used. Both densities were obtained from equilibrium NPT simulations at 300K temperature and 1atm pressure respectively [38]. Snapshot images of initial system setup are shown in Figure 3.2. Eight replicate simulations of each concentration system were performed with the NVT ensemble at T=300K. To study the effect of temperature, eight replicate simulations of 12 peptide system in water was run at temperatures 350K, 365K, 375K, 385K and 400K.In each replica, distinct initial conformations of the peptides were assigned using a different set of random seeds. The highest concentrated system (12 peptide/system V), was studied in the presence of a water-hexadecane interface (system VI), keeping the concentration in water constant. To explore the role of sequence, we also looked at 12 poly-glycine (polyG) and poly-valine(polyV) octapeptides, both at the interface and in aqueous solution. These simulations were performed at 300K. To characterize the role of dipolar interactions, a set of control runs of system V and VI, without dipolar

particles were also carried out. A total of 100ns data was collected for each system. Refer Appendix A for simulation parameters.

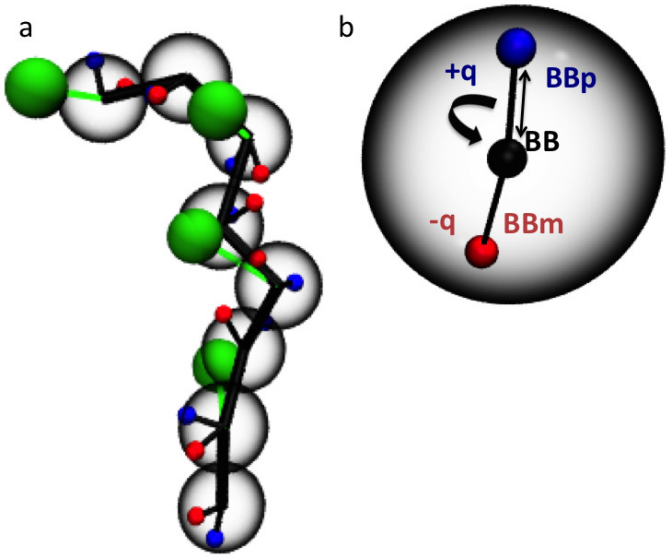

Figure 3.1: (a) Coarse-grained representation of $(GV)_4$ peptide, backbone beads (BB) are represented in translucent black, hydrophobic side chain beads in green, and positively and negatively charged dummies in blue and red respectively. (b) Polarizable BB bead; vdW radius of BB bead encloses dummy particles, BBm (negatively charged) and BBp (positively charged).

3.3.3 Analysis

The last 50ns of each trajectory was analyzed, unless otherwise stated.

3.3.3.1 Order Parameter.

Dipole order was evaluated using the principal method for determining orientational order in liquid crystalline systems, or the P2 order parameter [114]. This order

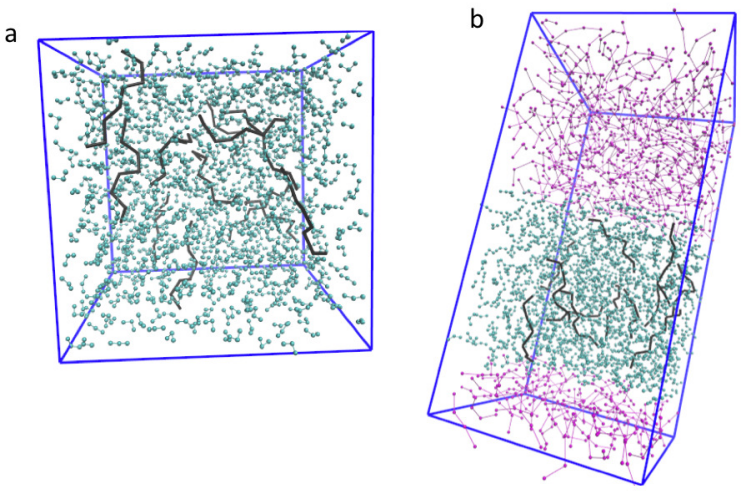

Figure 3.2: Initial conformation of (a) system V in water and (b) system VI at water-hexadecane interface. Water is represented in cyan, hexadecane in purple, and peptide backbone in black.

parameter is given by $\frac{3}{2}\lambda_{max}$, where λ_{max} is the highest eigenvalue of matrix S_d (Equation 1). N is the total number of backbone beads, u_i is a unit dipole vector within a backbone bead. P2 is 1 for a fully ordered system and 0 for a random system [115].

$$S_d = \frac{1}{N}\sum_i \begin{pmatrix} u_i^x u_i^x - \frac{1}{3} & u_i^x u_i^y & u_i^x u_i^z \\ u_i^y u_i^x & u_i^y u_i^y - \frac{1}{3} & u_i^y u_i^z \\ u_i^z u_i^x & u_i^z u_i^y & u_i^z u_i^z - \frac{1}{3} \end{pmatrix} \tag{3.1}$$

Peptide order was also calculated using the above P2 parameter, with N as the total number of peptides, and u_i as the end-to-end vector ($\vec{R}$) of a peptide. A similar definition of the orientational order parameter to characterize peptide aggregation has been used in a number of aggregation studies [109, 116, 117].

3.3.3.2 Dipole Moment and Energy.

Dipole moment (μ) for each backbone bead, in an aggregate, was evaluated using Equation 2. The quantities r_{BBm_i}, r_{BBp_i}, q_{BBm}, q_{BBp} represent position vectors and charge of the two dummy particles, and r_{com_i} is the center of mass vector of the backbone bead.

$$\mu_i(r_i) = q_{BBm}(r_{BBm_i} - r_{com_i}) + q_{BBp}(r_{BBp_i} - r_{com_i}) \tag{3.2}$$

3.3.3.3 Pseudo Hydrogen Bonds.

Since hydrogen bonds are a type of dipole-dipole interactions, and WEPPROM models a peptide backbone (CO-NH) as a dipole, we refer to dipolar interactions in our model as "pseudo" hydrogen bonds (H-bond). WEPPROM models H-bonds as purely dipole-dipole interactions and does not account for the covalent character of H-bonds. This is also the reason we refer to dipole-dipole interactions as "pseudo" H-bonds. The number of interpeptide pseudo hydrogen bonds was calculated as a measure of sheet content. A H-bond was defined between any two oppositely charged dummy particles on distinct peptides, within a cutoff of 2.5Å. This cutoff corresponds to the peak of a pairwise distance distribution between positively and negatively charged dummy particles in helical (i and $i+4$) and sheet conformations (see Figure 3.3a).

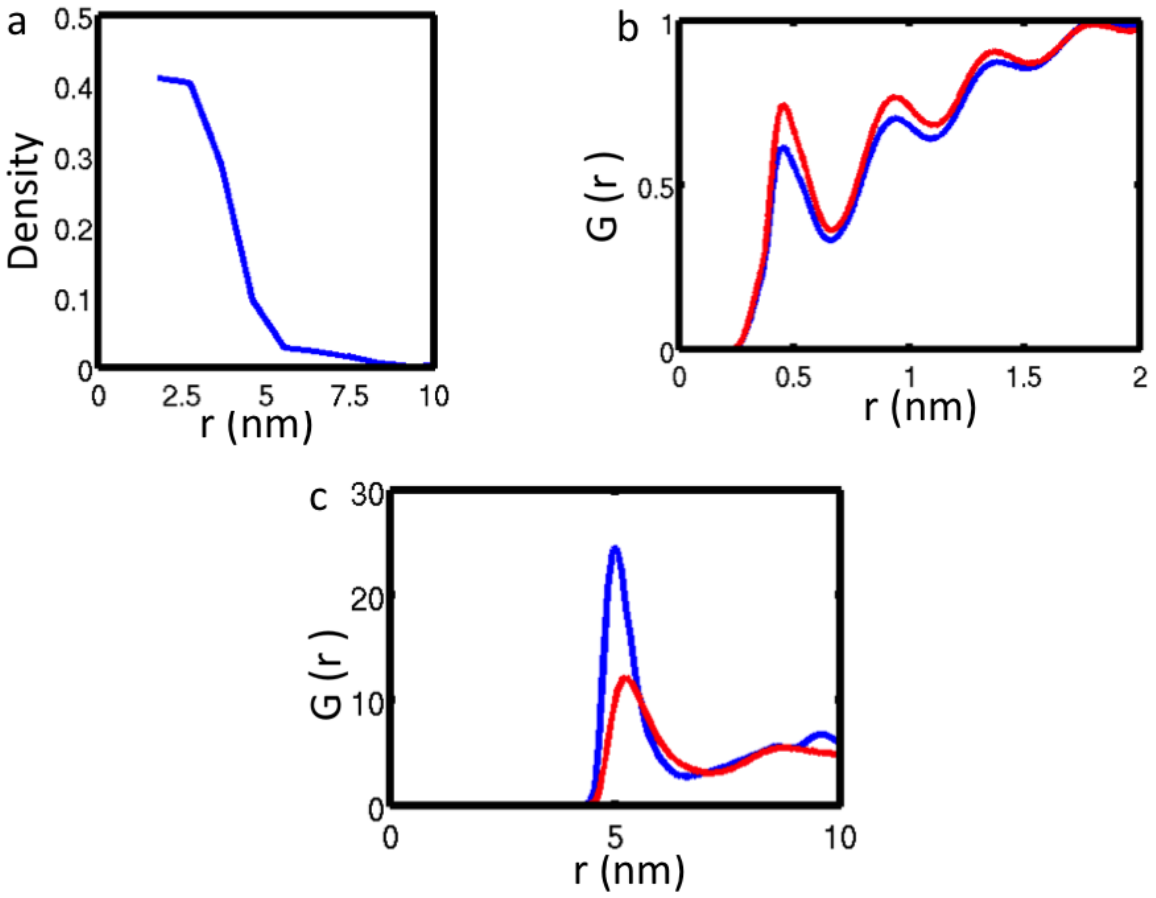

Figure 3.3: (a) Pairwise distance distribution of positively and negatively charged dummy particles in helical and sheet conformations. (b) Radial distribution function evaluated between hydrophobic side chain and water beads of system V. Red and blue curves represent "fibril-like" and "cross-β" like conformations. (c) Pairwise distance distribution between backbone beads of adjacent peptides in an aggregate. Blue curve represents system V with dipolar particles, and red curve, system V without dipolar particles.

3.3.3.4 Water Expulsion.

To explore the role of solvent, we evaluated the number of water molecules around hydrophobic side chain beads. We used a cut-off of 6.6 Å, which corresponds to the location of the first minima in the radial distribution function (RDF) plot between water and hydrophobic side chain beads (Figure 3.3b).

3.3.3.5 Conformational Analysis and Kinetics.

Aggregates formed can either be disordered or ordered β-sheets. Conformations were classified using the following criteria: if a peptide in an aggregate, made less than two pseudo interpeptide hydrogen bonds with any other peptide, it was classified as a monomer (M), else, defined as part of an aggregate. If each peptide of the aggregate made at least $\frac{n}{2}$ H-bonds, where n is the length of the peptide, we termed the aggregate as an ordered aggregate, else, intermediate or disordered. This criteria is consistent with a similar kinetics study from Hall's group on peptide aggregation [118]. We used the same criteria for our temperature studies as well. To compare kinetics or dynamics of aggregates between systems, with and without dipolar particles, a backbone bead cutoff (5Å) was used in place of interpeptide H-bonds. This cutoff was obtained by comparing pairwise distance distributions between backbone beads of different peptides in an aggregate, with and without dipolar particles, for 12 peptides system V (blue and red curves in Figure 3.3c).

The ordered aggregates can either adopt a "cross-β" or "fibril-like" conformation in water. Radius of gyration (R_g) was used to distinguish these two ordered pop-

ulations. As shown in Figure 3.4a and 3.4b, a "cross-β" like aggregate populates the $\frac{R_g}{\sqrt{N}}$ (where N is the number of peptides) region of 1.5 to 2.5nm and has at least 6 interpeptide H-bonds. Whereas a "fibril-like" aggregate occupies the region of 3.5 to 4.5nm and has greater than 8 interpeptide H-bonds. The above parameters were used to determine the conformational frequency of $(GV)_4$ aggregates in water. At the interface, only "fibril-like" aggregates were seen, and hence the H-bond cutoff was sufficient to distinguish ordered from disordered conformations.

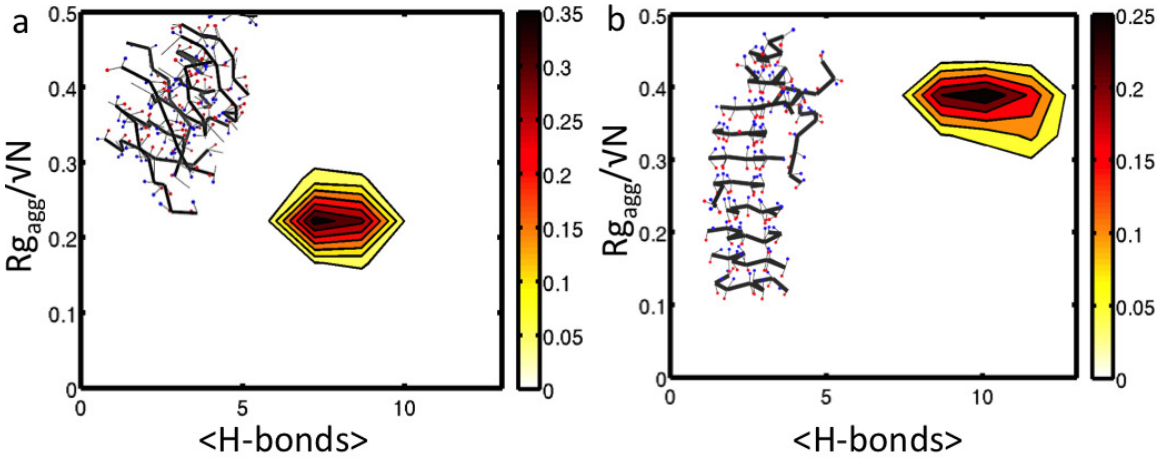

Figure 3.4: Probability density plots using interpeptide pseudo H-bonds and radius of gyration of the aggregate over squareroot of N (number of monomers) as reaction coordinates for simulations exhibiting (a) "cross β" like and (b) "fibril-like" conformations in system V. Insets show representative conformations. Peptide backbone is shown in black, positive and negative dummies in blue and red, respectively.

3.3.3.6 Potential Mean Force.

Potential mean force (PMF) for aggregates in water and at the interphase, for systems with and without dipoles were evaluated using Equation 3. The quantities $p(R_g)$ is the probability distribution of radius of gyration of the aggregate formed, W is the PMF, k_b is the Boltzmann constant and T is 300K in our study.

$$W(R_g) = -k_b T ln p(R_g) \tag{3.3}$$

3.4 Results and Discussion

3.4.1 Effect of Concentration

We first present the results characterizing the effect of concentration in determining the structure and stability of aggregated conformations. All the simulations performed in explicit water resulted in transient or stable aggregate structures.

To characterize the conformations, we looked at the time evolution of the average backbone dipole moment (Figure 3.5). Backbone dipole moments of 2 and 3 peptides systems (I and II) fluctuate between 3 and 5D (Figures 3.5a-b), whereas, for systems III and IV (4 and 8 peptides systems), the value remains constant at around 4.5D after 10ns (Figures 3.5c-d). System I (2 peptides) fluctuates more than system II (3 peptides), and system II stabilizes higher dipole moment conformations. Therefore, more ordered and stable conformations are observed in system II, at 300K. Whereas,

aggregates of 4, and 8 peptides result in stable, structured and ordered conformations. Figures 3.6c-e are representative conformations of 2, 3 and 4 peptide aggregates, respectively.

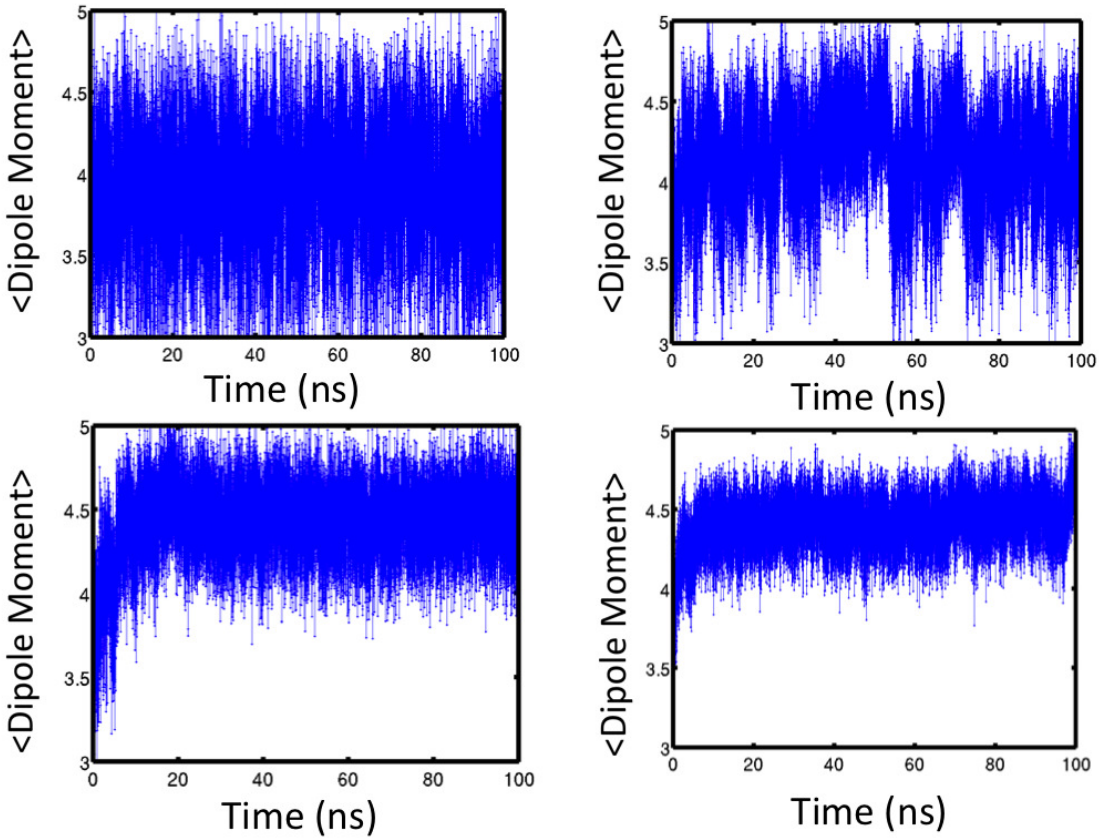

Figure 3.5: Time evolution of average dipole moment per peptide backbone bead for (a) system I, (b) system II, (c) system III, and (d) system IV.

These results lead us to the following question: why is the 4 peptide aggregate, the smallest, stable, ordered aggregate? To answer this question, a few backbone(BB) dipole parameters were evaluated. The BB dipole order, and BB dipole moment per residue of various aggregate conformations are depicted in Figure 3.6a and 3.6b, respectively. The dipole moment and order exhibit a sharp increase from an aggregate

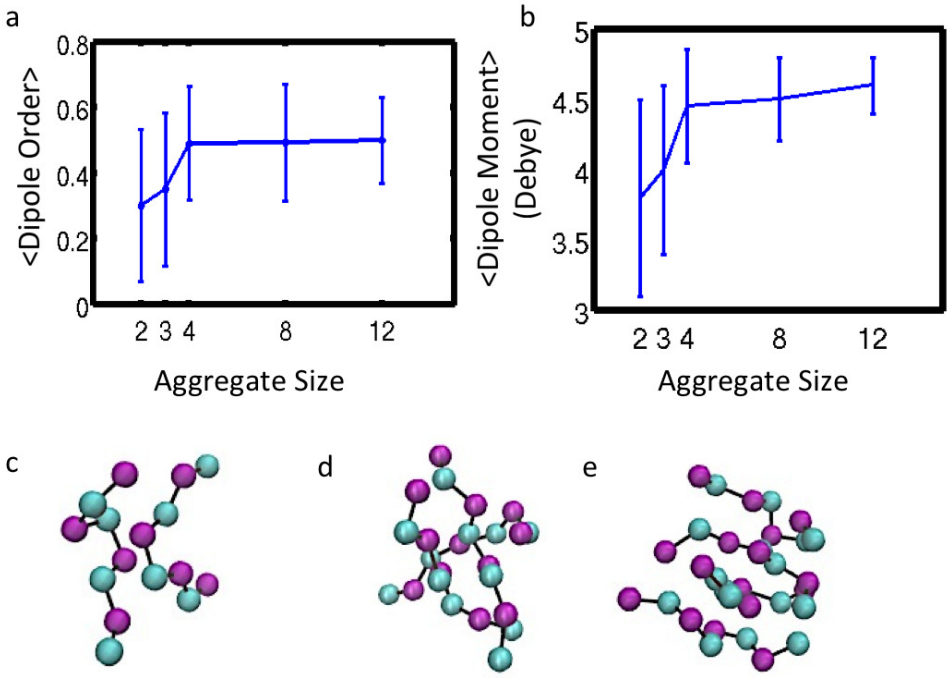

Figure 3.6: Average (a) dipole order and, (b) dipole moment per backbone bead with respect to $(GV)_4$ aggregate size. All error bars represent 95% confidence interval for the mean (assuming normal distribution) of collective data, as standard error of the mean is negligible due to large number of conformational information collected. Representative conformation of (c) 2 peptide aggregate; (d) 3 peptide aggregate; and (e) 4 peptide aggregate. Cyan and purple beads correspond to backbone representation of hydrophobic and neutral residues respectively.

size of 2 to one of size 4. Adding more layers of peptides to an aggregate of size 4 does not significantly increase the dipole order or moment per residue. Specifically, the dipole moment can be considered as a representative strength of the pseudo hydrogen bond network. From Figure 3.6b, we see an increase in this strength up to four layers of peptides, before leveling off at 4.5 D. That is, there exists "cooperativity"

in both dipole order and moment with increase in aggregate size, that saturates at aggregate size 4. This cooperativity of pseudo hydrogen bonds or dipolar interactions contributes to the stability of the four peptide aggregate. Therefore, an aggregate of size 4 is the minimum aggregate size with the highest dipole moment per residue. This size coincides with previous studies that have identified a nucleus size for aggregation between 3 and 4 peptides [119]. Cooperative effect of hydrogen bond networks in amyloid fibrils has been previously studied using *ab initio* calculations. A DFT study on peptide GNNQQNY from yeast prion Sup35, also identified a nonlinear increase in energy per monomer, up to 4 layers of peptide, before saturation [87]. A similar effect caused by side chain hydrogen bonding of polyQ aggregates has also been observed [86].

Dipole energy, which is a measure of how aligned a dipole vector is to the local electric field (E), given by expression $< -\vec{\mu}.\vec{E} >$ was also evaluated [110,120]. Figure 3.7a depicts the dipole energy per peptide with respect to aggregate size, and shows a linear increase in dipole energy with aggregate size (a linear fit is shown in red). The observed linear increase is due to the local electric field strength, which increases with aggregate size. The angle between the backbone dipole vectors and the local electric field is shown in Figure 3.7b. This angle is a measure of the alignment between backbone dipole vectors and the electric field. A decrease of this angle with aggregate size is due to a better alignment with the local electric field. It is interesting to note that this decrease in alignment also saturates at an aggregate size of 4, thus revealing a cooperative behavior consistent with dipole moment and dipole order (Figures 3.6a and 3.6b).

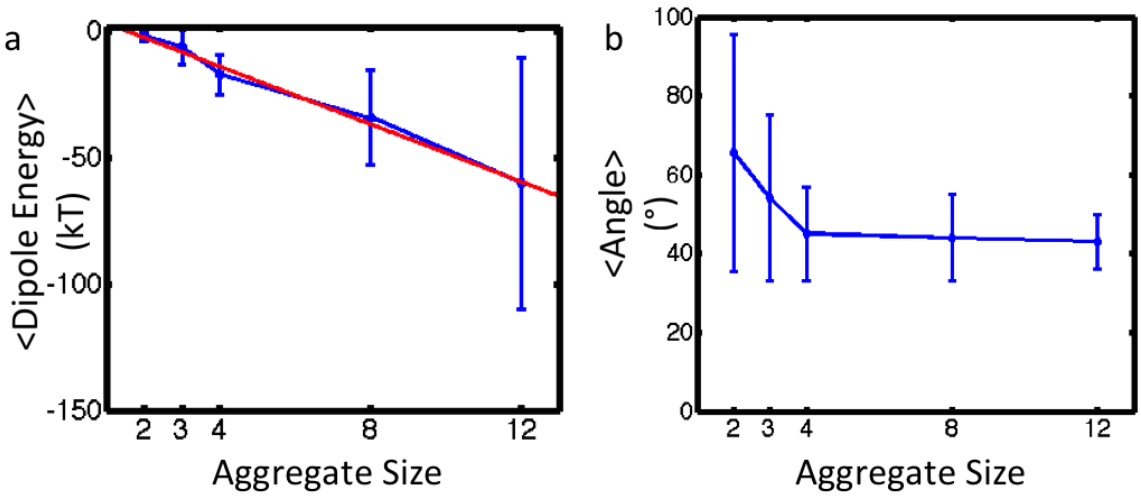

Figure 3.7: (a) Dipole energy per peptide as a function of aggregate size, linear fit shown in red (b) Average angle between dipole moment vectors and the local electric field, with different aggregate sizes. All error bars represent 95% confidence interval.

3.4.2 Energetic Contributions and Role of Water

As shown in Figure 3.8, within 5ns, randomly distributed peptides collapse into disordered aggregates with the formation of a hydrophobic core for system V (12 peptides). This disordered aggregate then rearranges to form either "fibril-like" or "cross-β" like sheet structures. These results indicate a two-step condensation-ordering mechanism, that has previously been identified in simulations of $A\beta_{16-25}$, $A\beta_{25-35}$, prion protein Sup35 and capped polyalanine sequences [74, 107, 121]. In this mechanism, a disordered oligomeric aggregate structurally reorganizes into ordered amyloid fibrils [91].

We take a closer look at peptide-peptide energetic contributions to identify the driving forces behind the aggregation process. The time evolution of LJ hydrophobic

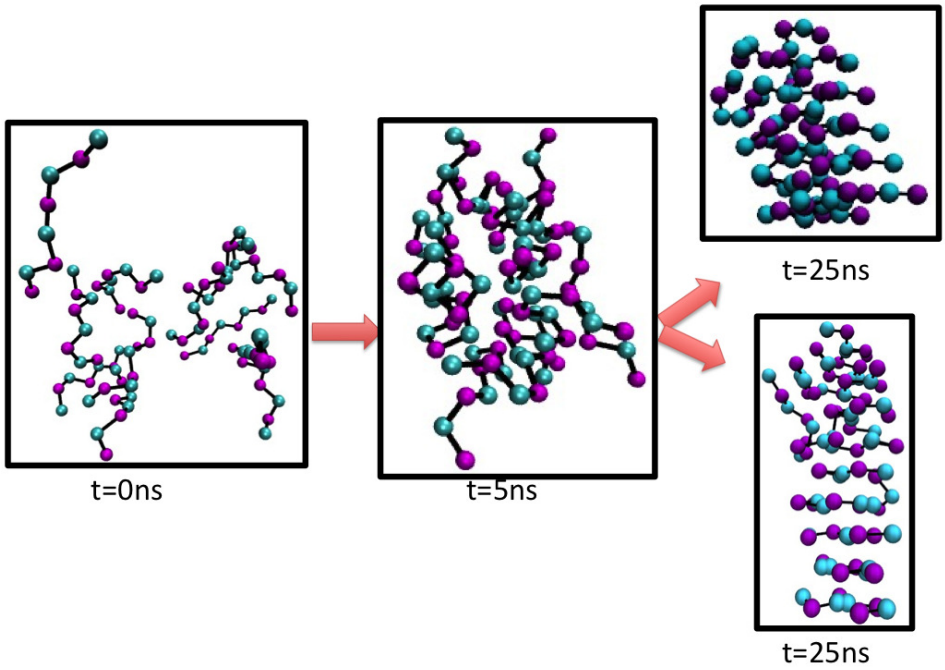

Figure 3.8: Observed aggregation mechanism for $(GV)_4$ peptide in water. Initial conformation of system V (12 peptides with backbone representation) at 0ns; disordered aggregate formed at around 5ns. Inset shows the presence of a hydrophobic core. Ordered aggregates formed at 25ns adopt "cross-β" like (top) or "fibril-like" (bottom) conformations. Cyan and purple beads correspond to backbone representation of hydrophobic and neutral residues respectively. Hydrophobic side chain beads shown in green.

side chain interactions (red curve), backbone Coulombic interactions (black curve), and total interpeptide energy (blue curve) for representative trajectories are shown in Figures 3.9a-e, for different peptide systems. These energies are normalized by the number of peptides in the aggregate. These plots clearly indicate that the initial conformation of randomly distributed peptides has the highest energy (Figures 3.9c-

e), except in the 2 and 3 peptide systems (Figures 3.9a-b), where the aggregates formed are neither stable nor ordered. The transient nature of 2 and 3 peptide aggregates is visible from the transitions seen in energy values (Figures 3.9a-b). However, for the remaining systems, the final aggregate is the conformation of lowest energy. It is interesting to note that the trend followed by the total peptide-peptide energy (blue curve) is similar to the Coulombic energy (black curve) in systems II (3 peptides), III (4 peptides), IV (8 peptides) and V (12 peptide), see Figures 3.9b-e. The Coulombic energy displays the largest energy drop in these systems. This drop in energy arises from backbone dipolar interactions, or interpeptide hydrogen bonds. For systems III, IV and V (4, 8 and 12 peptides, see Figures 3.9c-e), the Coulombic and total peptide energy decrease until 20ns, and remains constant thereafter, till the final aggregate conformation is reached. A comparison of representative hydrophobic side chain interactions for the above described systems are shown in Figure 3.9f. For aggregates of size 8 and 12 (blue and black curves respectively), the hydrophobic contribution is comparable and more drastic than for smaller aggregates of size 2 (red), 3 (pink), and 4 (green). This is because the largest drop in hydrophobic LJ energies is due to the formation of a hydrophobic core, which is not formed in the case of smaller aggregates. A control run of 12 peptide system V without dipoles, exhibits hydrophobic collapse and results in disordered structures (discussed later). Therefore, interpeptide hydrogen bonding plays a major role in driving ordered structures. This is in agreement with many studies that have suggested a larger role for backbone hydrogen bonding than hydrophobic interactions in amyloid fibril aggregation [78, 85, 91, 122]. Gordon *et.al.* showed that replacing two amide bonds of $A\beta_{16-20}$ with

ester groups lacking amide protons prevented aggregation, thus shedding light on the relevance of backbone interpeptide hydrogen bonding, even for a largely hydrophobic peptide.

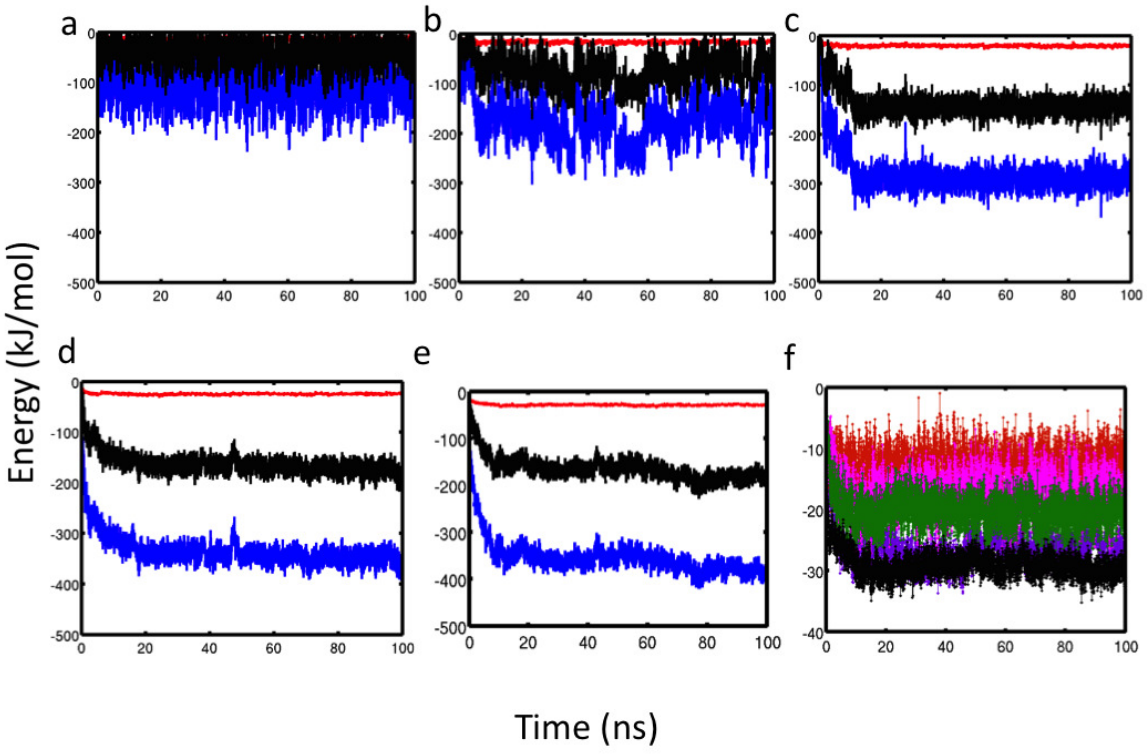

Figure 3.9: Time evolution of the Lennard-Jones energy from hydrophobic side chain interactions (red), backbone Coulombic interaction (black) and total peptide-peptide energy (blue) for (a) 2 peptide , (b) 3 peptide, (c) 4 peptide, (d) 8 peptide, (e) 12 peptide system. (f) Hydrophobic side chain interactions of 2 (red), 3 (pink), 4 (green), 8 (purple) and 12 (black) peptide systems.Data obtained from one representative run, all energies are normalized by number of peptides in the aggregate.

3.4.3 Mechanisms of Water Expulsion

To better understand the significance of hydrophobic interactions in $(GV)_4$ octapeptide, we characterized the water expulsion from hydrophobic side chains in system V, as a distinct hydrophobic collapse is observed in systems IV and V. Figure 3.10 shows the time evolution of the number of water molecules per peptide, around the first hydration shell of hydrophobic side chain beads (N_w), and the number of interpeptide hydrogen bonds (N_{hb}), for a 12 peptide system.

In total, we observe four mechanisms of water expulsion: In 63.5% of the cases, as shown in Figure 3.10a, water expulsion is a single step process, followed by peptide reorganization, as described above. In this case two individual aggregates are formed initially within the first 2ns. These aggregates fuse to form one large aggregate by 7ns, after which N_w values remain constant. Similarly, a steep increase in N_{hb} is seen after 2ns, which further increases after the formation of the large aggregate at 7ns, indicating structural reorganization. Insets in Figure 3.10a, show the two initial aggregates and the larger aggregate, formed at 2ns and 7ns, respectively. In 12.5 % of the cases the expulsion of water is coupled with structural ordering (Figure 3.10b). That is, there is an increase in water expulsion (or decrease in N_w) with increase in pseudo H-bond content, with time. As the peptides collapse, there is simultaneous ordering. The inset of Figure 3.10b shows a representative partially ordered conformation. In 12.5% of the cases, N_w and N_{hb} are initially correlated, till 4ns, when N_{hb} continues to increase, while N_w remains constant (see Figure 3.10c). That is, within the first 4ns, increase in water expulsion (or decrease in N_w) is coupled

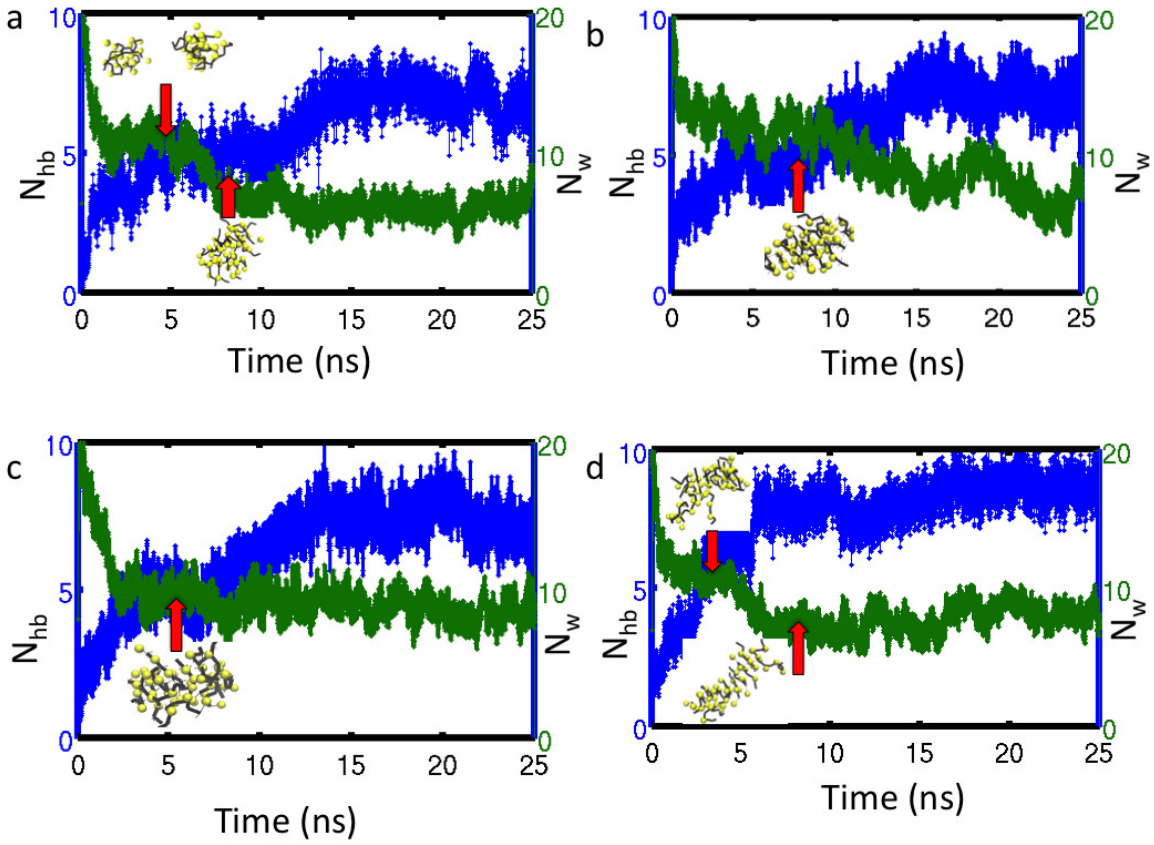

Figure 3.10: Time evolution of the number of water molecules per peptide (N_w) in the first hydration shell of hydrophobic side chain beads (green), and the number of pseudo-interpeptide hydrogen bonds (N_{hb}) formed (blue). (a), (b), (c) and (d) represent four distinct and representative trajectories for system V. Typical conformations shown as insets, side chain beads represented in yellow and backbone beads in black.

with increase in H-bond content, while after 4ns, the expulsion of water from the hydrophobic core is complete, but the number of H-bonds is still increasing, thus indicating structural ordering. The inset of Figure 3.10c shows a representative disordered, collapsed conformation at 5ns. In the case of the pathway that leads to a "fibril-like" conformation (12.5%) (Figure 3.10d), a small nucleus of ordered

structure inside an aggregate is formed within 5ns (see first inset), as indicated by the initial drop in N_w while N_{hb} is still increasing. This nucleus precedes the ordering of other peptides in the aggregate. The second drop in N_w denotes further ordering of the peptides that results in a "fibril-like" conformation, as shown in the second inset of Figure 3.10d at 10ns. In this case, water expulsion from hydrophobic side chains is influenced by the interpeptide backbone dipole interactions.

3.4.4 Effect of Water-Hydrophobic Liquid Interface

Figure 3.11 compares the conformational frequency between 12 peptide systems (a) in water (system V, blue bars), (b) in the presence of a hydrophobic interface (system VI, green bars) and (c) without dipolar particles (red bar). The presence of a hydrophobic surface influences aggregation morphology by shifting the conformational equilibrium. In water, two distinct types of conformations are seen, (a) a cross-β like conformation with a frequency of 0.6, and (b) an extended fibril-like conformation, with a frequency of 0.1. Both conformations are seen with 12 and 8 peptides. Studies on $A\beta_{1-40}$ show that within 6-10 monomer chains, cross-β like order is seen [41]. The "fibril-like" conformation is more water exposed (red curve in Figure 3.3b) than the "cross-β-like" conformation (blue curve in Figure 3.3b), as evident from the RDF between water and hydrophobic side chains beads. We refer to the dominant closed conformations as "cross-β-like" as they are a pair of ordered β-sheets with side chains of the two sheets interdigitated in a dry hydrophobic core (see Figure 3.12d) [123, 124]. These structures are similar to the MVGGVV microstructure crystallized

by Eisenberg's group [125].

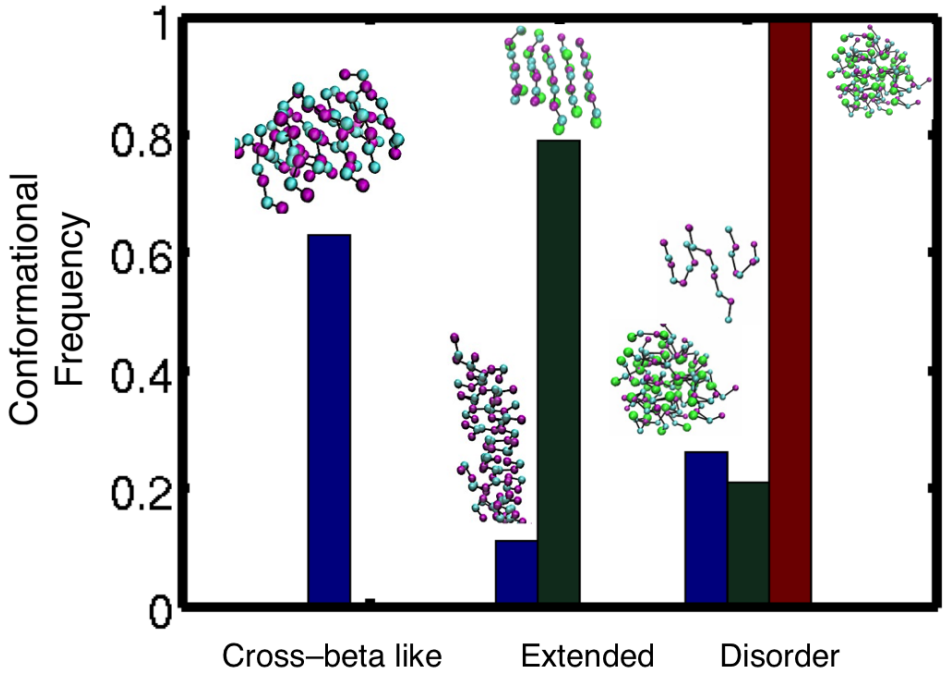

Figure 3.11: Conformational frequency of 12 peptides system V (blue), VI (green), and control system without dipolar particles in a water environment (red). Representative conformations are shown as insets, backbone beads represented in cyan (hydrophobic residue) and purple (neutral residue). Hydrophobic side chain beads shown in green.

With the presence of a hydrophobic surface there is a conformational shift to "fibril-like" structures, with the hydrophobic beads partitioning into the hexadecane phase (Figure 3.18 c). The frequency of ordered, extended conformations in the presence of an interface is 0.8. Another important feature is the decrease in disordered conformations by about 10% in the biphasic system compared to bulk water. The disordered conformations seen at the interface are smaller in size, consisting of 3

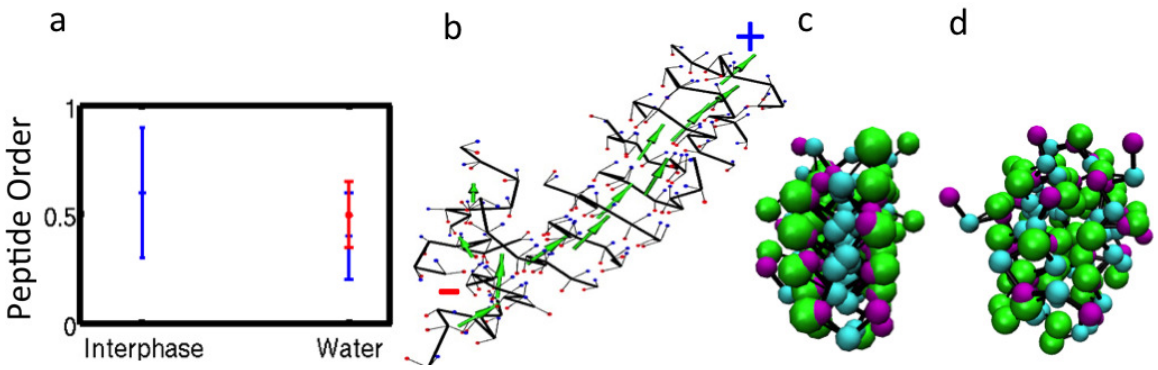

Figure 3.12: (a) Average peptide order parameter of aggregates in system V and VI (blue), the "fibril-like" conformation seen in water is represented by the red points. All error bars represent 95% confidence interval for the mean (assuming normal distribution) of collective data, as standard error of the mean is negligible due to large number of conformational information collected. Representative conformation of fibril-like structure, (b) showing dipole alignment, (c) lateral view displaying hydrophobic bead alignment on either sides. Representative conformation of cross-β structure seen in system V, (d) lateral view displaying hydrophobic core. Green arrows in (b) represent dipole vectors of each peptide, red and blue represent negative and positive dummy particles. Backbone beads in (c) and (d) represented in cyan (hydrophobic residue) and purple (neutral residue). Hydrophobic side chain beads shown in green.

or less peptides, as the peptides can interact with two water-hexadecane interfaces (see Figures 3.2). Partitioning of valine or hydrophobic residues into hexadecane restricts or constrains the peptides to two dimensions. This restriction increases the probability of peptides colliding as the local concentration increases, which can in turn lead to an increase in peptide-peptide hydrogen bonds and hence, aggregation.

Insets in Figure 3.11 show representative conformations.

Figure 3.12a shows the difference in order parameter P2 for aggregates in water ($\langle P2\rangle$=0.48) and in the presence of an interface ($\langle P2\rangle$=0.65). The "fibril-like" conformations seen in water are slightly more ordered ($\langle P2\rangle$=0.52, red point in Figure 3.12a) than the average, however, the presence of an interface results in a significant increase in P2 values. Surface adsorption of the peptide enhances order, as has also been observed in atomistic studies of $(GV)_4$ [100, 126, 127]. The presence of a surface can lower the entropic penalty to form an ordered state. As shown in Figure 3.12b, the fibril-like conformations, both in water and at interface, exhibits Pauling and Corey's α-sheet structure [128]. All the negatively charged dipole particles are oriented on one side of the sheet, with all the oppositely charged ones aligned on the other side, as shown in Figure 3.12b. The alignment of the dipoles is denoted by green arrows in Figure 3.12b. This distribution of partial charges from the peptide backbone, creates a distinct molecular dipole. α-sheets or "polar pleated sheets" have not received much attention since it is rare in crystal structures. However, recent studies suggest the possible involvement of α-sheets in early stages of amyloidosis [129, 130].

3.4.5 Pathways of Peptide Aggregation on Hydrophobic Interface

Figure 3.13 details different mechanisms of surface mediated aggregation observed in system VI. We see 5 distinct pathways, of which 4 dominate or are more prevalent. Since there are two interfaces, the peptides get adsorbed to either. In mechanism (a), peptides adsorb to the surface individually, an ordered nucleus of 4 peptides is formed

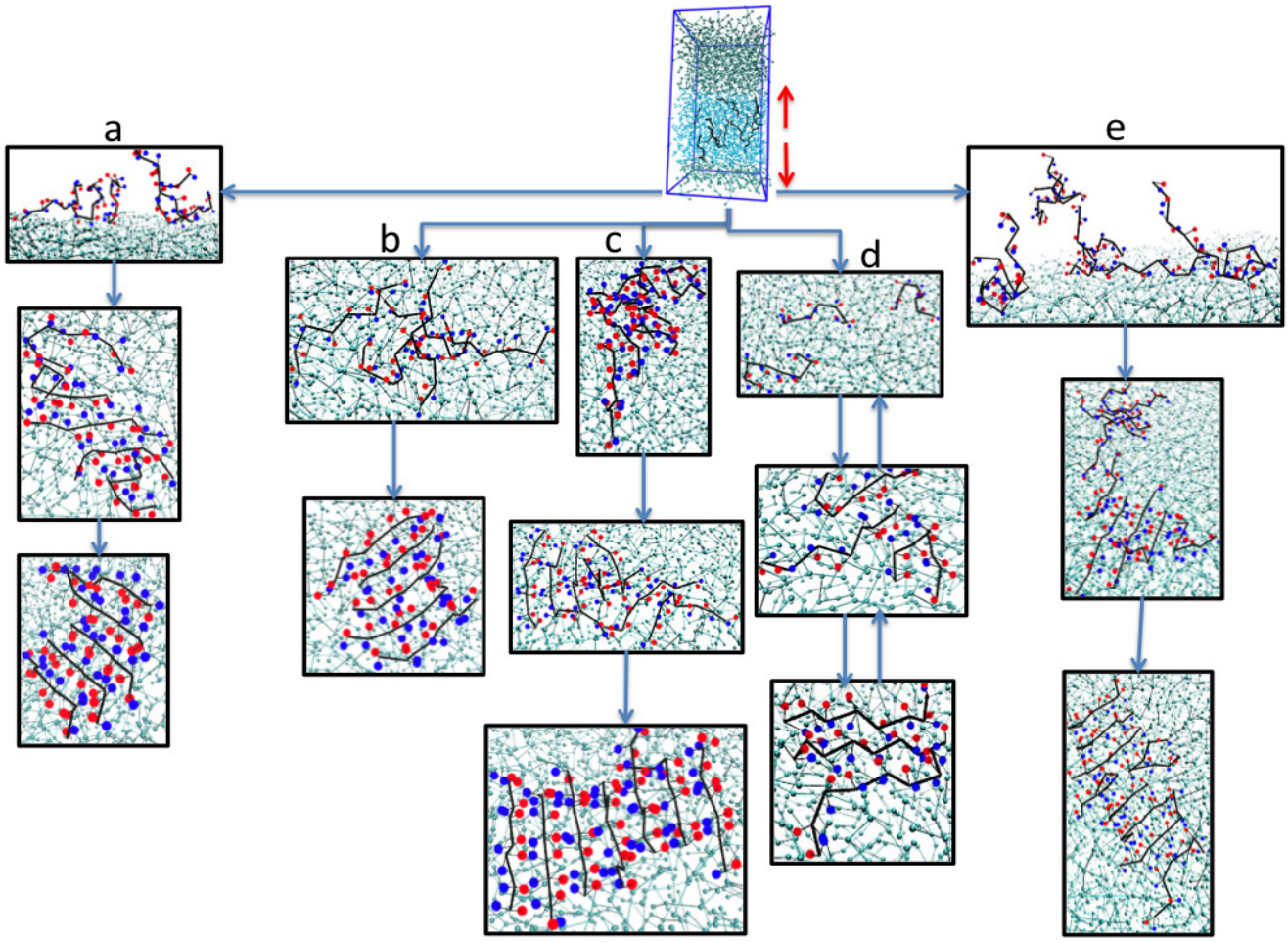

Figure 3.13: Aggregation pathways observed in system VI, red arrows indicate that peptides aggregate at both interfaces; light blue represents water; black, the protein backbone; red and blue represent negative and positive dummy beads; and cyan represents hexadecane phase. (a), (b) ,(c) ,(d) and (e) represent five different mechanisms, see text for details.

and the fifth peptide adds on to the ordered aggregate (fraction observed: 0.0625), in (b) the peptides adsorb to form a disordered aggregate on the surface, which rearranges to form ordered conformations (fraction observed: 0.1875). The third pathway (c) is the most common (fraction observed: 0.375), and is a condensation-ordering

mechanism where, the peptides aggregate in water and then the aggregate gets adsorbed on the surface which realigns with time. Mechanism (d) is observed when three (or less) number of peptides get adsorbed to a surface (fraction observed: 0.1875). In this case, the aggregates are not stable, and can be ordered or disordered. Finally, in mechanism (e), peptides get adsorbed to the surface, form different aggregates (in this example, of size 4 and 5), which then fuse to form one ordered structure (fraction observed: 18.75). Also note, that some peptides can occasionally adopt a hairpin conformation in the aggregate.

3.4.6 Kinetics and Mechanism of Aggregation

A comparison of kinetic properties of aggregation in water and the more probable aggregation pathway in biphasic systems is depicted in Figures 3.14a-b (another set of trajectories is represented in Figure 3.15). Based on the insets of Figures 3.14a-b (red curves), the "lag phase" which precedes ordered aggregation is more prominent in water ($\approx$ 3ns) than in the presence of an interface ($\approx$ 1ns). In water, the monomers (M) (green curve) aggregate to form an intermediate disordered state (I) (blue curve), which after 25ns, reorganizes to form ordered sheets (O) (red curve). Representative conformations are shown in Figure 3.14d. Whereas, when the water-hexadecane surface is present, the monomers form sheets in less than 10ns (see red curve). Even though there is an intermediate conformation present, this state is short lived in comparison to the intermediate conformation observed in water (see blue curve of Figure 3.14a inset). The nature of the ordered fraction curves (red) is

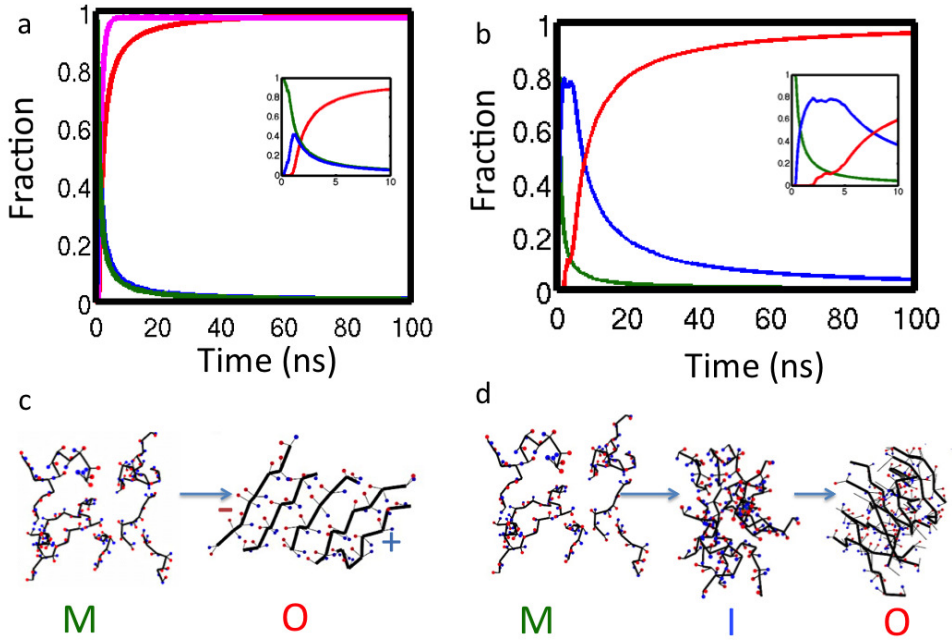

Figure 3.14: Time evolution of the fraction of different species in 12 peptides system (a) VI and (b) V. Green represents monomer fraction; blue, intermediate aggregate fraction, pink is a negative exponential fit and red, ordered aggregate conformation. (c) Representative pathway for ordered aggregate formation at hydrophobic-water interface, monomers [M] form ordered aggregates [O] with shortly lived intermediates. (d) Representative pathway for ordered aggregate formation in explicit water, monomers [M] form intermediate aggregates [I] which rearrange to form ordered conformation [O].

more exponential in the biphasic system (negative exponential fit shown in pink in Figure 3.14a) than in water, implying a more cooperative process. Representative conformations are shown in Figure 3.14c, note the "α-sheet" like final conformation. Thus the presence of the water-hydrophobic interface, aids or accelerates the rate of

sheet formation, relative to water, as has been observed experimentally [131].

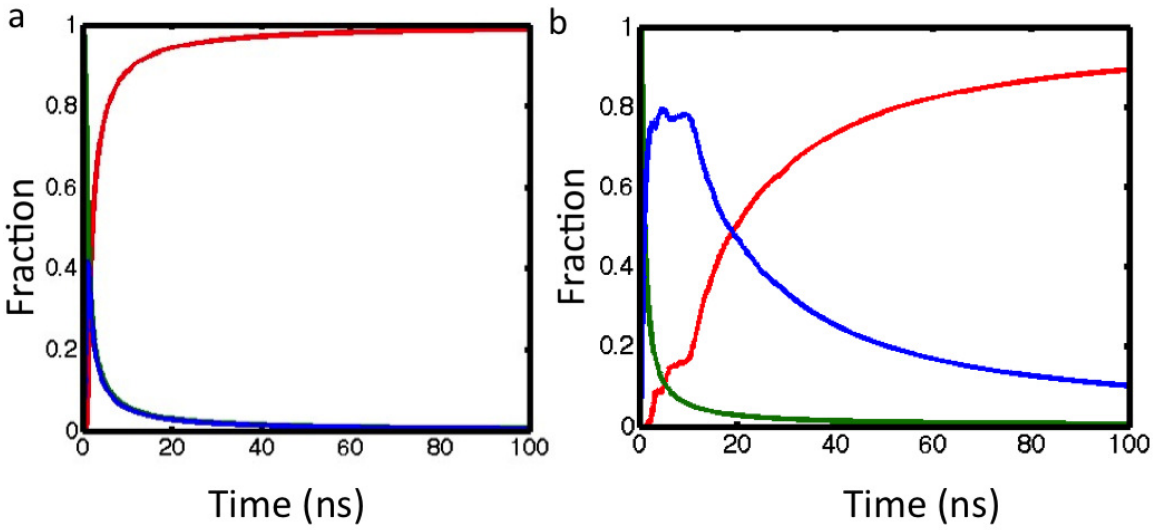

Figure 3.15: Time evolution of the fraction of different species in (a) system VI and (b) system V. Green represents monomer fraction, blue, intermediate disordered fraction, and red, ordered aggregate conformation.

At 300K, we see unidirectional progression of aggregation, thus the mechanism is downhill. As one might expect, ordered aggregation is dependent on temperature. Figure 3.16 represents average (over 8 runs) monomer (green curve), disordered aggregate (blue curve) and ordered aggregate (red curve) fraction at different temperatures of system V. Aggregates formed are stable and ordered till 350K. This is consistent with other simulation results that show a range of temperatures over which fibrils are formed [132,133]. However, on further increase in temperature, the probability of observing ordered aggregates drops, and is 0 at 400K, with 375K being the transition temperature. At high temperatures, the probability of observing stable aggregates drops [134].

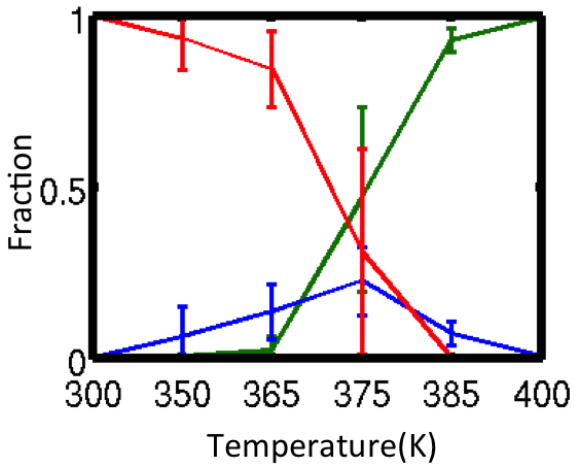

Figure 3.16: Fraction of monomer (green curve), disordered aggregate (blue curve) and ordered aggregate (red curve) for system V. Data averaged over 8 runs for each temperature.

Figure 3.17a and b represent kinetic properties of aggregation in water (solid lines) and at interface (dashed lines), for polyG octapeptides (Figure 3.17a) and polyV octapeptides (Figure 3.17b). In the case of polyG, the monomer fraction stays at 1 throughout the 100ns simulation (green curve in Figure 3.17a). Therefore, polyG octapeptides do not aggregate in water as backbone dipoles of glycine residues prefers to interact with water. Since glycines are neutral, when a hydrophobic interface is present the peptides do not partition to the hydrophobic interface, and hence do not aggregate at the interface either. In the case of polyV octapeptides in water, a disordered aggregate is formed within the first 10ns (blue solid curve in Figure 3.17b), however, the fraction of ordered aggregate (red solid curve in Figure 3.17b) does not significantly increase with time and converge at a fraction of 0.23. For polyV octapeptides at the interface, there is partitioning of the hydrophobic side chains

within the first few ns, and the peptides diffuse to form fully ordered conformations within the first 20ns (dashed red curve in Figure 3.17b). This behavior of polyV octapeptides at interface is similar to that of GV_4.

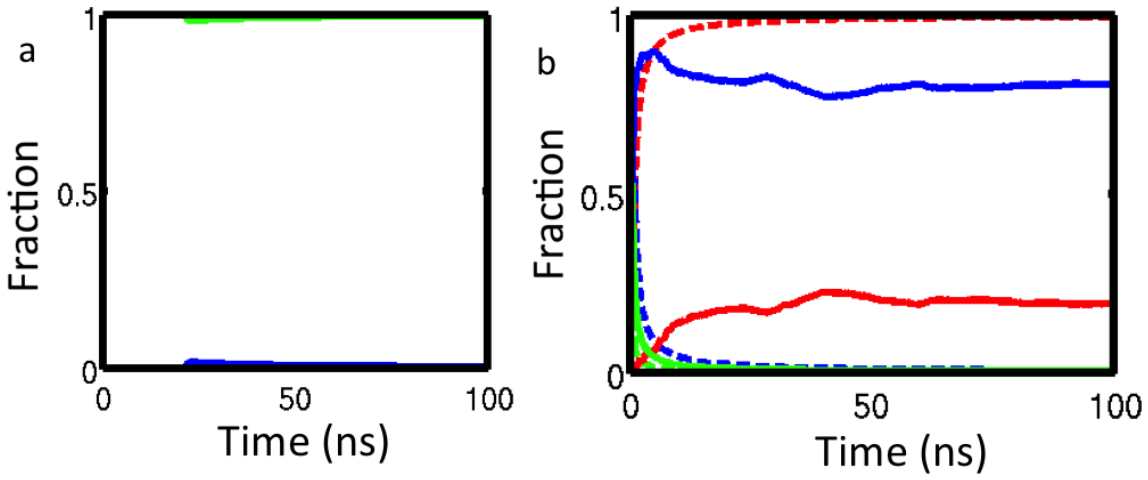

Figure 3.17: Time evolution of the fraction of different species in (a) polyG octapeptides and (b) polyV octapeptides. Green represents monomer fraction, blue, intermediate disordered fraction, and red, ordered aggregate conformation.Dashed lines represent data at interfaces and solid lines, in water.

3.4.7 Role of Dipole Interactions

To further investigate the role of dipolar interactions, systems V and VI (12 peptides system with and without interface, respectively) were simulated without dipolar particles. In water, the peptides aggregate due to the hydrophobic effect, however, the aggregates are disordered owing to a lack of pseudo interpeptide H-bonds. A representative collapsed conformation is shown in Figure 3.18b. To quantify the ag-

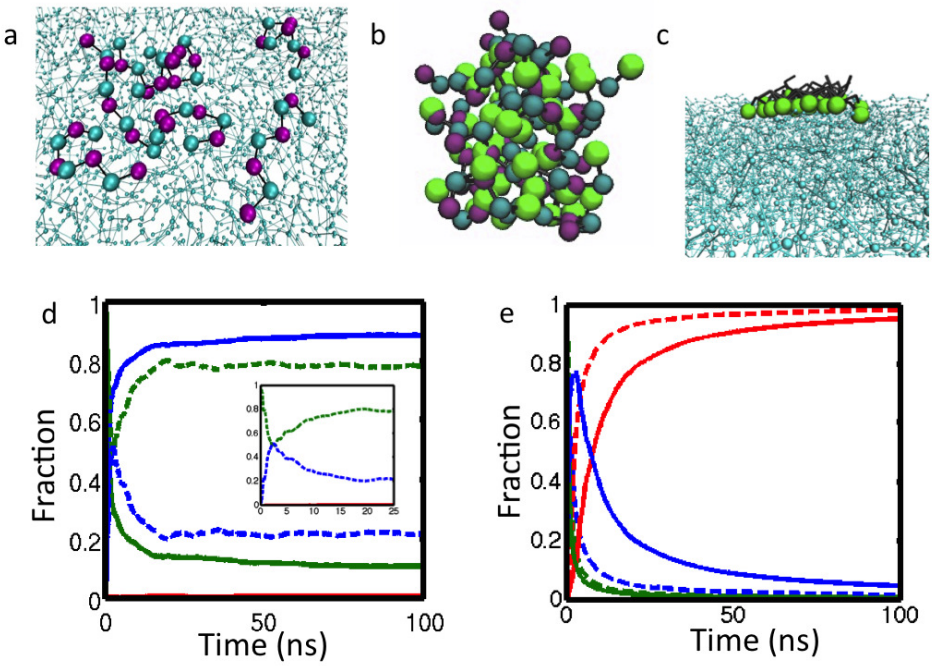

Figure 3.18: Representative conformations of 12 peptides system (a) VI and (b) V without dipolar particles. Cyan and purple beads correspond to backbone representation of hydrophobic and neutral residues respectively. Hydrophobic side chain shown in green. (c) Partitioning of hydrophobic side chain beads (green) to the hexadecane phase (cyan) for system VI with dipolar interactions. Peptide backbone shown in black. Time evolution of the fraction of different species, using the backbone distance cutoff in (d) system VI (dashed lines) and system V (solid lines) without dipolar particles, and (e) system VI (dashed lines) and V (solid lines) with dipole particles. Green represents monomer fraction, blue, intermediate aggregate fraction and, red, ordered aggregate.

gregation pathway, we estimate kinetic parameters using backbone bead cutoffs (see Methods section). This cutoff is defined because the control systems do not have

dipole particles, and hence lack interpeptide pseudo hydrogen bonds.

As can be seen from Figure 3.18d, the monomers (solid green curve) interact to form disordered aggregates (solid blue curve). Since there are no dipolar interactions, there is no order in the aggregate. The ordered conformational fraction remains at 0 (solid red curve). To compare this control run with system V, the same criteria, and cutoff is applied to a representative replicate where dipole interactions are taken into account. Figure 3.18e (solid curves) displays a similar trend as seen in Figure 3.18b (discussed above) for the bulk water environment. That is, the monomers aggregate within a few ns to form a disordered aggregate, which in turn rearranges to form ordered aggregates after 25ns.

In the presence of an interface, the peptides(without dipolar interactions) get adsorbed to the surface, due to partitioning of hydrophobic side chains. Representative conformations are shown in Figures 3.18a and 3.18c. However, due to the lack of interpeptide dipole interactions, the peptides do not aggregate on the interface, and are free to diffuse individually. Since the hydrophobic side chain can partition to hexadecane, the entropy is driving the peptides to not aggregate. Based on this, we conclude that at hydrophobic interfaces, the major driving force for peptide aggregation is dipolar interactions, which in our model mimics hydrogen bonding. Figure 3.18d (dashed lines), further elucidates this point. The monomer fraction (green dashed curve) decreases as the peptides aggregate and reach the interface, however, there is an increase soon after 5ns (see inset of Figure 3.18d). This is due to the fact that the monomers without dipolar particles, on reaching the interface, are free to diffuse. Since the hydrophobic side chains remain buried in hexadecane there is

no other driving force to keep the peptides aggregated. Whereas, system VI, that contains dipolar interactions (see Figure 3.18e), forms an ordered aggregate (dashed red line) within the first 10ns.

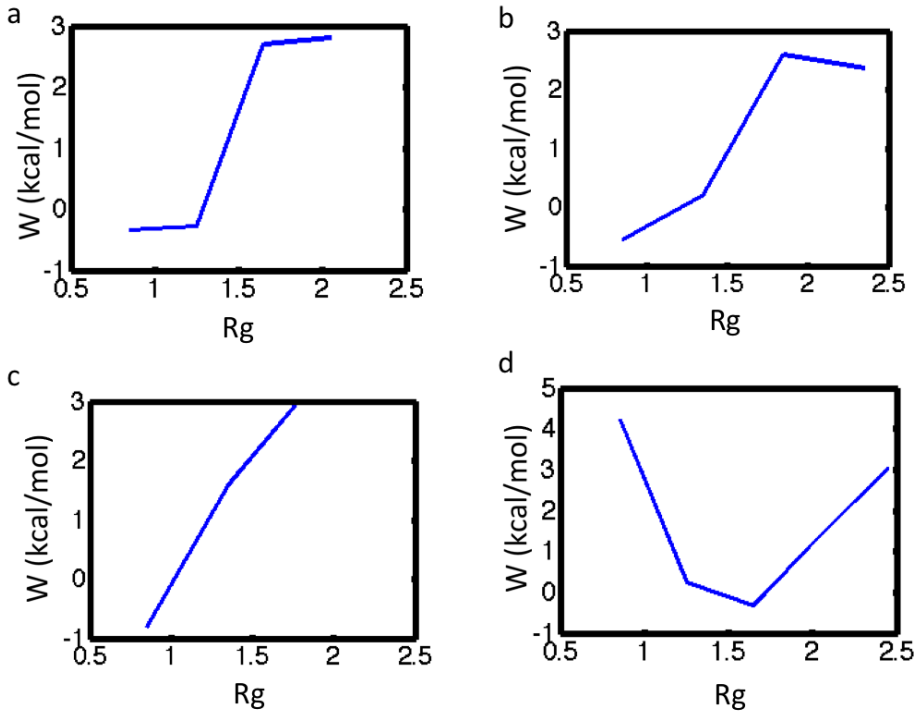

Figure 3.19: PMF as a function of the peptide aggregate radius of gyration (Rg). PMF for peptides with dipoles (a) in explicit water and (b) at the interface; and peptide aggregates without dipoles (c) in explicit water and (d) at the interface. All represented ensembles obtained at 300K.

To further quantify these processes, we looked at PMF (W) of peptide aggregates with respect to R_g. Figures 3.19 a-b represents PMF of systems with dipoles in water and at the interface, respectively. Both these systems display clear minima for lower values of Rg (Rg <1nm), which correspond to ordered aggregates. These curves also display a sigmoidal trend, consistent with cooperative processes. Figures 3.19c-d

represents PMF of systems without dipoles in water and at the interface respectively. Figure 3.19c clearly shows a minimum corresponding to the aggregated state (Rg <1nm), this corresponds to the disordered state originating from a hydrophobic collapse (see Figure 3.18b). Whereas, Figure 3.19d shows a minimum for states with larger Rg (Rg >1.5nm), as these peptides do not form aggregates (see Figure 3.18a).

3.5 Conclusion

In this study, we have used WEPPROM to study peptide aggregation of $(GV)_4$ octapeptides. Many of our results are concurrent with all-atom aggregation studies on $(GV)_4$. For example, in all-atom studies, kinetics and mechanism of aggregation at biphasic interfaces (octane-water) are observed to be different than in aqueous solvent [100]. The preliminary step for β-sheet formation at octane-water interfaces is also the initial partitioning of nonpolar side chains. The adsorbed peptides diffuse in 2D before forming intermolecular hydrogen bonds, that brings order to the aggregates. Both hairpin-like and fully extended conformations are observed on the interface and in water. All of which are observed in our study. However, in atomistic studies, not all peptides that adsorb to the surface form aggregates. This is due to a time lag in peptide diffusion as all-atom studies are limited by time scale. From our CG studies, we have been able to observe a difference in balance between hydrophobic and backbone dipole-dipole interactions, between amphipathic aggregating peptides in water and at a hydrophobic interface. The dipole interactions plays a more significant role in driving aggregation at interface.

We observe a cooperative effect in interpeptide pseudo hydrogen bonding with aggregate size, that stabilizes at aggregate size 4. That is, the backbone dipole moment and order increases non-linearly up to 4 layers and then levels off. These dipole interactions, within the β-strands are cooperative, with contributions from several layers away within the ordered aggregate. The backbone dipoles get aligned with the aggregate electric field up to 4 peptide layers, where it levels off at 40 degrees. That is, the tetrameric GV_4 species is the smallest, stable aggregate that has the highest backbone dipole moment. Studies on Amyloid-β oligomers, have also identified trimeric and tetrameric species to be stable, long-lived oligomers that might play a role in aetiology of the disease [135, 136].

The process of $(GV)_4$ aggregation in water mostly follows a two step condensation-ordering mechanism, however other pathways of water expulsion are observed. Disordered aggregate conformations are observed with poly-valine octapeptides in water, suggesting the influence of sequence patterning in ordered aggregation. Without dipolar interactions, the disordered aggregate does not rearrange into a fibril-like ordered conformation. . Therefore, a balance between hydrophobicity and dipolar interactions is needed to fold correctly [110], or to self assemble into fibril like aggregates. This balance was achieved while parameterizing WEPPROM [110], where too much or too less hydrophobicity resulted in collapsed or unfolded peptide conformations. The aggregation pathway in water exhibits two major off-pathway ordered aggregates, cross-β type and extended fibril-like structures. The extended fibril-like structure exhibits a water solvated hydrophobic face. The formation of the pseudo H-bond network in this structure compensates for the exposure of the hydrophobic

groups to the water environment.

On comparison with aggregation at hydrophobic-hydrophilic interfaces, we observe that the presence of an interface (a) increases order in the final aggregate conformations, (b) decrease disordered conformations explored by the trajectory and (c) increases rate of aggregation; as the aggregates better align with the local electric field. On characterizing the angle between the dipole moment vectors and the local electric field for aggregates formed on the interface, a higher alignment of $\theta \approx 30 \pm 5^{\circ}$ is observed. When the interface is present, there is backbone dehydration, leading to more stronger dipole interactions, and hence better alignment with the local electric field. With the interface, there is less competition to form dipole-dipole interactions between backbone beads and the solvent which can introduce distortions into the pseudo H-bond network that can cause a decrease in order. The presence of a hydrophobic-hydrophilic interface also decreases the lag phase, or the time period before the formation of ordered aggregates. Also, the kinetics of aggregation is also more exponential or cooperative in nature when the interface is present. While fibril-like aggregates dominate conformations seen at the interface, cross-β-like conformations are more probable in the aqueous environment, however, fibril-like conformations in the aqueous environment is also observed. We see the formation of α-sheet like structures in all ordered fibril-like

Dipolar interactions play a crucial role in peptide aggregation, irrespective of environment. The presence of dipoles, both (a) stabilizes the aggregate and (b) induces order, which is made clear in this study by drawing comparisons between systems with and without dipolar particles. For peptides without dipolar particles, ordered

aggregates are not observed in aqueous solvent and the peptides do not assemble or aggregate at the hydrophobic interface due to the lack of a driving force. The balance between hydrophobicity and dipolar interactions are different for aggregating peptides in water and at the hydrophobic interfaces. Hydrophobic interactions between peptides is lesser at the hydrophobic-hydrophilic interface, thus dipolar interactions play a more significant role in ordered aggregation at those interfaces.

Chapter 4: Effect of Lipid Head Group Interactions in Membrane Properties and Membrane-Induced Cationic β-Hairpin Folding

4.1 Overview

This chapter is based on the author's submitted work: Effect of Lipid Head Group Interactions in Membrane Properties and Membrane-Induced Cationic β-Hairpin Folding; Sai J. Ganesan, Hongcheng Xu and S. Matysiak

4.2 Introduction

Zwitterionic phospholipid phosphatidylcholine (PC), and anionic phospholipid phosphatidylserine (PS) comprise 40-55% and 3-10% respectively, of total mammalian cell membrane phospholipids [137]. Their structural and dynamical properties have been found to play important roles in a number of biological processes. Electrostatic interactions between lipid head groups have an effect on a membrane's internal electrical dipole potential, which varies from 100 mV to 400 mV, depending on the composition of lipids [138]. This dipole potential has also been shown to dramatically impact ion channel permeability in biological membranes [139].

Biological membrane interfaces (mIF) provide a unique dielectric environment in which proteins undergo conformational transitions from a water-soluble to a membrane associated state [140,141]. Short model peptides, especially antimicrobial peptides (AMPs), have been extremely useful in characterizing energetics of interfacial folding [142,143]. AMPs are cationic peptides with a significant level of hydrophobicity. Anticancer peptides (ACP) are AMPs designed to target tumor cells, one such *de novo* designed ACP is SVS-1 ($KVKVKVKV^DP^LPTKVKVKVK-NH2$) [144]. SVS-1, like AMPs, are disordered in the aqueous phase (bioinactive), but is fully structured upon partitioning onto an interface (bioactive) [144]. This ACP is known to fold into a β-sheet on interaction with negatively charged vesicles [144]. The literature on experimental and computational characterization of biophysical properties of AMPs is vast [145–148]. It has been proposed that the energetic cost of partitioning unfolded peptides into mIFs is reduced by secondary structure formation or intermolecular hydrogen bonds [149]. Membrane lipid composition is known to play a crucial role as well; for example, differences in the amount of acidic membrane phospholipids and cholesterol are known to play a critical role in specificity of magainins [150,151]. However, the balance of driving forces between the two states (water soluble and membrane bound) remains to be understood. Coarse-grained membrane models that capture the right dielectric gradient, and peptide models that can capture protein secondary structures should have essential ingredients to decode such a process.

Atomistic simulations have contributed to the understanding of many membrane processes [152–156], including the existence of anionic lipid clusters, mediated by

ion-dipole or hydrogen bond (a type of dipole-dipole interaction) networks in both monocomponent and mixed bilayers [157–159]. It has been hypothesized that these clusters could be intermediate structures on pathway to experimentally observed lipid phase separation in mixed PC/PS bilayers on longer time scales [160]. CG simulations of lipid systems have largely proven to be efficient in giving us a thorough and coherent picture of membrane structure and have been used in the past to explore lipid domain formation in mixed bilayers for systems that do not have anionic lipids [161–163]. There exist a large number of CG models that have yielded significant results and extended our understanding of membrane molecular processes [1, 164–168]. Among them, a transferable model called MARTINI force field [1, 168], built on thermodynamic data of oil/water partitioning coefficient, achieves a broader range of applications without the need for re-parametrization.

In this chapter, we present a CG lipid model that can be used to explore the role of head group dipoles in membrane structure and interfacial peptide folding. This model has roots in the MARTINI force field, and is combined with a new Water-Explicit Polarizable PROtein Model (WEPPROM) described in chapter 2 [30] and Yesylevskyy's polarizable water model [169]. By modeling a protein backbone bead as a flexible dipole, we were able to achieve *de novo* helix and sheet content without any biases. In WEPPROM, the dipolar interactions can be considered as pseudo hydrogen bonds, which contribute to cooperativity in folding secondary and super-secondary structures. An analog to our model is the multipole CG model developed by Ren et al [170]. By adding structural polarization to some polar groups of a lipid model, to capture the dipole interactions that can exist in the head group region of

anionic bilayers. The change in orientation of atoms underlying polar CG units of the lipids are captured by a flexible dipole inside each polar CG unit. This flexible dipole is created by angular changes in oppositely charged dummy or dipolar particles, which are constrained to the center of mass site. Dipolar particles interact with each other and with charged beads through Coulombic potentials, introducing structural polarization into the model.

We have chosen a zwitterionic lipid, 1-palmitoyl-2-oleoyl-*sn*-glycerol-3-phosphatidylcholine (POPC), and an anionic lipid, 1-palmitoyl-2-oleoyl-*sn*-glycerol-3-phosphatidylserine (POPS), as model lipids. The choice of the above two lipids is governed by the use of POPC/POPS mixed systems as common models in the study of plasma membranes [171, 172]. In this chapter, we explore (a) the role of head group dipole interactions in membrane structure and dynamics, (b) the effect of monovalent ions on lipid dipole interactions and bilayer properties, and (c) membrane-induced folding of SVS-1.

4.3 Methods

4.3.1 Lipid Model

A mapping scheme consistent with the MARTINI model for POPC and POPS lipids is used, and is shown in Figure 4.1a. A phospholipid molecule is mapped onto a structure consisting of 13 CG sites made of 3 different bead types. The bead types used are: charged *(C)*, polarizable *(Pol)*, and hydrophobic *(H)*. We also use a set of bead subtypes similar to the MARTINI force field, with distinct modifications in

Table 4.1: Table of vaporization, hydration and partition free energy in kcal/mol. The partition free energy is evaluated for water/hexadecane interface. $\Delta G^{\mathbf{M}}$ is the free energy calculated using the MARTINI model [1], $\Delta G^{\mathbf{P}}$, with our water-explicit polarizable coarse-grained model, and $\Delta G^{\mathbf{E}}$ is the free energy from experiment [1].

Bead	Chemistry	Examples	$\Delta G^{\mathbf{M}}_{vap}$	$\Delta G^{\mathbf{P}}_{vap}$	$\Delta G^{\mathbf{E}}_{vap}$	$\Delta G^{\mathbf{M}}_{hyd}$	$\Delta G^{\mathbf{P}}_{hyd}$	$\Delta G^{\mathbf{E}}_{hyd}$	$\Delta G^{\mathbf{M}}_{part}$	$\Delta G^{\mathbf{P}}_{part}$	$\Delta G^{\mathbf{E}}_{part}$
C0	C_3N^+	choline	-	-	-	-6.0	-6.0	-	<-7.2	<-7.2	-
C+	H_3N^+-C_3	1-propylamine	-	-	-	-6.0	-6.0	-	<-7.2	<-7.2	-
C-	PO_4^-	phosphate	-	-	-	-6.0	-6.0	-	<-7.2	<-7.2	-
Pol1	H_2N-C_2=O	acetamide	sol	sol	sol	-6.7	-6.9	-9.6	-6.7	-6.9	-6.5
Pol2	C-O-C=O	methylformate	-3.1	-2.2	-3.8∼-5.5	-2.2	-2.4	-2.9∼-3.8	-1.7	-1.9	-1.0∼-1.4
H1	C_4	butane	-2.4	-2.4	-2.6	3.3	4.5	2.2∼2.4	4.3	5.0	4.3
H2	C_2=C_2	2-butene	-2.4	-2.4	-3.8	1.2	3.8	-0.2∼-0.5	3.1	4.1	2.9

the Lennard-Jones (LJ) parameters, to account for all the CG sites. *C0*, *C+* and *C-* are charged bead subtypes, where *C+* is a representative hydrogen bond donor, *C-* acceptor, and *C0* is neither. *Pol1* and *Pol2* are subtypes of the polarizable bead, sorted in order of decreasing polarity. *H1* and *H2* are subtypes of the hydrophobic bead, in decreasing order of hydrophobicity. As depicted in Figure 4.1a, the PC head group region consists of two hydrophilic groups: choline (NC3) and phosphate (PO4) with *C0* and *C-* bead types respectively. The PS head group region also consists of two hydrophilic groups: serine (CNO) with oppositely charged dummy particles (CNM and CNP), as shown in Figure 4.1b, and phosphate (PO4), with *Pol1* and *C-* bead subtypes respectively. For both lipids, two sites of intermediate hydrophilicity (bead subtype *Pol2*) are used to represent the glycerol ester groups (GL1 and GL2), each

with oppositely charged dummy particles (G1M, G1P and G2M, G2P), as shown in Figure 4.1b. The oleoyl tail is modeled with 5 beads, 4 of *H1* subtype and a central bead of *H2* subtype (a less hydrophobic bead to model the double bond). The palmitoyl tail is modeled with 4 beads of subtype *H1*.

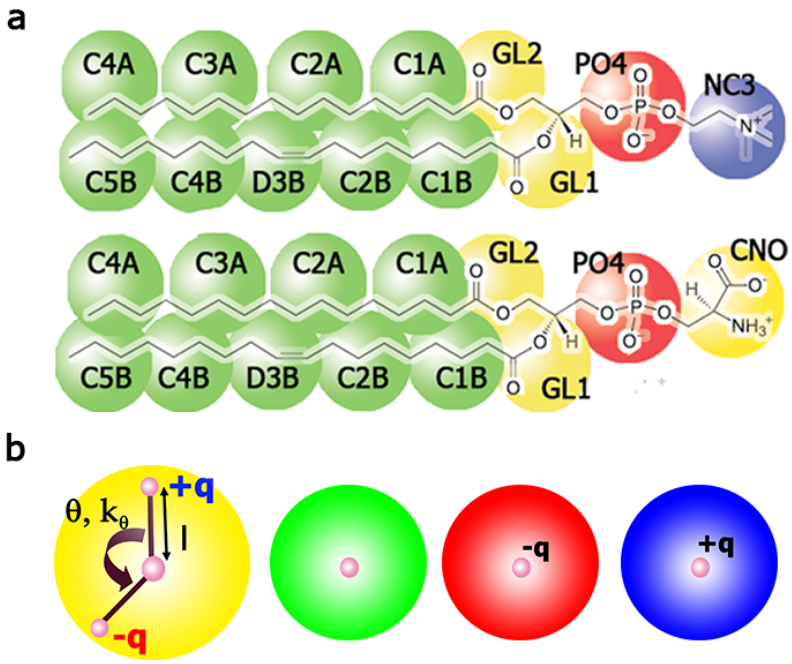

Figure 4.1: (a) Mapping scheme for POPC and POPS coarse-grained lipids; colors: green, hydrophobic bead; yellow, polarizable beads ; red, negatively charged bead; blue, positively charged bead. (b) Bead types: yellow represents polarizable beads (example : CNO, GL1, GL2), van der Waals radius of the bead encloses positively (+q/P) and negatively (-q/M) charged dummy particles (example:, CNP and CNM, G1P and G1M, G2P and G2M respectively) . The tunable parameters (l, q, θ, k$_\theta$) are depicted. Blue bead represents a positively charged bead, red bead represents negatively charged bead, and green represents hydrophobic bead.

The CG phospholipid model is combined with the polarizable coarse-grained (pCG) water model developed by Yesylevskyy et al. [169]. The pCG bead of our lipid model consists of three interaction sites, of which one is the center of mass site and the other two are dummy particles with opposite charges, as depicted in Figure 4.1b. The dummies are added into the polarizable bead only to create a flexible dipole which interacts with other particles via electrostatic interactions. The Lennard-Jones pairwise interactions are defined between the main CG sites. A constraint with a distance (l) is defined between dummies and the main site, and all the three interaction sites are bound by a cosine squared angle potential (equilibrium angle θ and angular force constant k_θ) to control the rotation of dummy particles. To avoid overpolarization, a small repulsive core is added to dummy particles, as commonly done in polarizable all-atom force fields [173]. All 1-2 non-bonded interactions are excluded between the main CG sites and their corresponding embedded dipole particles. In addition, the non-bonded interactions between dummy particles inside a polarizable bead are excluded as well. The mass of a CG bead (72 a.m.u) is distributed equally among the three particles (24 a.m.u. each) in polarizable beads.

4.3.2 Lipid Force Field Parameters

Our force field consists of bonded (harmonic bond and angular potential for lipid and peptide) and non-bonded terms (Lennard-Jones and Coulombic potentials). All non-dipolar bonded interactions are based on the MARTINI force field [1,168], and are fine-tuned using MARTINI's LJ parameter scale as a baseline. The bonded distance

between two adjacent head group beads is 0.37 nm and between adjacent tail beads is 0.47 nm, both with a bond strength of of 298.8 kcal/mol. The only angle defined among head groups are between the phosphate and ester beads (PO4-GL1-GL2), which is set to 120°. Angles involving tail groups are set to 180°. The interaction strength of both the angles are set to 6.0 kcal/mol. There is an exception for the double bond in the carbon tail, which is set to 120° with an interaction strength of 10.8 kcal/mol.

The parametrization of non-bonded terms is done in two stages to account for (a) thermodynamic parameters or free energy values of partitioning, hydration, and vaporization of each bead type, and (b) dipole moments of polarizable beads. The dipole moment of polarizable beads is initially parametrized to match that of the corresponding chemical group in atomistic detail from all-atom simulations. There are four parameters for the polarizable CG bead that can be tuned to obtain the desired average dipole moment (l, q, θ, k_θ). Since the polarization of the bead inevitably adds extra electrostatic interactions to the system, the lipid dipole moment and Lennard-Jones (LJ) interactions of polarizable beads are carefully tuned down as a compensation to match, as close as possible, the free energy of partitioning, hydration and vaporization, as depicted in Table 4.1, using the method outlined by Marrink et al. [1]. The final dipole parameters for the CNO bead, with an average dipole moment of 8.76 Debye, is l=0.20 nm, q=0.4557, θ=180°, k_θ=4.78 kcal/mol. For GL1/GL2 bead, with an average dipole moment of 1.35 Debye, is l=0.14 nm, q=0.175, θ=70°, k_θ=8.40 kcal/mol. The LJ parameters tuned down from the MARTINI model values corresponding to different chemical species are presented in Table 4.2. The LJ

interaction strengths are divided into nine levels as follows: O) ϵ=1.35 kcal/mol, I) ϵ=1.20 kcal/mol, II) ϵ=1.10 kcal/mol, III) ϵ=0.95 kcal/mol, IV) ϵ=0.85 kcal/mol, V) ϵ=0.75 kcal/mol, VI) ϵ=0.65 kcal/mol, VII) ϵ=0.55 kcal/mol, VIII) ϵ=0.50 kcal/mol. In addition, two hydrophobic interactions, H1-W and H2-W, are also scaled down to 10% to make the lipid model compatible with our protein model [30], i.e. lipid and the peptide model use the same hydrophobic scale. An effective size of σ=0.47 nm is used for all main CG interaction pairs in the LJ potential.

4.3.3 Peptide Model

The peptide model is described in chapter 2. The bead types of the protein model is largely consistent with the current lipid model, with an addition of a non-polarizable polar side-chain bead type *P*. SVS-1 sequence is mapped to our CG model using an hydrophobicity scale [141]. Residues are mapped into polar *(P)*, hydrophobic *(H)* and charged *(C)* . Valines and prolines are modeled as hydrophobic residues *(H)*, with one polarizable backbone bead *(Pol1)*, and one hydrophobic side chain bead *(H1)*. Lysines are modeled with three beads, a polarizable backbone bead *(Pol1)*, a hydrophobic side chain bead *(H1)*, and a positively charged second side chain bead *(C+)*. Threonine is modeled as a polar residue *(P1)* with one polarizable backbone bead *(Pol1)* and one non-polarizable polar side chain bead *(P1)*. Like the polarizable beads in the lipid model, the backbone coarse-grained bead consists of three interaction sites, the center bead BB and two dipole particles, BBm and BBp. The main site, the center of the BB bead, interacts with other CG beads through a pairwise Lennard-Jones (LJ) potential.

Dipole particles BBm and BBp are harmonically bound to the central particle BB (equilibrium distance l, force constant k_l), and carry a positive and negative charge of equal magnitude (q) respectively, as depicted in Figure 4.1b. These dipole particles interact with other particles via electrostatic interactions. A cosine squared angle potential (equilibrium angle (θ) and angular force constant (k_θ)) was used to control the rotation of BBm and BBp particles. For solvation, the polarizable CG water model was used [169]. Our model currently does not account for chirality of residues. The peptide model is used with a double well α dihedral potential between backbone beads (force constant of 1.2 kcal/mol) to remove background noise [174]

$$U_{dih}(\gamma_{ijkl}) = cos(3\gamma_{ijkl}) + cos(\gamma_{ijkl} + 60) \tag{4.1}$$

$U_{dih}(\gamma_{ijkl})$ has three minima, 60° (right helix) and 180° (sheet) of equal well depth, and -60° (left helix) of a lower depth, and γ_{ijkl} is the dihedral between 4 consecutive backbone beads.

4.3.4 Simulation Setup

For simulation parameters, refer Appendix A. The bilayer system is energetically minimized before an isothermal-isobaric (NPT) run, simulation data is collected for 200 ns, of which the last 100 ns is analyzed. Every membrane system studied (atomistic, MARTINI CG or pCG) is made of 240 lipids, 120 on each leaflet. A side view snapshot of POPS bilayer is illustrated in Figure 4.2a.

Simulations with 1M NaCl are performed for both POPS and POPC systems. To

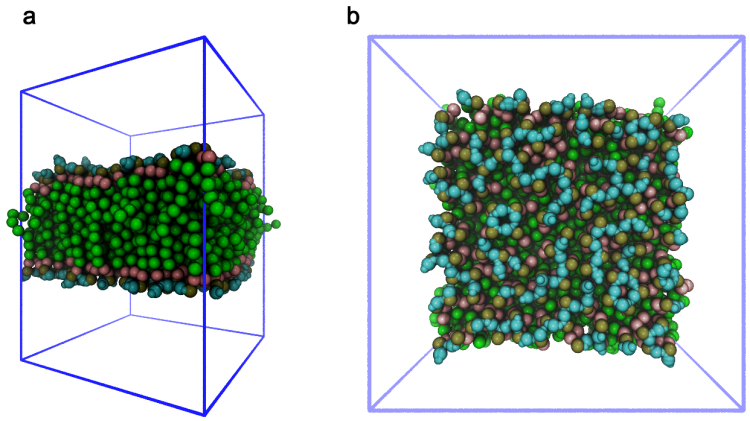

Figure 4.2: (a) Side view of POPS bilayer showing the lateral structure of the membrane. (b) Top view of POPS bilayer. Colors: serine (cyan), phosphate (tan), ester (pink), alkyl (green).

make comparisons with MARTINI force field, all 4 systems (POPC without NaCl, POPS without NaCl, POPC with 1M NaCl, and POPS with 1M NaCl) are simulated using both our pCG model as well as the MARTINI force field. The simulation setups used for pCG and MARTINI simulations are mostly identical. The only difference is the increase in time step with MARTINI force field (20 fs). This was done to maintain consistency. Explicit MARTINI polarizable water model is used for both pCG and MARTINI simulations [1, 169]. We also compared simulation performance between MARTINI force field and pCG, with polarizable water and POPC lipids (240 POPC lipids and 7757 water particles). For this comparison analysis, MARTINI parameters were borrowed directly from their study [1,169], while parameters detailed above were used for pCG. We found MARTINI simulations to be twice as fast as our model.

Table 4.2: Interaction strength ϵ for LJ interactions (kcal/mol)

Bead (Type)	C0	C+	C-	P1	Pol1	Pol2	W	H1	H2
C0	IV	VII	VII	III	O*	V	II	VII	VI
C+	VII	IV	III	III	O*	II	I	VII	VI
C-	VII	III	IV	III	O*	IV	I	VII	VI
P1	III	III	III	I	I	III*	I	VIII	VI
Pol1	O*	O*	O*	I	I*	I*	I*	VIII	VI
Pol2	V	II	IV	III*	I*	V	IV*	VI	VI
W	II	I	I	I	I*	IV*	III	VIII**	VI**
H1	VII	VII	VII	VIII	VIII	VI	VIII*	IV	IV
H2	VI	VI	VI	VI	VI	VI	VI**	IV	IV

(O: ϵ=1.35 kcal/mol, I: ϵ=1.20 kcal/mol, II: ϵ=1.10 kcal/mol, III: ϵ=0.95 kcal/mol, IV: ϵ=0.85 kcal/mol, V: ϵ=0.75 kcal/mol, VI: ϵ=0.65 kcal/mol, VII: ϵ=0.55 kcal/mol, VIII: ϵ=0.50 kcal/mol)

* 95% of the interaction strength is used to counterbalance the polarization

** 10% of the interaction strength is used to make this model compatible with our protein model [30] in hydrophobicity

Simulations with the peptide are performed with 240 lipids of polarizable POPS, polarizable POPC, POPS without dipoles, and in water. For systems with the peptide

and the bilayer, a random conformation of the peptide is introduced 5nm away from a self assembled bilayer. Counterions are added to neutralize the system. The peptide is constrained and a 10 ns NPT simulation is performed to allow the counterions to equilibrate. Constrains are removed to collect 300 ns NPT data, all of which are analyzed. For better sampling, we run 9 randomly constructed simulations of each pCG POPS system, and 6 runs for pCG POPC, POPS without dipoles (POPSnd), and in water. An image of the bilayer-peptide system setup is shown in Figure 4.3.

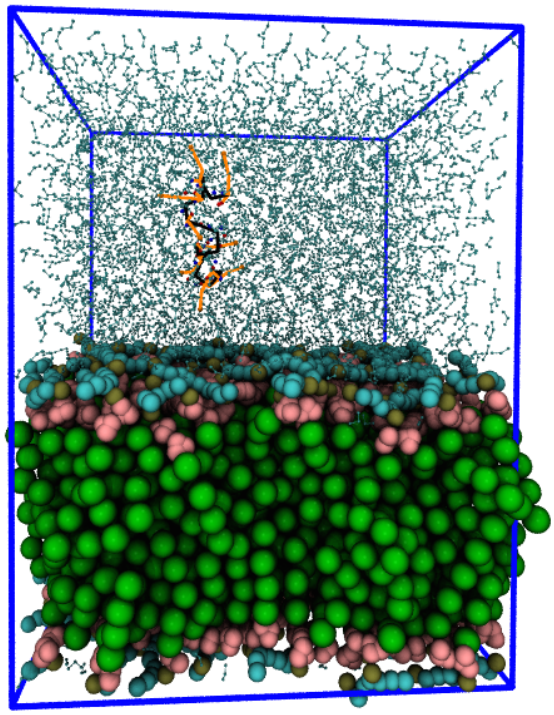

Figure 4.3: Bilayer peptide system setup. Peptide is placed 5 nm away from the bilayer.

Atomistic POPS and POPC bilayer simulations are performed with GROMOS 53A6 lipid force field [175]. The thermostat coupling method, velocity rescaling with a stochastic term (v-rescale), with a time constant of 0.1 ps is used to maintain a

temperature of 300K. The Parinello-Rahman barostat with a time constant of 5.0 ps and isothermal compressibility $1.08\times10^{-5}(kcal\cdot mol^{-1}\cdot nm^{-3})^{-1}$ are used to maintain semi-isotropic pressure at 1 bar in the z direction and 1 bar in the x, y plane. The time step for dynamics is 2 fs and the neighbor list is updated every 5 steps. Long-range electrostatic interactions with periodic boundary conditions (in x, y, z directions) are evaluated using the PME method.

4.3.5 Analysis Methods

4.3.5.1 Calculation of Standard Errors

The estimation of the standard error for the average of the property X, is calculated by block average. Namely, the whole trajectory is divided into N blocks, each with M frames. The average of X for each block, and standard deviation from block averages is calculated. The standard error is the standard deviation over $\sqrt{N}$. To ensure the property X is independent in each M-sized block, we calculate the normalized time correlation function of the fluctuations for X.

$$C(t) = \frac{\langle \delta X(0)\delta X(t)\rangle}{\langle \delta X(0)\delta X(0)\rangle} = \frac{\langle \delta X(0)\delta X(t)\rangle}{\delta X^2} \tag{4.2}$$

where $\delta X(t) = X(t) - \langle X\rangle$, and $\langle \delta X^2\rangle$ is the mean squared fluctuation. The size M is set to equal twice the correlation time $\tau_X = \int_0^\infty C(t)dt$. The standard error in X can also be directly obtained from:

$$se[X] = \sqrt{\frac{2\tau_X}{T_{run}}} < \delta X^2 >^{1/2} \tag{4.3}$$

All standard error calculated in this paper use the block average method.

4.3.5.2 Density Distribution

In the CG bilayer system, the density distribution for each bead in the lipid is plotted along the bilayer normal direction. In atomistic simulations, instead of using the position of each atom, center of mass of several atoms corresponding to each CG bead is evaluated for better and more direct comparison to CG data. The scheme for atoms mapped to beads is shown in Figure 4.1a.

4.3.5.3 Susceptibility Profile

The bilayer is divided into several slabs of 5Å, in the axial direction, starting from the center of mass of the bilayer. Then the susceptibility or specific dielectric constant of each slab in a direction parallel to the membrane interface is calculated using the following equation based on linear response theory [176],

$$\chi_{//}\epsilon_0 = \beta \frac{\langle |\Delta \mathbf{M}_{//}|^2 \rangle}{\langle V \rangle} = \beta \langle |\Delta \mathbf{P}_{//}|^2 \rangle \langle V \rangle \tag{4.4}$$

where $\mathbf{M}_{//}$ and $\mathbf{P}_{//}$ are the total dipole moment and polarization density in the direction parallel to the bilayer, and the Δ indicates the difference between the value in each sample and the time-averaged one. ϵ_0 is the dielectric constant of vacuum, V is the slab volume and $\beta = 1/k_B T$. Ergodicity is assumed for time averages in the equation. To investigate the effect of polarization on bilayer dielectric profile, only polarizable beads, including serine, ester groups and water molecules in CG

simulation, and their corresponding atom groups in atomistic simulation are taken into consideration. The dipole moment of the polarizable CG beads is assigned to their central main site and the dipole moment of atom group is assigned to their center of mass.

4.3.5.4 Line Tension

Line tension of POPC and POPS bilayer is computed from a ribbon structure in the z direction. Initial and final conformations are shown in Figure 4.4. Ribbon structure is simulated using a $NP_{xy}L_zT$ ensemble and evaluated using Eq.(4.5) [177].

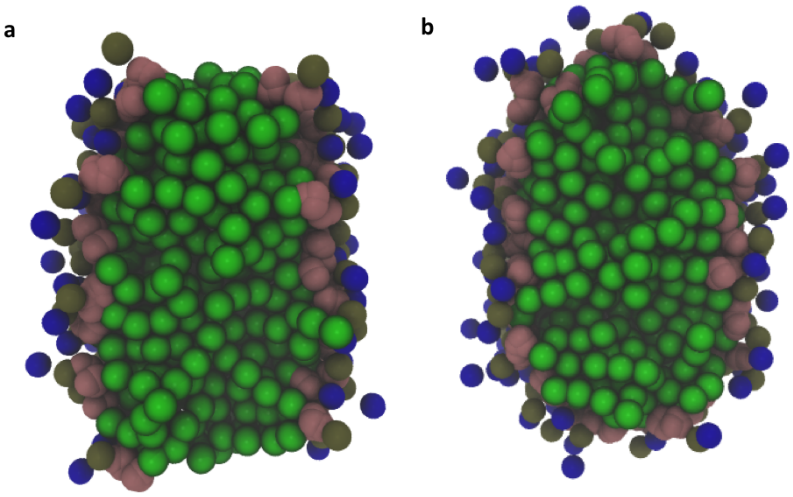

Figure 4.4: Line tension ribbon structure. Phosphates are represented in brown, ester groups in pink, choline groups in blue, alkyl groups in green.

$$\Lambda = \frac{1}{2}\left\langle L_x L_y \left[\frac{P_{xx} + P_{yy}}{2} - P_{zz} \right] \right\rangle \tag{4.5}$$

L_x, L_y are the sizes of the simulation box in x and y axis, and P_{xx}, P_{yy} and P_{zz} are the diagonal elements of pressure tensors along x, y, z axis.

4.3.5.5 Bilayer Potential

Electrostatic potential of the bilayer across the box is calculated using the `g_potential` program in the GROMACS 4.5 package [178]. It is computed by evaluating the double integral of the charge density ($\rho(z)$):

$$\psi(z) = -\frac{1}{\epsilon_0}\int_{-\infty}^{z} dz' \int_{-\infty}^{z'} \rho(z'')dz'' - \frac{z}{\epsilon_0 L}\int_{0}^{L} \rho(z')z'dz' \tag{4.6}$$

where ψ is the electrostatic potential and ϵ_0 is the dielectric constant of vacuum. L is the length of simulation box in the bilayer normal direction. Periodic boundary condition is assumed in the second term, *i.e.* $\psi(0) = \psi(\mathrm{L})$.

4.3.5.6 Cluster Analysis

To characterize the clustering of head groups in lipid bilayers, a distance-based clustering method is adopted. For the pCG model, neighboring lipids that have dummy particles with opposite charges residing within a cutoff distance are considered connected, and all lipids that are connected through dipolar connections are classified as a cluster. Dipolar connections are defined based on contact distance between a positively charged and a negatively charged dummy particle in close contact with each other. The cutoff distance used to determine a dipolar connection is based on pairwise radial distribution functions (RDF) between lipid beads with opposite dummy charges, as shown in Figure 4.5a and Figure 4.5b. The position of the RDF first peak, from positively charged CNO dummy beads to all negatively charged particles (CNM, PO4, G1M, G2M) is used to define the cutoff distances. These

distances are 3.0Å for CNP-CNM pair (serine-serine), 4.2Å for CNP-PO4 pair (serine-phosphate), 3.5Å for CNP-G1M pair (serine-ester), and 4.5Å for CNP-G2M pair (serine-ester). If either of these distances are satisfied between two lipids, they are considered to be interacting lipids forming a dipolar connection.

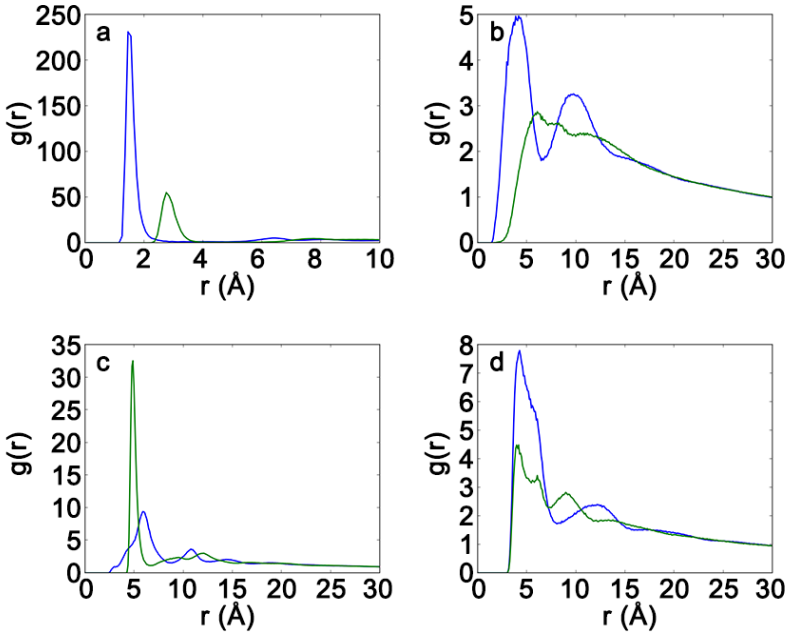

Figure 4.5: Radial distribution functions for serine-involved (a-b) and ion-involved (c-d) electrostatic interaction pairs. (a) CNP-CNM (blue) and CNP-PO4 (green), (b) CNP-G1M (blue) and CNP-G2M (green), (c) ION-CNM (blue) and ION-PO4 (green), (d) ION-G1M (blue) and ION-G2M (green).

The original MARTINI CG model does not have dipolar particles, therefore an additional distance, based on main CG bead sites, are defined to compare pCG and MARTINI model directly. From the defined interacting lipids, pairwise distance cut-offs of 6.1Å for CNO-CNO pair and 5.5Å for CNO-PO4 pair are defined. These are obtained by including the first peak of respective radial distribution functions (results

not shown). Between any two lipids, if both cutoff distances are satisfied, they are considered to be adjacent to each other. An adjacency matrix with $N \times N$ elements, where N is the number of lipids in the system, is introduced to characterize the dipolar connectivity between all lipid pairs, in the following form:

$$\underline{\underline{\mathbf{A}}} = \{a_{ij}\} = \begin{cases} 1 & \text{if } \mathbf{r}_i^{\mathbf{CNO}} - \mathbf{r}_j^{\mathbf{CNO}} \leqslant 6.1\mathring{A} \\ 1 & \text{else if } \mathbf{r}_i^{\mathbf{CNO}} - \mathbf{r}_j^{\mathbf{PO4}} \leqslant 5.5\mathring{A} \\ 0 & \text{otherwise} \end{cases} \tag{4.7}$$

the superscript for the position vector $\mathbf{r}$ denotes the bead type concerned, the subscript is the lipid index, which is a number assigned from 1 to N. With this matrix, the classification of physically neighboring lipid clusters is transformed to a connected-components labeling problem. The `NetworkX` 1.6 module in `Python` 2.7 is used to perform a connected-components labeling analysis and classify connected lipids in the bilayer as clusters [179].

As for atomistic simulations a cutoff distance of 3.5Å between hydrogen and oxygen atoms is used, which is the typical hydrogen bonding distance [180]. The adjacency matrix for the all-atom data is defined below:

$$\underline{\underline{\mathbf{A}}} = \{a_{ij}\} = \begin{cases} 1 & \text{if } min\{\left\|\mathbf{r}_i^{\mathbf{H}} - \mathbf{r}_j^{\mathbf{O}}\right\|\} \leqslant 3.5\mathring{A} \\ 0 & \text{otherwise} \end{cases} \tag{4.8}$$

The superscript for the position vector $\mathbf{r}$ in Eq.4.8 denotes the atom type (H for hydrogen and O for oxygen) and the subscript denotes the lipid index. Whenever there is at least one pairwise distance between oxygen and hydrogen in two different

lipids that is within 3.5$\mathring{A}$, a hydrogen bond is considered formed between the two.

4.3.5.7 Ion Bridge Connectivity

The first peak of the RDFs between a positively charged ion (Na^+) and other negatively charged beads in a lipid is shown in Figure 4.5c and Figure 4.5d, and is used to define cutoffs for ion-bead interactions (CNM: 4.4Å, PO4: 6.1Å and G1M/G2M: 5.1Å). In other words, an ion is bound to a lipid if the distance between the positively charged ion and the negatively charged lipid particle is less than the cutoff distance. An ion bridge is formed when one lipid connects to another lipid via an ion-lipid connection.

4.4 Results and Discussion

4.4.1 Structural and Dynamic Membrane Properties

Bilayer Self-Assembly: Snapshots of the bilayer self-assembly process are shown in Figure 4.6 for POPS, and Figure 4.7 for POPC. In both systems, the lipids begin aggregating in less than one nanosecond and form a single disordered aggregate. As system evolves, the aggregate rearranges to form a defect-free bilayer in less than 12 ns.

Area per Lipid and Bilayer Thickness:The bilayer area per lipid at different NaCl concentrations is shown in Figure 4.8. The area per lipid of POPS and POPC at 0M ion concentrations (i.e. with counter ions) is 65Å^2, for both systems with MARTINI force field [1], and 62Å^2 and 60Å^2 respectively with our polarizable model.

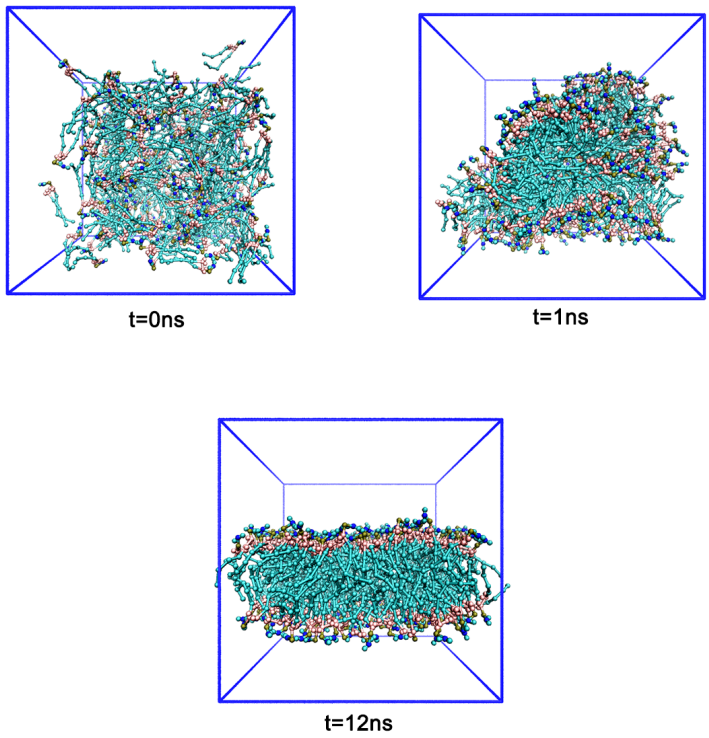

Figure 4.6: Time evolution of bilayer self assembly using pCG (polarizable coarse-grained) POPS. Phosphates are represented in brown, ester groups in pink, serine groups in blue, other groups in cyan.

The standard errors, determined from block averages, are within 10^{-3}nm^2 for all the four systems. One major distinction in our results compared to the MARTINI force field is the ability of our model to capture a difference between the area per lipid of POPC and POPS. Due to the absence of any dipolar interactions, the area per lipid values of POPC and POPS bilayer are nearly identical in MARTINI. A condensation effect is observed in pCG POPS bilayer induced by strong dipolar interactions between the serine head groups. In experiment, the area per lipid of POPS has been reported by different groups to be 45-55Å^2 [181, 182] whereas for POPC it is around 62-68Å^2

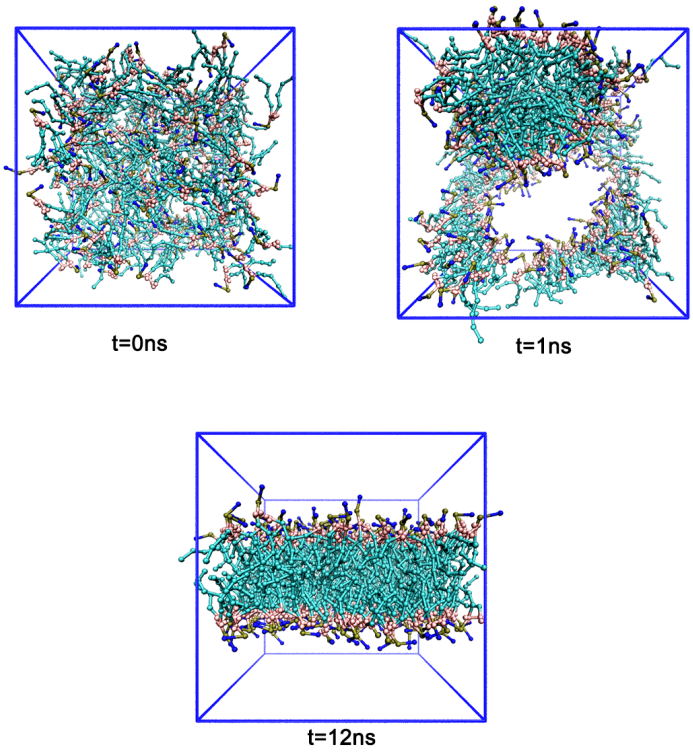

Figure 4.7: Time evolution of bilayer self assembly using pCG POPC. Phosphate beads are represented in brown, ester groups in pink, choline groups are in blue, other groups in POPC in cyan.

[183–186]. Even though our POPC area per lipid (62Å^2) is about 3Å^2 lower than that of MARTINI POPC (65Å^2), both coarse grained values are within reasonable range, in comparison to both experiments and all-atom simulations [187].

In both MARTINI and our pCG model, the decrease in area per lipid induced by the addition of 1M NaCl is in agreement with previous all-atom simulations [152], and experimental measurements [188] using various lipid bilayers. All-atom study by Pandit et al. characterizing the effect of NaCl on DPPC bilayers, showed that the area per lipid of the bilayer decreases with the presence of ions [156]. The reduction in

area per lipid is due to a condensation effect induced by Na^+ ions. On the other hand, Tieleman's study on atomistic POPS with GROMOS, in the presence of ions does not show a marked effect on area per lipid [158]. Our model, along with MARTINI shows a 3-4% decrease in area per lipid with the presence of monovalent ions, in both POPC and POPS systems.

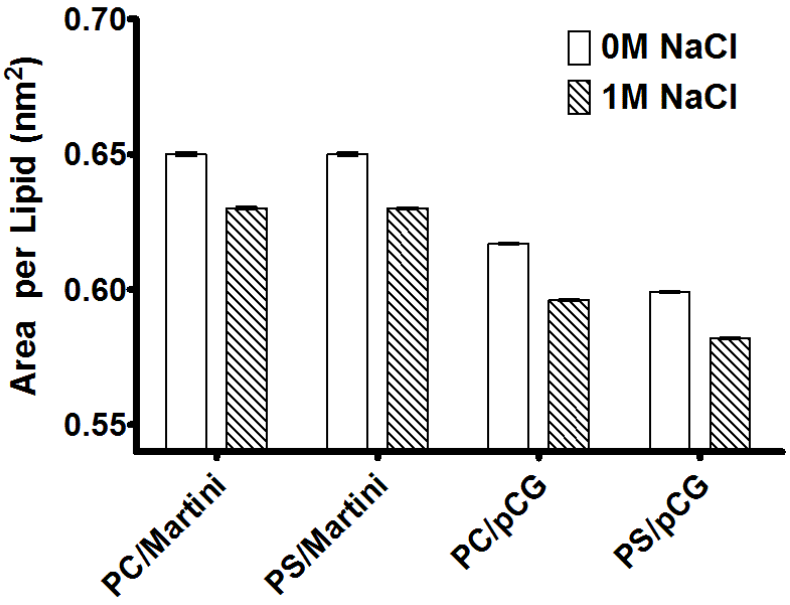

Figure 4.8: Area per lipid change induced by the addition of 1M NaCl. The standard error of mean is within 10^{-3}nm^2.

The average bilayer thickness is listed in Table 4.3. Bilayer thickness is measured as the distance between vertical positions (z-axis) of phosphate groups on either leaflet. The bilayer thickness of pCG POPS is smaller than that of pCG POPC by ~0.5Å. In all-atom and experimental studies, the bilayer thickness of POPS is reported to be 38.2 Å and for POPC it is 39.1 Å [154,183], which shows the same trend. In addition, with the presence of ions, all-atom simulation data with POPC, and POPC-POPS

mixed systems, show an increase in bilayer thickness, which is in agreement with our bilayer thickness increase of 0.7Å [188, 189]. The change in bilayer thickness is attributed to an increase in head group interaction with ions and the decrease of area per lipid.

Table 4.3: Bilayer thickness in different systems evaluated over last 100 ns data

System	Bilayer thickness (Å)	Standard error
POPC (MARTINI)	42.7	0.04
POPC + 1M NaCl (MARTINI)	43.7	0.03
POPS (MARTINI)	41.6	0.04
POPS + 1M NaCl (MARTINI)	43.1	0.03
POPC (pCG)	44.2	0.03
POPC + 1M NaCl (pCG)	44.9	0.03
POPS (pCG)	43.7	0.03
POPS + 1M NaCl (pCG)	44.4	0.03

Density Distribution: Density distributions (see Figure 4.9) of different head groups of POPC and POPS were evaluated to estimate the effect of added dipolar particles. As shown in Figure 4.9b and Figure 4.9d, the regions occupied by phosphate (PO4) and serine groups (CNO) in POPS overlap in space for our model and all-atom

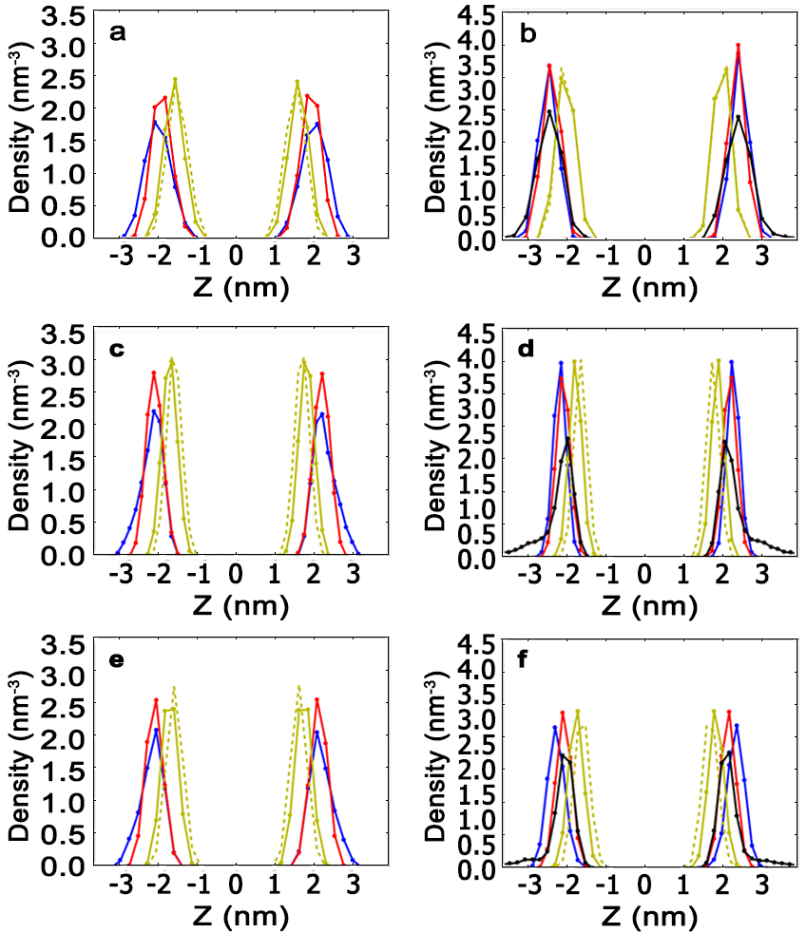

Figure 4.9: Density distribution of (a) POPC from all-atom data, (b) POPS from all-atom data, (c) POPC from pCG data, (d) POPS from pCG data, (e) POPC from MARTINI data, (f) POPS from MARTINI data. Solid yellow: GL1; dashed yellow: GL2; red: PO4; blue: NC3/CNO; black: Na^+.

data. This effect is primarily due to the electrostatic interactions among the serine and phosphate groups, between lipids and within lipids, that causes the phosphates to lie in the same vertical position (z-axis) as the serine groups. That is, with the addition of head group dipoles, both the phosphate and serine groups lie on the same plane. However, with the MARTINI force field the serine head group bead is located

above the phosphate bead, as seen by the outward shift of the PO4 and CNO distribution peaks (Figure 4.9f). This is due to a lack of any dipole-dipole or electrostatic interactions between CNO-CNO beads and CNO-PO4 beads in MARTINI leading to an increase in conformational freedom of CNO-PO4 beads.

For the 1M NaCl system, both pCG POPS and pCG POPC exhibit Na^+ ion penetration as observed by the increase of the Na^+ density distribution near the head group region (black curve in Figure 4.10a and Figure 4.10b). There is a clear distinction between pCG POPC and pCG POPS, a deeper ion penetration in the PS system is observed. Due to this effect, some of the charges on phosphate beads are satisfied, and the serine bead is seen to interact less with the phosphate group, and more with ions and water. This can be better understood by comparing serine and phosphate positions in Figure 4.10b and Figure 4.9d. By the addition of NaCl the CNO peak shifts outwards, towards the solvent. The ion density curves with both our model and MARTINI (black curve in Figure 4.10a and Figure 4.10b) is similar in location to the Na^+ ion peak with old CHARMM parameters, where Na^+ over binding was observed [190]. In order to estimate if ions exchange with the solvent we looked at ion residency time (τ) using the method outlined by Sachs et al. [155]. The ion residency time of our CG ion (Figure 4.11) is more than an order of magnitude less than that of all-atom ions using GROMOS (Figure 4.12), thus suggesting that our ions are not stuck to the lipid bilayer. However, we would like to point out that the monovalent ion used in this study, both with MARTINI and pCG forcefields, is just a prototype monovalent ion. It is not representative of sodium specifically, thus we can't comment on the possibility of overbinding. We are currently working on

parameterizing ions and charged interactions based on size to charge ratio.

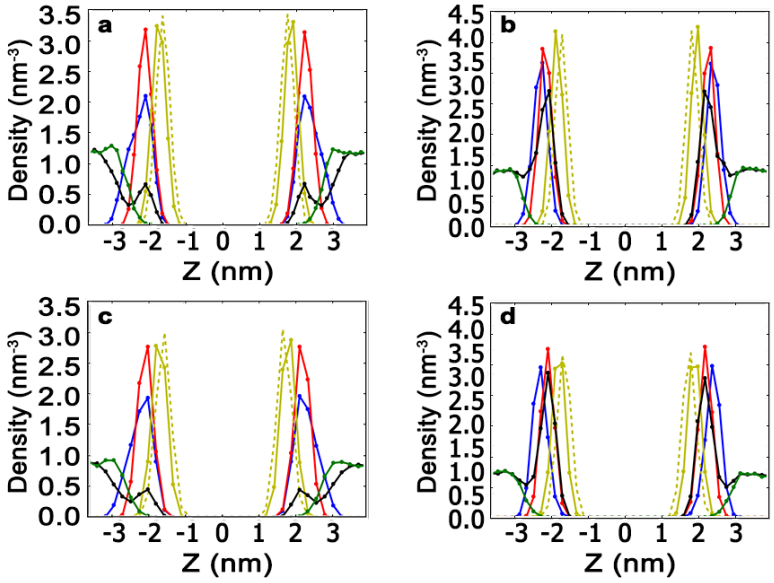

Figure 4.10: Density profiles of lipid bilayer systems with 1M NaCl. Solid brown: GL1; dashed brown: GL2; red: PO4; blue: NC3/CNO; black: Na^+; green: Cl^-. Density distribution of (a) POPC with 1M NaCl from pCG data, (b) POPS from with 1M NaCl from pCG data, (c) POPC with 1M NaCl from MARTINI data, (d) POPS with 1M NaCl from MARTINI data.

Susceptibility Profile and Dielectrical Potential: Susceptibility (χ) is a measure of dipole moment sensitivity to changes in external electric field. Both water molecules and head group beads contribute to this dipole moment, and hence χ. Dielectric susceptibility of a bilayer-water system with atomistic force field GROMOS (red curves), our polarizable CG model (black curves) and the MARTINI force field (gray curves) for POPC and POPS is depicted in Figure 4.13a and 4.13b respectively.

In the case of POPC (Figure 4.13a) there is a gradual gradient in χ from the center

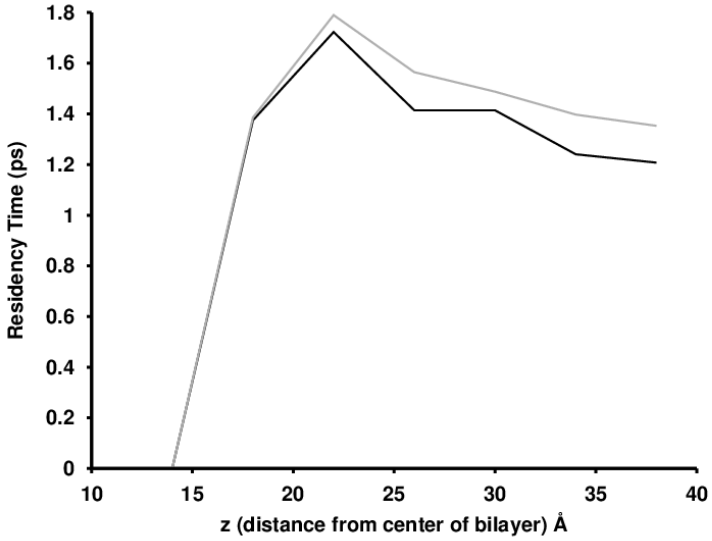

Figure 4.11: Residency time (τ), as a function of distance from the bilayer center for counter ions in pCG POPS system (black curve) and extra added ions (gray curve).

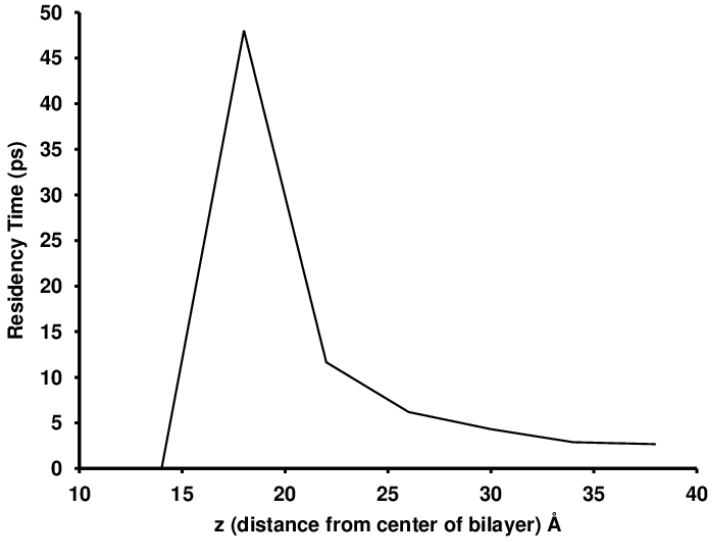

Figure 4.12: Residency time (τ), as a function of distance from the bilayer center for ions in all-atom POPS system.

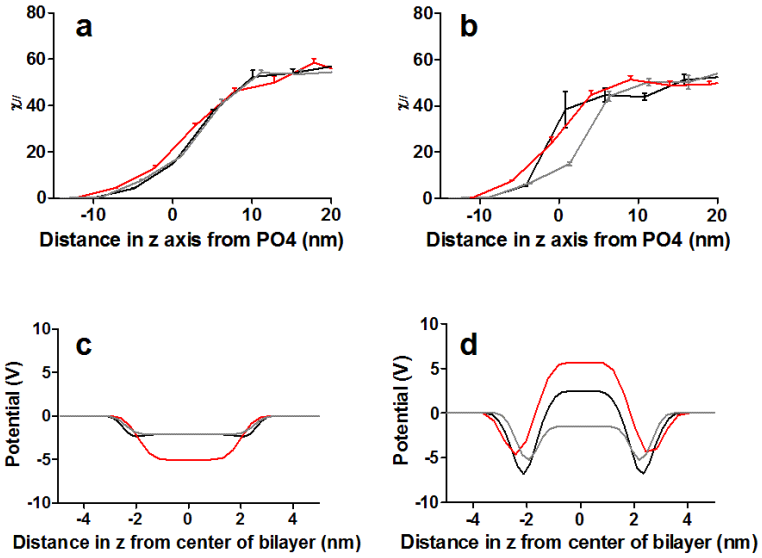

Figure 4.13: Susceptibility profile of (a) POPC and (b) POPS bilayers. Potential profile of (c) POPC and (d) POPS bilayer. Atomistic profile is represented in red, MARTINI in gray and pCG in black.

of the bilayer (x axis <0) to bulk water (x axis >0). This trend is consistent in all three systems. However, in the case of POPS (Figure 4.13b), the regions near the head groups (interfacial region) have a high dielectric contribution in both all atom simulations (red curve) as well as with pCG (black curve). This effect is not captured in MARTINI (gray curve) largely due to the lack of head group bead polarizability. A CARS (Coherent Anti-Stokes Raman scattering) microscopy experiment used by Cheng et al. show that interfacial water molecules near POPS multilamellar vesicle is more polarized than those near POPC multilamellar vesicle [191], which can be interpreted as being consistent with our finding that PS interfacial dipoles are more prone to the change of external electric field .

To investigate the effect of bead polarization on membrane electrostatics, we computed transmembrane electrical dipole potential (V) that arises solely from POPC and POPS lipid bilayers, excluding water molecules and ions. Transmembrane potential for POPC and POPS bilayer systems with atomistic force field GROMOS (red curves), our polarizable CG model (black curves) and the MARTINI force field (gray curves) is depicted in Figure 4.13c and 4.13d respectively. This potential largely arises from the alignment of lipid dipole head groups. For the POPC bilayer, the dipole potential evaluated using pCG and MARTINI is nearly indistinguishable, with the exception of a marginal decrease in potential is observed at the interfacial region with pCG, owing to the presence of polarizable ester groups. This result is in disagreement with the observations from Orsi et al., which found that ester groups of PC membranes play a more significant role in electrostatic potential [192].

In the case of POPS, there is a more significant gradient in dipole potential change from the interfacial region to the hydrocarbon core (see Figure 5d, from x=0 to |x|=2), with pCG and all atom bilayers. Although the absolute value of the dipole potential at the center of the bilayer is around +2.5V with pCG, and +5V with the atomistic model, we are able to capture the right trend. That is, MARTINI yields a negative potential at the center of the bilayer, whereas, pCG and atomistic yield a positive potential.

PS Cluster: The presence of lipid clusters in PS and mixed PC/PS bilayers has been observed in the atomistic simulations [158, 189]. Since the head group of POPS in our model is capable of forming dipole-dipole interactions, dynamic clusters are observed on the membrane surface see Figure 4.14b and Figure 4.2b). That is, there

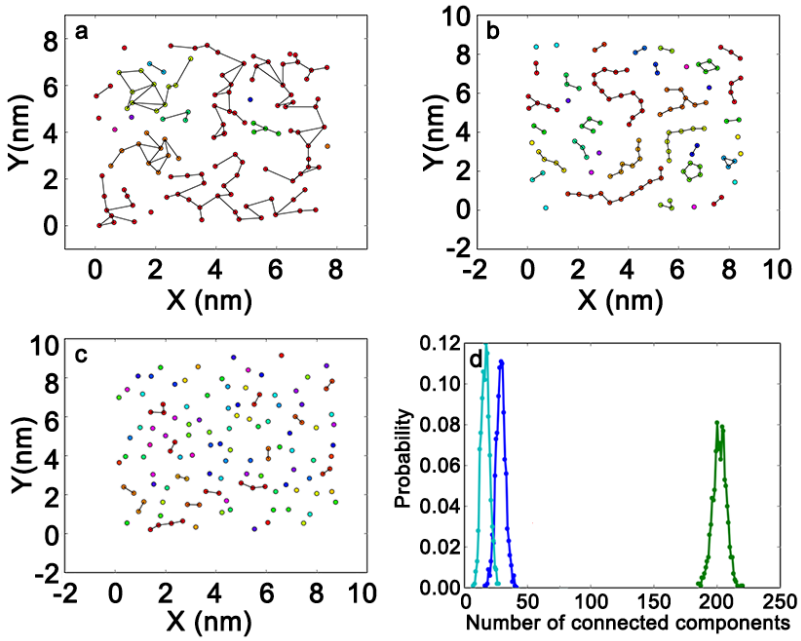

Figure 4.14: Top view of head group clusters for a leaflet (each point represents a phosphate atom, and lines represents lipid connectivity) in (a) all-atom POPS bilayer, (b) pCG POPS bilayer, and (c) MARTINI POPS bilayer. Distinct colors are used to distinguish individual clusters. (d) Probability distribution of number of clusters in POPS bilayer in all-atom (cyan), pCG (blue), and MARTINI (green) systems.

are dipolar interactions connecting oppositely charged dummy particles of neighboring lipids. As shown in Figure 4.14d, on average, there are around 30 clusters in our polarizable lipid CG model, and around 20 clusters in POPS all-atom model. The clusters in our CG model are mostly linear whereas in all-atom simulations they have more branches. This is because, the serine group in the all-atom system can form multiple hydrogen bonds between lipids, while the serine CG bead can only form two dipolar connections. All clusters observed in the simulations are dynamic in nature,

they emerge and disappear. Therefore, these dipolar interactions observed in our CG model mimic the hydrogen bonding network observed in all atom bilayers [193] (Figure 4.14a). These clusters are not present in the MARTINI POPS system (Figure 4.14d), due to the inability of the model to capture dipolar interactions. Clearly, pCG is capable of reproducing the essence of cluster formation, which is a distinct property of POPS lipids. The dipoles in polar beads, act as pseudo hydrogen bonds and assist in the interactions between head groups. These head group interactions lead to the formation of clusters.

Line tension: Our model predicts a line tension of 37.3±4 pN for POPC bilayer. This value is within the range of that predicted for similar lipids like DOPC and SOPC (6∼25pN) [177, 194, 195]. Thus the model can capture the right barrier in pore formation of POPC bilayers, and the presence of dipolar particles does not significantly increase this energetic penalty or the barrier for pore formation. The line tension for pCG POPS is 37.3±4 pN.

Ion Bridges: To better characterize ion bound lipids, we classified lipids bound to ions via ion bridges, where an ion bridge is defined as an ion connecting two lipid molecules based on cut-off distances (see methods section). For the POPS bilayer system with 0M NaCl (i.e. with counter ions), 20% of lipids are bound to only one ion bridge, 49% to two ion bridges, 28% to three ion bridges and almost none of the lipids are bound to four ion bridges (Figure 4.15). However, when 1M NaCl is added to the system, the number of 3 and 4 ion bridges bound to a lipid increases significantly to, 43% and 15% respectively. This suggests that the addition of extra ions to the system connects more lipids, forming larger ion-mediated lipid regions.

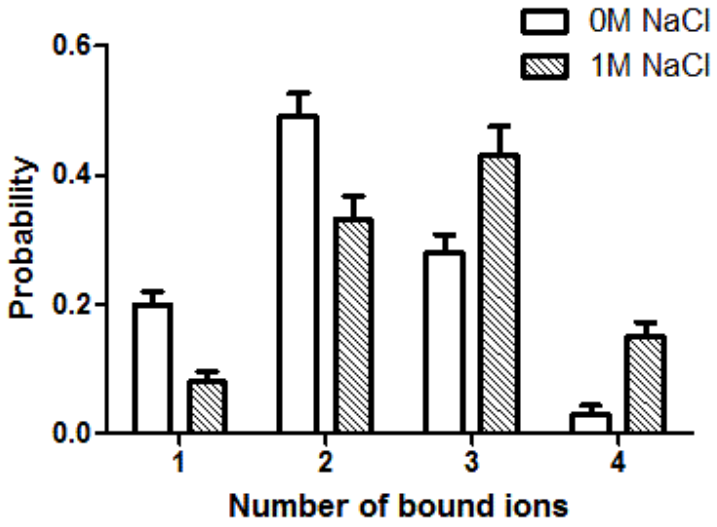

Figure 4.15: Probability of 1, 2, 3 and 4 ion bridges bound to a POPS lipid at different ion concentrations.

This result is consistent with many all-atom studies on anionic bilayers [152,158,188].

Interactions between Ion and Head Groups: We further investigated interactions between ion and lipid head groups, to better characterize subtle changes in bilayer properties. Figure 4.16a shows a representative structure of a POPS lipid bound to Na^+. In this image, the Na^+ ion is seen interacting with PO4, CNO (negatively charged dummy CNM) bead and G1M dummy bead. Sodium ions occupy the region between serine, phosphates and the ester groups, maximizing interaction with all three charged regions. This can also be seen from density plots (Figure 4d and S7b), where the sodium ions (black curve) occupy a region between CNO (blue curve) and PO4 (red curve), which lie on the same z plane, and ester groups (brown curves). A consequence of this is a tilt in ester group vector (defined as GL1-G1M), where the negatively charged dummy, rises from the plane to interact with the sodium ion.

To further quantify this effect, the angle between the ester group and its negatively charged dummy (GL1-G1M) vector with the POPS bilayer normal is measured.

In Figure 4.16b, the angle distribution shows two distinct peaks, accounting for the angle made by ester groups near a sodium ion, which is better aligned to the bilayer normal (peak at 75°); and another, away, which is less aligned (peak at 125°). For the 1M NaCl system, the GL1-G1M vector is better aligned to the bilayer normal, compared to the system with 0M NaCl. The better alignment of the GL1-G1M vector with the bilayer normal at 1M NaCl can be rationalized by the increase in population of ion bound lipids. Figure 4.16c shows a representative structure of a POPC lipid bound to Na^+. In this image, the ion (Na^+) bound to a lipid is more exposed, due to favorable interactions with phosphates. The angle between PO4-NC3 (head groups) and the bilayer normal is depicted in Figure 4.16d. The PO4-NC3 vector is better aligned with the bilayer normal with 0M NaCl (peak at 75°). However, for 1M NaCl, this angle shifts (peak at 100°), indicating a possible in-plane alignment of PO4-NC3 vector, as seen in Figure 4.16d. This is potentially one of the reasons on why there is lesser ion penetration in POPC membranes. A study by Woolf et al. shows a similar head group tilt observed in all-atom MD simulations of POPC with 1M NaCl [155].

4.4.2 Membrane-Induced SVS-1 Folding

The presence of dipole particles in lipids (POPS) and peptide (SVS-1) enabled us to better investigate the role of electrostatic interactions. Figure 4.18 includes 4 snapshots of one representative run of SVS-1 peptide with pCG POPS bilayer. Within

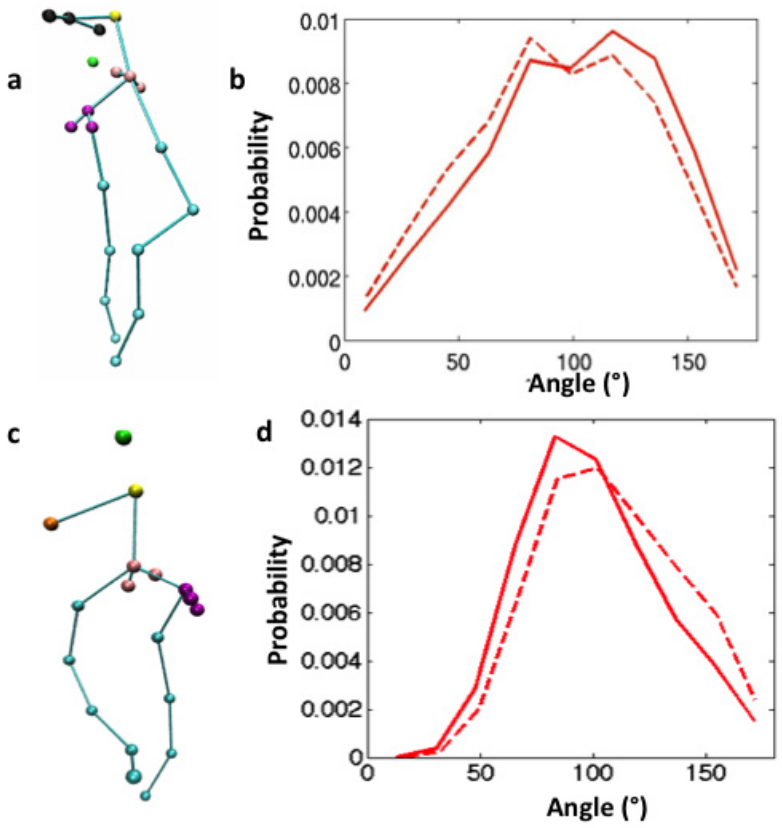

Figure 4.16: (a) Representative structure of POPS lipid bound to Na^+ . Colors: Na^+ (green), CNO (black), PO4 (brown), GL1(pink), GL2(violet), alkyl (cyan) (b) Probability distribution of the angle made by the GL1-G1M vector of POPS with the bilayer normal in POPS (red). Dashed lines represent the systems with 1M NaCl and solid lines for 0M NaCl. (c) Representative structure of POPC lipid bound to Na^+. Colors: Na^+ (green), NC3 (brown), PO4 (brown), GL1(pink), GL2(violet), alkyl (cyan). (d) Probability distribution of the angle made by PO4-NC3 vector with bilayer normal in POPC. The dashed lines represent the systems with 1M NaCl and solid lines 0M NaCl

the first 10 ns, lysine side chains of the peptide (brown) are attracted to the anionic bilayer. Once the side chain charges are satisfied, the dipoles of the backbone beads interact with each other, which aid in formation of a β-hairpin within 30 ns in most trials. The peptide is dynamic on the surface of the bilayer and explores different registers.

This is consistent with experimental behavior of SVS-1, which has been shown to preferentially adopt a β-sheet conformation both in the presence of anionic membranes and tumor cells [144, 171]. To characterize the lateral position of the peptide, we looked at z distance between side chain beads of each of the β strand residue, and phosphate layer, with time. Figure 4.17 represents this z distance (scale on the color bar) for one representative trial that folds into a β-hairpin. Initially, the lysine distances from the phosphate layer are lower than the valines (dark blue in Figure 4.17a, <2Å), however, with time the valine distances from the phosphate layer become more negative (green and blue, -4 to -7Å). Negative distances in Figure 4.17 denote deeper penetration beneath the phosphate layer . That is, with time the valines face the hydrophobic phase to interact with the alkyl beads, while the lysines continue to interact with the head group region (PO4 and CNO). This leads to a more negative distance for valines than lysines in Figure 4.17.

Multiple trials were performed to validate the significance of our results. Details of 3 random trials are shown in Figure 4.19. Figure 4.19a-c depicts in-register sheet fraction (Fr_{sheet}) [30], center of mass distance (com) of the peptide from the bilayer (Δz), and end to end distance of the peptide (L_c), respectively. Different colors represent different trials. From Figure 4.19a and 4.19b, as the peptide reaches the bilayer

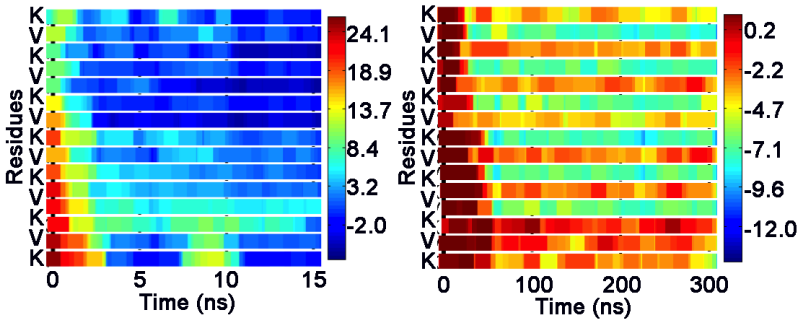

Figure 4.17: Lateral z distance of each side chain bead of SVS-1 strands (residue name on y-axis), from the center of mass of pCG POPS PO4 beads, with time. Color bar represents distance in Å, where negative values indicate deeper side chain penetration, below the com of PO4 layer. (a) and (b) represent different time periods.

(denoted by 20Å on the y axis), the in-register sheet fraction gradually increases, suggesting the involvement of the bilayer in driving peptide folding. It is important to note that the peptide is dynamic on the bilayer, which can be seen by fluctuations in in-register sheet fraction, which is a strict measurement of sheet contacts. In addition to β-hairpin, off-register conformations are observed, as depicted by the representative peptide conformations with in-register sheet fraction between 0-0.2, 0.2-0.4, 0.4-0.6, 0.6-0.8 and 0.8 to 1 in Figure 4.19e, 4.19d, 4.19g, 4.19f and 4.19h respectively. Conformations with Fr_{sheet} >0.5 are largely sheet-like. Time evolution of L_c of the peptide is shown in Figure 4.19c, a decrease in L_c as the peptide reaches the bilayer and adopts a sheet-like conformation is observed. The trend in L_c correlates with the pair fraction (Figure 4.19a). That is, with an increase in Fr_{sheet} there is a decrease in L_c.

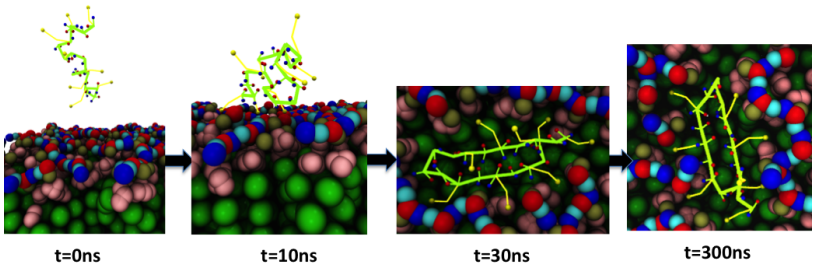

Figure 4.18: Stages in SVS-1 sheet formation: peptide is randomly placed above the bilayer at t=0ns; lysine side chains interact with anionic POPS within a few ns. With lysine side chains buried in the bilayer, the backbone dummies interact to form sheets, which are formed as early as 30 ns in some runs. The peptide is dynamic on the surface of the bilayer and largely retains sheet content by the end of 300 ns. Colors: lipid hydrophobic core(green), peptide backbone(orange), positive and negative dummies in blue and red, phosphates in tan, esters in purple, CNO in cyan and lysines in yellow.

However, not all trials lead to sheet-like conformations (blue curves in Figure 4.19). Details of 6 more trials are outlined in the supplementary material. In total, 5 out of 9 runs folded into stable, sheet-like conformations. The peptide is dynamic and folds and unfolds on the surface of the bilayer. For example, in Figure 4.20e there are 27 transitions from folded (Fr_{sheet} >0.7) to the unfolded state (Fr_{sheet} <0.3) in 300ns.

Figure 4.20a-f depict Δz, and Fr_{sheet} of multiple trials. Even though a small double well dihedral bias for both helical and sheet conformations is added to the force field, no helicity was observed for the SVS-1 peptide with pCG POPS at the interface. This is not surprising as the peptide has a distinct sheet pattern of alternating cationic and hydrophobic residues, along with a designated turn region [196].

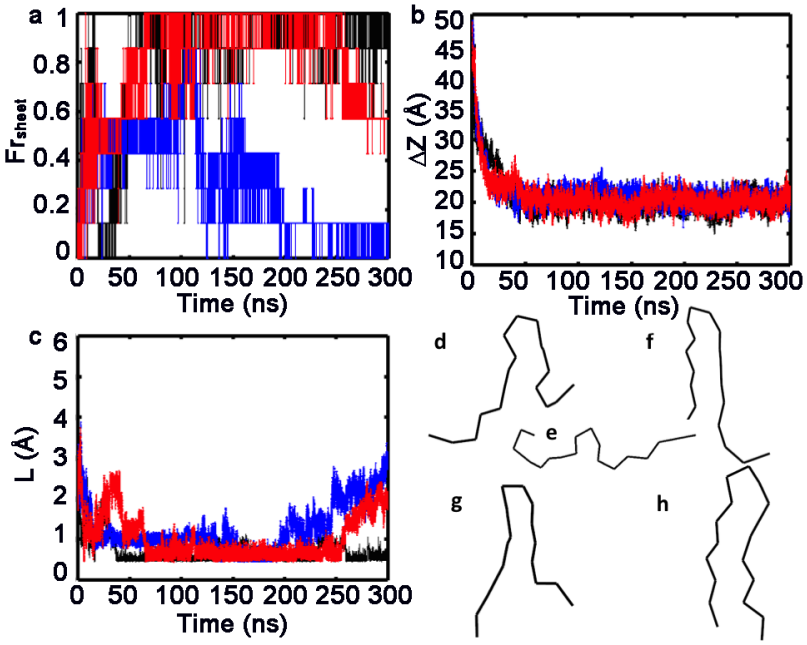

Figure 4.19: Time evolution of (a) sheet pair fraction (Fr_{sheet})of the peptide; (b) center of mass (com) distance of the peptide from the phosphate beads on the bilayer (Δz); (c) end to end distance (L_c) of the peptide, evaluated between the first and the last backbone bead. Each color represents a single run. Representative snapshots of conformations explored, each with a in-register sheet fraction of (d) 0.28, (e) 0.14, (f) 0.71, (g) 0.57 and (h) 1.0. All data from our polarizable coarse-grained models.

As control systems, simulations of (a)pCG SVS-1 and pCG POPC bilayer, (b)pCG SVS-1 and POPS bilayer without polarizable particles (POPSnd *i.e.* POPS no-dipole), and (c)pCG SVS-1 in water were analyzed. Figures 4.21a and 4.21d, 4.21b and 4.21e and 4.21c and 4.21f, depict Fr_{sheet}, Δz, and L_c of runs with pCG SVS-1 and pCG POPC, and pCG SVS-1 and POPSnd (or POPS no dipole), respectively. Each color in the Figures represents an individual trial, a total of 6 distinct runs are represented. Fr_{sheet} explored by these systems is largely below 0.3 and L_c, above

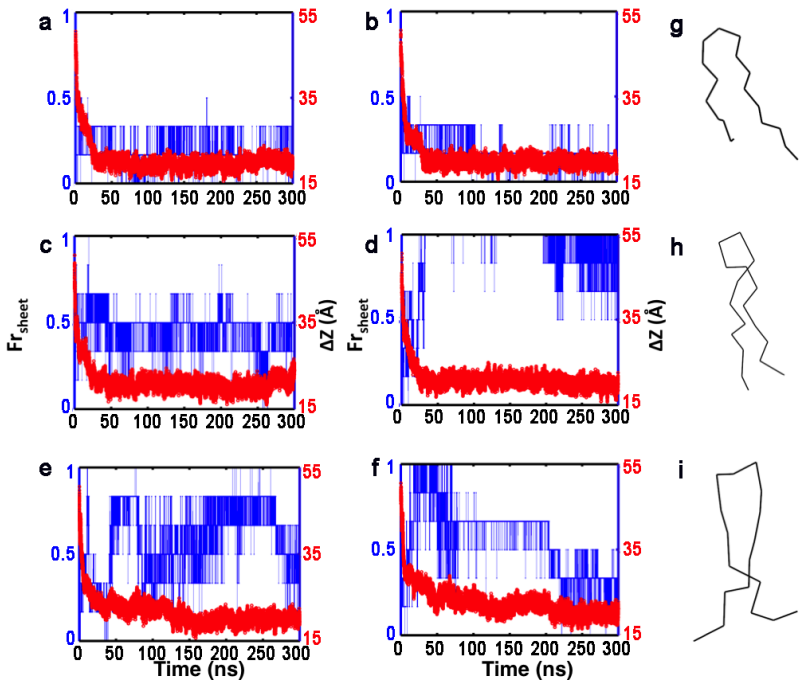

Figure 4.20: Time evolution of sheet pair fraction of the peptide (Fr_{sheet}) in blue and center of mass (com) distance of the peptide from the bilayer in red, for system with pCG POPS. a-f represents individual trials, and g, h and i are final conformations of trials depicted in c, d and e, respectively.

20Å. Therefore, there is a lack of secondary structure content in these systems, and a preference for more extended conformations with L_c ranging from 20 to 50Å (see Figure 4.21c and 4.21f). Any sheet-like conformation explored in the case of pCG POPC (red and magenta lines in Figure 4.21a) are structures explored by the peptide in water. This is supported by the Δz plot (Figure 4.21b), which shows that the distance between the peptide and the com of the bilayer is greater than 35Å untill 30-40 ns. A time-lag in peptide-pCG POPC bilayer binding is observed by comparing the time evolution of Δz in Figures 4.21b, 4.21e, and 4.19b. That is, there is a no-

ticeable time difference of about 10ns between peptide interaction with pCG POPC, in comparison with POPS with and without dipoles. Therefore, the serine dipoles might not play a significant role in attracting the peptide to the bilayer surface.

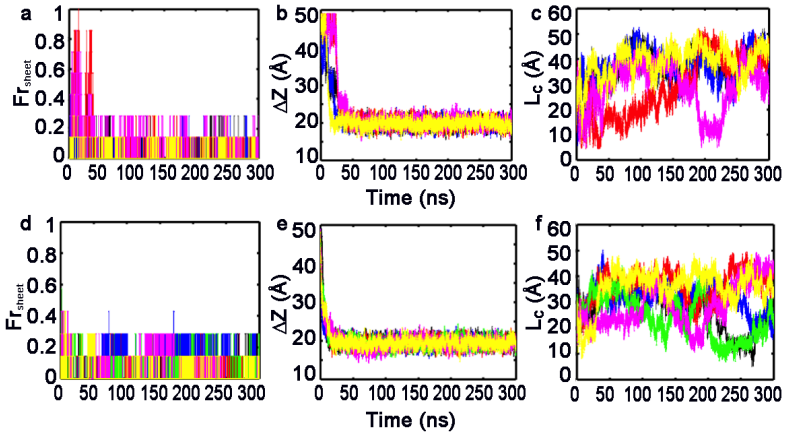

Figure 4.21: Time evolution of (a and d) sheet pair fraction of the peptide (Fr_{sheet}); (b and e) center of mass (com) distance of the peptide from the phosphate beads on the bilayer; (c and f) end to end distance (L_c) of the peptide, evaluated between the first and the last backbone bead. Each color represents a single run. (a), (b) and (c) are data from our polarizable coarse-grained model for POPC bilayer (d), (e) and (f) are data using our peptide model with dipoles and a POPS bilayer without dipole particles (POPSnd).

Time evolution of sheet content, end to end distance, average peptide dihedral, and H1 distance (i to $i+4$ backbone distance) [30] of pCG SVS-1 in water are shown in Figure 4.22a-d respectively. SVS-1 explores unfolded, helical (average dihedral angle of 40-60° and H1 distance of 5-7Å) and sheet-like conformations (sheet contact greater than 0.7 and L_c within 1-2 nm) without exhibiting a preferred structure or

stable state(s) in water. From these four plots, we conclude that SVS-1 is intrinsically disordered in water. This is consistent with both experimental data and the design strategy, *i.e.* SVS-1 was designed to remain disordered and inactive in aqueous solution [144]. In fact, most linear AMPs are not structured in solution, and the induction of secondary structure on membrane surfaces is known to enhance amphipathicity, which plays a key role in the antimicrobial function of these peptides [197]. This also means that the peptide could be collapsed before interacting with the bilayer. However, the fact that a stable β-sheet conformation is observed, only on SVS-1 interaction with pCG POPS and not otherwise, reinforces the role of pCG POPS in stabilizing β-sheet conformations in SVS-1 peptide.

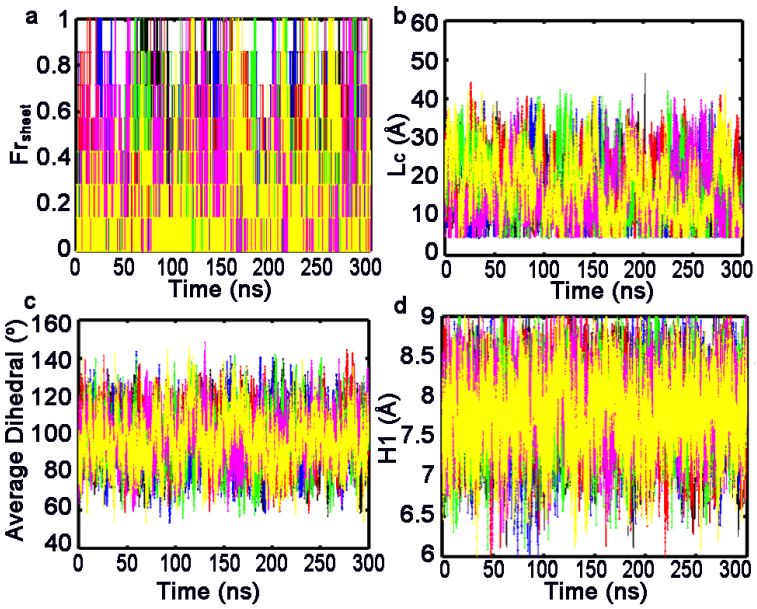

Figure 4.22: Time evolution of (a) sheet fraction (Fr_{sheet}) of the peptide in water, (b) end to end distance (L_c), (c) average dihedral angle per frame and (d) average 1-4 backbone distances (H1). Each color represents a single run.

These results, albeit expected, raise a series of important questions, (a) what drives the folding of pCG SVS-1 on pCG POPS bilayers?, (b) what is the role of dipoles, both in the peptide and the membrane? (c) why does the peptide not fold on pCG POPC and POPSnd (POPS without dipoles) bilayers, and finally, (d) how do the side chains influence the folding process? To answer these questions, we turned to energetic contributions.

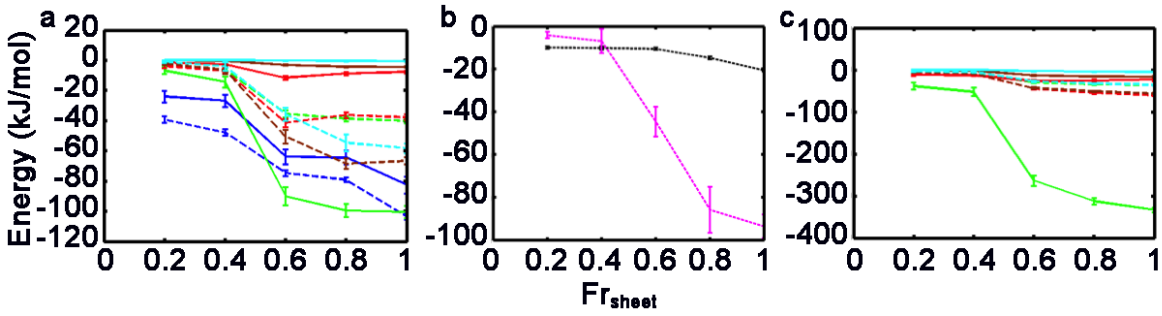

Figure 4.23: LJ pairwise (dashed lines) and Coulombic energies (solid lines) as a function of Fr_{sheet} for (a) PO4-BB (green), CNO-BB(red) and BB-BB (blue), GL2-BB (cyan), GL1-BB (brown); (b) hydrophobic side chain self interaction (black) and hydrophobic side chain-alkyl (magenta); (c) PO4-SC_{C+} (green) and CNO-SC_{C+} (red), GL2-SC_{C+} (cyan), GL1-SC_{C+} (brown). Data from pCG POPS bilayer system.

Figure 4.23a represents distinct energetic contributions between the CNO beads and the peptide backbone beads (BB) (red curves), phosphate-BB (green curves), GL1-BB (brown), GL2-BB (cyan) and between backbone beads themselves (blue curves). All five interactions display a swift decrease in energy from the unfolded state (Fr_{sheet} around 0.2) to the folded state (Fr_{sheet}>0.6), thus denoting a cooperative transition in folding. Figure 4.25 shows an example of a BB-BB dipole interaction

(purple box) and an example of CNO-BB dipole interaction (blue box), where the backbone dipole vectors are represented in brown and the head group dipole vectors in green. Cooperativity in BB interaction is expected and consistent with our previous study [30], however, the interaction of BB with PO4 and CNO beads also display similar trends. This is because, sheet formation in SVS-1 is not just driven by dipolar contacts within the sheet, but also stabilized by interactions between the bilayer head groups and the peptide. This result stresses on the relevance of the "polarity profile" of bilayers, or the gradient in electrical polarity due to chemical heterogeneities at membrane interfaces. It has been speculated by White's group, among others, that the chemical heterogeneities of the interface will provide possibilities for non-covalent, stabilizing interactions with peptides [141, 198]. Both GL1-SC_{C+} (brown) and GL2-SC_{C+} (cyan) interactions seem to be the least significant, with LJ interactions (dashed brown and cyan curves) a little more pronounced than Coulombic interactions. This is largely due to the positioning of the peptide in the bilayer, which is below the PO4 layer as evident from Figure 4.17.

Figure 4.23b represents pairwise energies of valine-valine beads (black dashed curve) and valine-lipid alkyl tails (magenta dashed curve). Both these terms show clear cooperative trends of lower energy for the folded state. However, a sharper transition between the folded and unfolded states is observed in the case of valine-alkyl interactions. To understand the interplay between the lysine (SC_{C+})-phosphate and valine-alkyl interactions, we looked at density distributions of lysine and valine side chains of a representative run (black and blue curves in Figure 4.24, respectively) at different time periods. Density distributions of phosphates on both leaflets (red

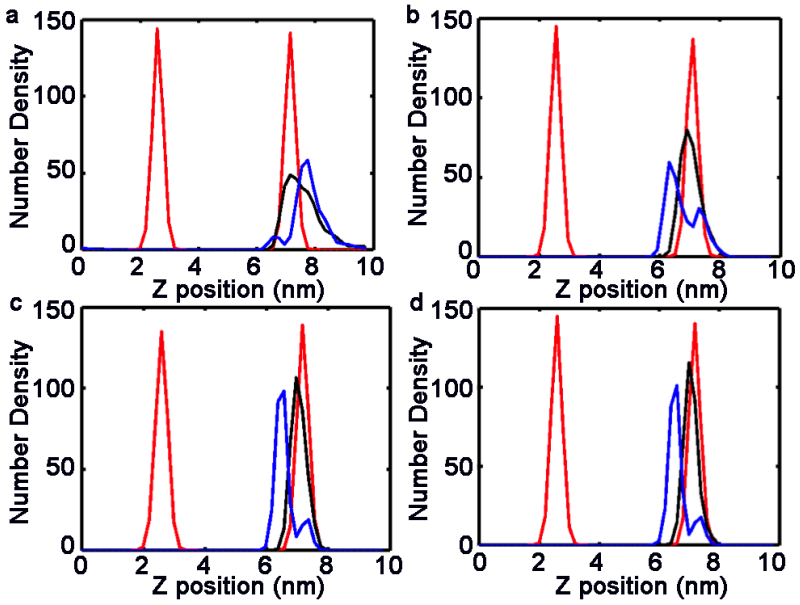

Figure 4.24: Number density distribution of PO4 (red curves), lysine side chain (SC_{C+}) (black curves) and valine side chain beads (blue curves) over a time period of (a) 0-25 ns, (b) 25-50 ns, (c) 50-75 ns and (d) 75-100 ns. Side chain distributions are scaled by a factor of 5 for easy comparison.

curves in Figure 4.24) are shown in red, to denote the bilayer boundaries. Figure 4.24 shows the distribution from (a) 0-25 ns, (b) 25-50 ns, (c) 50-75 ns and (d) 75-100 ns. As can be seen from these plots, lysine insertion into the phosphate region is the first crucial step (black curve in Figure 4.24a). With time, the valine side chains flip towards the interior of the bilayer. By 75 ns, almost all the valine side chain beads are completely buried in the hydrophobic region (Figure 4.24c). Another trajectory is represented in Figure S13, which also shows similar trends in lysine and valine side chain insertion, *i.e.* by 75ns, the hydrophobic side chains are buried in the membrane. These results reinforce the importance of amphilicity in membrane-induced folding of

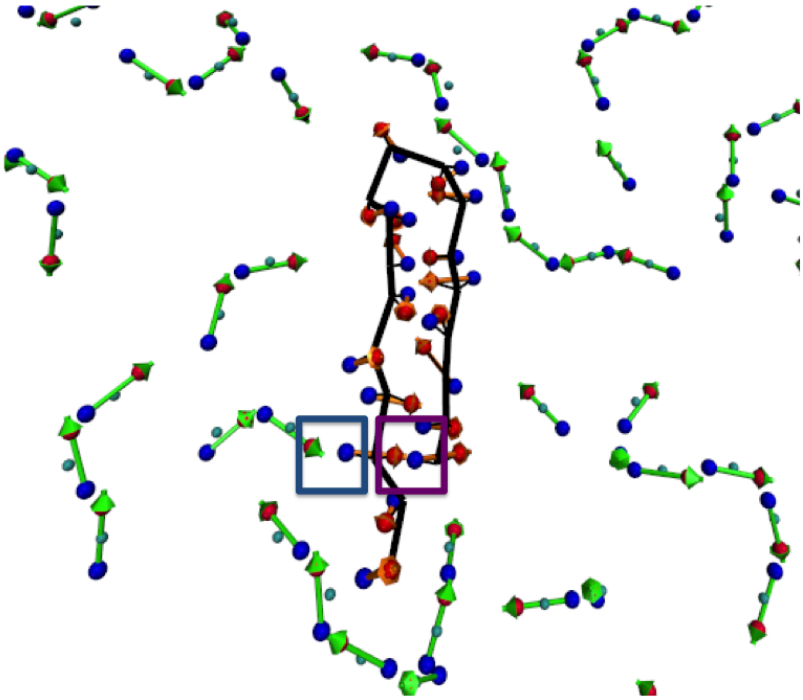

Figure 4.25: Top view of a representative conformation of folded SVS-1 on POPS membrane. Peptide backbone is depicted in black, red and blue represent negatively and positively charged dummy beads. Brown vectors represent backbone dipoles and green vectors, CNO dipoles. Purple box denotes an example of dipolar connections or contacts within a peptide, that play a role in secondary structure content. Blue box denotes an example of peptide-membrane dipolar connections formed between backbone and CNO dummies.

AMPs.

Figure 4.23c represents distinct energetic contributions between the bilayer and charged lysine side chain beads (SC_{C+}), along the reaction co-ordinate Fr_{sheet}. Green curves correspond to interaction between phosphate beads and SC_{C+}, red curves correspond to interaction between CNO beads and SC_{C+}, brown curves correspond to

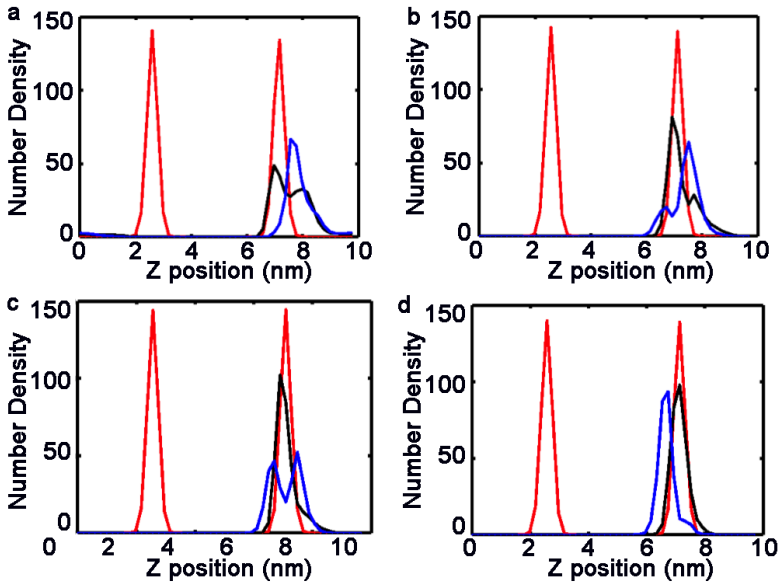

Figure 4.26: Number density distribution of PO4 (red curves), lysine side chain (SC_{C+}) (black curves) and valine side chain beads (blue curves) for POPS system, over a time period of (a) 0-25 ns, (b) 25-50 ns, (c) 50-75 ns and (d) 75-100 ns. Side chain distributions are scaled by a factor of 5 for easy comparison.

interaction between GL1 beads and SC_{C+} and cyan curves correspond to interaction between GL2 beads and SC_{C+}. All solid lines are Coulombic contributions and dashed lines, LJ interactions. Phosphate-SC_{C+} Coulombic interaction (green solid curve) displays a sharp transition from the unfolded state (Fr_{sheet} around 0.2) to the folded state (Fr_{sheet}>0.6). A similar transition of much lower magnitude is observed in the case of CNO-SC_{C+} interaction. Again, both GL1-SC_{C+} (brown) and GL2-SC_{C+} (cyan) interactions seem to be the least significant, with LJ interactions (dashed brown and cyan curves) a little more pronounced than Coulombic interactions, due to the location of the peptide. Thus, phosphates play a larger role in interaction with

cationic side chains. This result can be reconciled with Figure 4.18, where the lysines are seen to drive the peptide towards the bilayer. Positioning of lysine residues to interact with lipid phosphates is a property of many cationic AMPs like CM15, a lysine enriched cecropin-melittin hybrid [199].

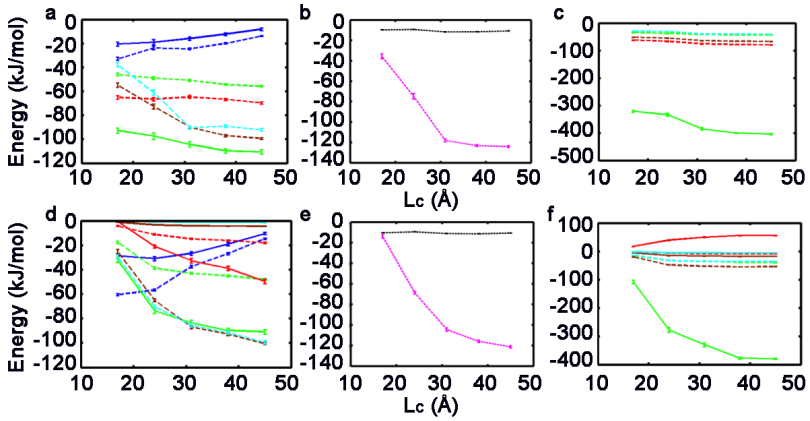

Figure 4.27: LJ pairwise (dashed lines) and Coulombic energies (solid lines) as a function of L_c for (a and d) PO4-BB (green), CNO-BB(red) and BB-BB (blue), GL2-BB (cyan), GL1-BB (brown); (b and e) hydrophobic side chain self interaction (black) and hydrophobic side chain-alkyl (magenta); (c and f) PO4-SC_{C+} (green) and CNO-SC_{C+} (red), GL2-SC_{C+} (cyan), GL1-SC_{C+} (brown). Data for POPS bilayer without dipole particles represented on top (a, b, and c), and pCG POPC bilayer-SVS-1 system below (d, e and f).

SVS-1 does not fold with pCG POPC and POPSnd bilayers, energetic contributions with respect to L_c, of one representative trajectory (brown curves) is depicted in Figure 4.27. Figures 4.27a-c correspond to POPSnd and Figure 4.27d-f to pCG POPC. Figure 4.27a and 4.27d represent energetic contributions between the head group beads (CNO for POPSnd and NC3 for POPC) and the peptide backbone beads

(BB) (red curves), phosphate-BB (green curves), GL1-BB (brown), GL2-BB(cyan) and between backbone beads themselves (blue curves); Figure 4.27b and 4.27e represent pairwise energies of valine-valine beads (black dashed curve) and valine-lipid alkyl tails (magenta dashed curve); and Figure 4.27c and 4.27f, energetic contributions between CNO/NC3 beads and the lysine side chain beads (SC_{C+}) (red curves), phosphate-SC_{C+}(green curves), GL1-SC_{C+} (brown), and GL2-SC_{C+} (cyan). Comparing Figure 4.27 with Figure 4.23, the trend of every curve in Figure 4.23 is reversed in Figure 4.27, except for the blue curves or BB-BB pair interaction. That is, every evaluated pairwise interaction between the peptide and the bilayer in Figure 4.27 favors the unfolded state (L_c>40Å), whereas the same interaction pairs in Figure 4.23, favor the folded state (Fr_{sheet}>0.6). The decrease in BB-BB interaction energy (blue curves) with decrease in L_c is an obvious and expected trend; lower the end-to-end distance, more compact the peptide, higher the intra-peptide interaction and lower the energies.

On comparing Figures 4.27a and 4.27d with Figure 4.23a, we can see that PO4-BB (green curves) interaction energy is lowest in the POPSnd system. This is due to a lack of serine dipoles in the head group region, as dipoles might electrostatically compete with PO4. We can also see that NC3 interacts more strongly with BB beads (red curves in Figure 4.27d), in comparison to CNO in pCG POPS and POPSnd (red curves in Figure 4.23a and Figure 4.27a, respectively), due to its point charge of +1. Therefore, backbone beads interact more strongly with (a)POPSnd, due to the lack of an electrostatic gradient in the head group region, and hence increased PO4-BB interaction, and (b)pCG POPC, due to higher NC3-BB interaction, along

with PO4-BB interaction. Both PO4-BB and NC3/CNO-BB energies in Figure 4.27a and 4.27d (red and green curves), are the lowest for extended peptide conformations on the bilayer surface (L_c>40$\mathring{A}$). This could be because, in both these systems, the dipole or electrostatic interactions within POPSnd bilayer and within pCG POPC bilayer are lower than within pCG POPS. In the case of pCG POPS, the added dipoles facilitate stronger lipid-lipid interactions, which leads to cluster formation (see Figure 4.14). Therefore, in pCG POPS systems, a balance between intra-peptide backbone interaction and peptide backbone-bilayer interaction is achieved. On the other hand, in both pCG POPS and POPSnd systems, the peptide backbone-bilayer interaction is higher, leading to decreased intra-peptide interactions. This suggests that there is a subtle balance between these two competing interactions (intra-peptide and peptide-lipid), which a model must be able to capture, in order to be used to study membrane-induced peptide folding.

From Figure 4.27b, 4.27e and 4.23b, we see that the valine-valine pairwise energies (black dashed curve) are lowest for folded conformations in the pCG POPS system (by -15kJ/mol in Figure 4.23b). However, the valine-alkyl energies (magenta dashed lines) are lower in the case of pCG-POPC (Figure 4.27b) and POPSnd (Figure 4.27b) by about the same amount of -15kJ/mol. Therefore, the net hydrophobic interaction of SVS-1 (intra-peptide and peptide-alkyl tail) does not bias the folded sheet-like state or the unfolded-extended state.

There are two main distinctions between Figures 4.27c, 4.27f and 4.23c. First, the interaction energy between lysine side chains and phosphate beads (green curves) is lowest (around -410kJ/mol) in the POPSnd system (Figures 4.27c), which could

be attributed to an absence of electrostatic gradient in the head group region. It is also worthwhile to note that the lowest energy is when the peptide is extended (L_c>40Å). Second, the electrostatic repulsive energy between lysine side chains and choline (NC3) beads of pCG POPC (red curve in Figure 4.27f) destabilizes the membrane-bound state (+80kJ/mol). This repulsion between the head groups of pCG POPC and lysine residues could explain the time-lag in peptide-bilayer interactions seen in Figure 4.21b. However, the longer side chains of lysine residues and its charge distribution on the peptide, facilitates binding to even pCG POPC membranes. In our study, only one peptide is present in the system (Lipid:Peptide is 240:1). With higher concentration of the peptide, repulsive interaction between the peptide side chains (lysines) and pCG POPC is likely to be more pronounced. Binding of cationic β-hairpin AMPs to zwitterionic lipid membranes have been previously observed in protegrin-1(PG-1) known to interact with both zwitterionic and anionic lipids [200, 201]. CMP, the cysteine deleted analog of tachyplesin, is known to bind weakly to zwitterionic POPC vesicles, but remain unfolded [202]. CMP, like SVS-1, folds in the presence of anionic lipids, and is disordered in water. Cationic peptides like TAT [203–206], poly-arginine sequences [207, 208], and penetratin [204, 209] are also known to bind to DOPC and DPPC lipid membranes. Atomistic free energy studies with OPLS forcefield predicts lysine and arginine residues to have favorable interfacial free energies of partition with DOPC bilayers [210]. It is also important to remember that the SVS-1 peptide used in this study is mapped to our minimalistic CG model, where we have only one type of hydrophobic and charged residue. Therefore, valine and lysine residues in our simulation study essentially represent

a hydrophobic and charged residue prototype and not the properties of the residue themselves.

Finally, the trend in Coulombic interaction of GL1 and GL2, both with lysines and phosphates in (a) pCG POPC is minimal and almost non existent (brown and cyan solid curves in Figure 4.27d and 4.27f), and (b) absent in POPSnd. Although the LJ interactions of GL1 and GL2 show a decrease in energy values with increase in L_c, similar to most other peptide-lipid interactions(brown and cyan dashed curves in Figure 4.27d and 4.27f), this is largely because of the location of the peptide within the bilayer.

4.5 Conclusion

We have explored the role of lipid head group dipoles in structural and dynamical properties of an anionic (POPS) and zwitterionic (POPC) bilayer. We have done this by introducing polarization into polar coarse-grained lipid head group. The model has roots in the MARTINI force field and has been built to be compatible with our recently developed protein model that captures *de novo* folding of secondary and super-secondary protein structures [30]. Our model is slightly more expensive in computational cost. In simulations of the benchmark system with 240 POPC lipids and 7757 CG water molecules, our model is slowed down approximately by a factor of two in comparison with the MARTINI system, which mostly arises from the shorter time step in our model. Several interactions involving polarizable CG beads have been re-parametrized. It should also be noted that, we have not tested all the bead

types of the MARTINI force field, and our lipid model is not transferable to the other lipid types, because it is intended to be used specifically with our peptide model to study membrane-induced peptide folding.

The physical properties of the POPS and POPC bilayers which formed spontaneously from a random configuration, exhibit reasonable descriptions of lipid behavior. To examine the performance of our model, we explored structural, dynamic and electrostatic properties, such as the cross-bilayer density profile, area per lipid, bilayer thickness, mean squared displacements, line tension, dipole potential, dielectric profile, head group orientation and formation of lipid clusters. Comparison of these properties with experiments and/or all-atom simulations shows good agreement. Our model also captures the right trend in membrane interface electrical potential, which the MARTINI model fails to capture.

The model predicts formation of lipid clusters in PS bilayers in agreement to all-atom simulations, but in contrast to the the MARTINI model. In particular, we have shown that dipole interactions are crucial in stabilizing lipid cluster formation in PS bilayers by mimicking the hydrogen bonding network present in the head group region of atomistic PS bilayers. The presence of PS lipid cluster formation causes a distinction in area per lipid between POPC and POPS bilayer in our model. That is, the presence of head group dipoles in POPS results in a condensation effect by the alignment of headgroup dipoles, which manifests as a decrease in area per lipid. In addition, the model indicates, in agreement with all-atom data, that the serine group lies at the same vertical position of the phosphate group. This is in contrast to the MARTINI model where the serine is found above the phosphate position. Also, more

subtle changes to head groups, on interaction with monovalent ions are observed. With the addition of 1M NaCl, area per lipid of both POPS and POPC bilayers decreased due to an electrostatic condensation effect, and the average number of ion bridges formed between lipids increased.

We studied POPS mediated folding of anticancer peptide SVS-1 to explore the effects of lipid head group interactions in membrane-induced peptide folding. With pCG, we were able to observe membrane mediated folding of SVS-1 into β-hairpin with anionic bilayers, in agreement with experimental observations. The driving forces involved in folding include PO4-lysine interaction, valine-alkyl interaction, intra-peptide interaction and CNO-peptide interaction. PO4-lysine interaction contributes in attracting the peptide to the anionic bilayer, while valine-alkyl interaction and intra-peptide interaction play a role in stabilizing the β-turn conformation. We do not observe SVS-1 folding with pCG POPC, POPSnd, or in water, where it is intrinsically disordered. This is in agreement with experimental studies [144].

One of the reasons we observe SVS-1 folding in pCG POPS bilayers, and not pCG POPC or POPSnd is because, a subtle balance between intra-peptide interaction (BB-BB) and peptide-lipid bilayer (BB-PO4 and BB-CNO) interaction is achieved only with pCG POPS. In the case of pCG POPC and POPSnd, the peptide-lipid interactions are more stronger (BB-PO4 in POPSnd and, BB-PO4 along with BB-NC3 in pCG POPC), thus decreasing intra-peptide interactions (BB-BB). The presence of added dipole particles in the CNO or serine head group region in pCG POPS, leads to higher lipid-lipid interaction, which is also the primary reason for head-group mediated lipid clusters observed in these bilayers. This causes lower lipid-peptide in-

teractions and subsequently, higher intra-peptide interactions. Whereas, both in the case of POPSnd and pCG POPC, there is less (if any) dipole-dipole interaction between lipids in a bilayer, which leads to increased peptide-lipid interaction and hence decreased intra-peptide interaction. This is also the reason clusters are not formed with MARTINI force field or in pCG POPC bilayers. The role played by the ester groups (GL1 and GL2) in all three systems (pCG POPS, pCG POPC, POPSnd) is minimal for SVS-1 peptide. There is also a lag in peptide-bilayer interaction for pCG POPC system, due to electrostatic repulsion between lysine residues and positively charged choline beads. In conclusion, our results also suggest that there is an intricate balance between intra-peptide, peptide-lipid and lipid-lipid dipole interactions, which our CG model captures.

Chapter 5: Effect of Monovalent Ion Size on Lipid Domain Formation in Anionic-Zwitterionic Lipid Mixtures

5.1 Overview

In this chapter, the role of monovalent ion (M^+) sizes in lipid head-group driven microdomain formation in PC-PS lipid mixtures is investigated with WEPMEM.

5.2 Introduction

Cellular membranes are not homogenous in nature and are composed of a multitude of lipids and proteins resulting in interactions, some more favorable than others. These interactions give rise to many interesting patterns with distinct physical and biological properties, as a result, there are regions of order and disorder in cellular membrane [211]. Some regions are thicker, some are thinner. Some are more crowded than others. Different cells have different membranes. The structure of these membranes is constantly regulated [211]. Lipid phase regulation by cholesterol is well studied, from both experimental and computational studies, cholesterol is known to associate with saturated lipids to form liquid-ordered (L_o) domains and induce phase separation in lipid mixtures [163, 212–214]. The nature of phase separation in choles-

terol ternary mixtures is attributed to a tail induced ordering effect [215].

The role metal ion binding (M^+) to biological membranes is of interest as it affects structure, dynamics, stability of lipids which in turn affects folding, binding and insertion of proteins. Ion interaction with phospholipids is driven by Coulombic forces near the head group region and is therefore more pronounced for anionic lipids [216]. Both the structure and behavior of membranes are dependent on ion type and strength. Among monovalent metal ions of biological significance ($K^+, Na^+ and\ Li^+$), K^+ and Na^+ is known to produce only minor changes in bilayer structure, stability and chain packing [217]. Whereas, in sharp contrast to this, even small concentrations of Li^+ is known to influence the lipid state of phosphatidylserine (PS) by increasing its critical temperature, and influencing transformation from a liquid disordered state to a gel state [217–219]. The exact molecular underpinnings of such contrasting behaviors is not understood. The effect of lithium on membranes is also significant due to its use in treatment of psychiatric and neurological disorders [220]. Phosphatidylserine (PS) and phosphatidylcholine (PC) are among the major anionic and zwitterionic phospholipids of neural tissues [221]. Thus understanding the size effect of monovalent ions in modulating structural and dynamic properties in PC-PS mixtures could provide valuable information regarding many biological processes.

There exist a large number of CG models that have yielded significant results and extended our understanding of membrane molecular processes including cholesterol or tail-induced phase separation in lipid mixtures [1, 164–168, 214]. To our knowledge all CG simulations on lipid domain formation in mixtures is induced by tail ordering, and none that is induced by head-group interactions. A MC lattice model on PC-PS

mixtures showed that electrostatic interaction influences cluster size and shape of PC and PS domains [222]. This study is one of the first to characterize domain formation in lipid mixtures, driven by head-group interactions.

In this chapter, we use our recently developed Water Explicit Polarizable Membrane Model (WEPMEM) (described in chapter 4) to characterize the effect of monovalent ion sizes on 1:1 POPC-POPS lipid mixtures. WEPMEM has roots in the MARTINI force field, and is combined with Yesylevskyy's polarizable water model [169]. All beads in WEPMEM have the same size of 4.7Å (1.00σ), and the ions are modeled as hydrated ions. With decrease in size of the ions, the water-coordination number of the ions change as well [223]. From literature, the first minima of the hydration shell for Li^+ is 3.1 Å, Na^+ is 3.5 Å and 3.7 Å for K^+. Therefore, we can model different monovalent ion-types by decreasing the size of the bead, σ. With this study, we can predict behavior of monovalent ions with different sizes on 1:1 POPC/POPS lipid bilayers. Our study suggest that at a specific range of M^+ size, we observe partitioning of the lipid mixture into (a) ion bound gel-like POPS domains and (b) water bound liquid-like POPC domains.

5.3 Methods

5.3.1 System Setup

Bilayer systems were built with our new model WEPMEM, which uses a 4:1 mapping scheme. For the study on the effect of M^+ sizes, a 1:1 ratio of POPC and POPS molecules, with a total of 240 lipids was randomly constructed. Our initial bilayer is

symmetric, with equal lipids of each type on each leaflet. Four distinct M^+ sizes are explored in this study, starting from 1.0σ, which is the size of all beads used in the model, to 0.9σ, 0.8σ and 0.7σ. All ions and counterions are placed in the solvent at time 0ns. An ion concentration of 0.4 aqueous oM is used consistently throughout this study. Although this concentration is very high and not comparable to physiological conditions, we are interested in understanding changes in ion binding modes, which should not be affected by the concentration used in the study.

5.3.2 Simulation Parameters

All simulations are carried out at 300K and 1atm pressure. The Nosé-Hoover [224, 225] thermostat with a time constant of 1 ps is used to maintain a temperature of 300K, and the Parinello-Rahman [226] barostat with a time constant of 1 ps and an isothermal compressibility of $7.17\times10^{-6}(kcal{\cdot}mol^{-1}nm^{-3})^{-1}$ is used to keep the semi-isotropic pressure at 1 bar in the z direction and 1 bar in the x, y plane. The time step is 5 fs and the neighbor list is updated every 10 steps. The long-range electrostatic interactions with periodic boundary conditions (in x, y, z directions) are evaluated using the Particle Mesh Ewald (PME) method [227] with a global dielectric constant of 2.5. We use the Shift scheme beginning from 0.9 nm and switch the Lennard-Jones interaction to zero at 1.2 nm. The LINCS algorithm [228] is used for constraining dummy bonds inside polarizable beads. A total of 300ns data is collected of which the last 100ns is analyzed, unless specified otherwise.

5.3.3 Analysis

To characterize ion mediated lipid head group clusters, a distance-based clustering method is adopted. Neighboring lipids that are connected via an ion, within either a cutoff distance between (a) PO4-ION of 5.5Å or (b) CNM-ION of 2.0Å, are classified as a cluster. These cut-offs are obtained from PO4-ION and CNM-ION RDF peaks for $0.8\sigma M^+$. The `NetworkX` 1.6 module in `Python` 2.7 is used to perform a connected-components labeling analysis and classify connected lipids in the bilayer as clusters [179].

Area per lipid and bilayer thickness was evaluated using GridMAT-MD [229]. S_{CD} order parameter is used to calculate tail order by computing tilt of each tail bond with the bilayer normal [230]. Hydration curves are obtained by integrating lipid-water RDF.

5.4 Results and Discussions

5.4.1 Effect of Ion Size on Cluster Formation

Figure 5.1 a-d shows the time evolution of the number of lipids in the largest POPS cluster for systems with 1.00σ, 0.90σ, 0.80σ and 0.70σ of M^+ respectively. There is an increase in largest cluster size with time for systems with both $0.90\sigma M^+$ and $0.80\sigma M^+$, whereas lipid clusters with $1.0\sigma M^+$ and $0.70\sigma M^+$ do not grow with time. That is, with initial decrease in ion size, an increase in ion mediated lipid cluster is observed, however, on further decrease (to 0.70σ), the growth of clusters

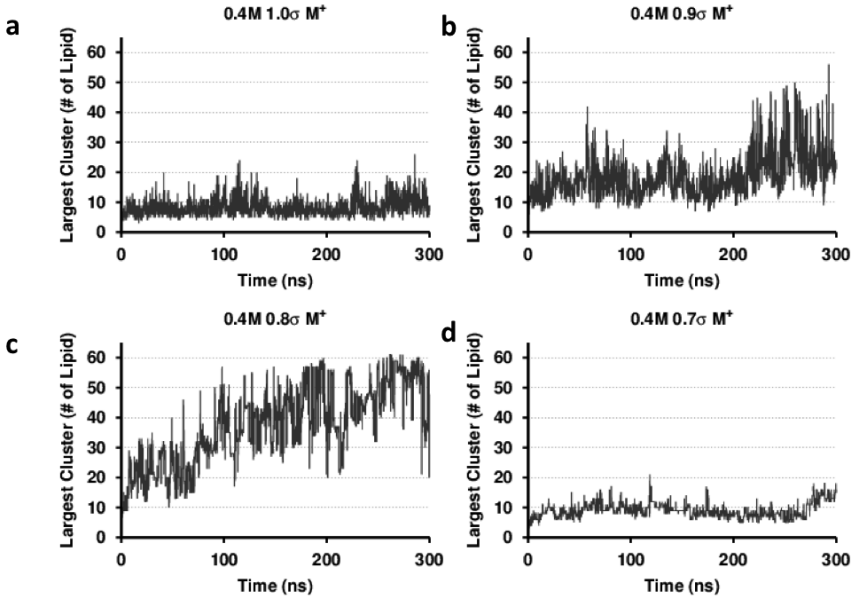

Figure 5.1: Cluster time evolution of system with (a) $1.00\sigma M^+$, (b) $0.90\sigma M^+$, (c) $0.80\sigma M^+$ and (d) $0.70\sigma M^+$.

is restricted. Since the total number of lipids in each leaflet is 120, and the number of POPS lipids, 60; in the system with $0.80\sigma M^+$, all POPS lipids are bound to each other via ions by 200ns. From the fluctuations in cluster size in Figure 5.1, it is interesting to note that the clusters are dynamic and are not stuck. On comparing the cluster size distribution for systems with different ion sizes (see Figure 5.3 a-d), it is clear that for sizes 0.90 and $0.80\sigma M^+$ (Figure 5.3 b and c), there is (a) a more diverse distribution of clusters and (b) more large-sized clusters. Whereas for systems with 0.70 and $1.0\sigma M^+$ (Figure 5.3 a and d), there are multiple clusters with less than 20 lipids, and none beyond 30 lipids.

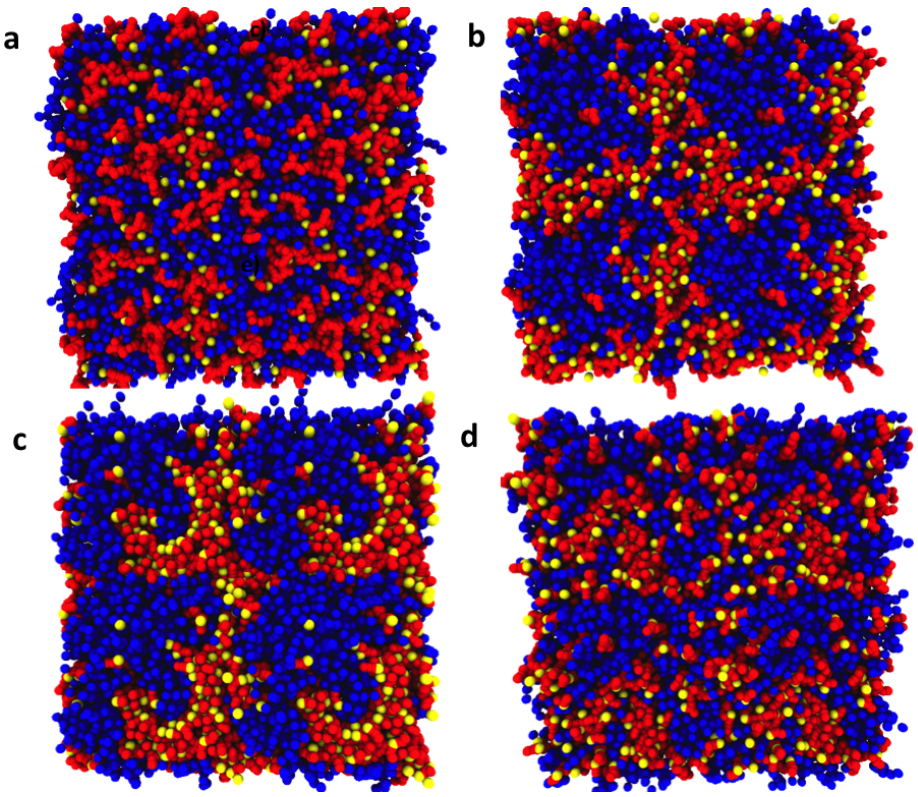

Figure 5.2: Representative snapshots of bilayer system with (a) $1.00\sigma M^+$, (b) $0.90\sigma M^+$, (c) $0.80\sigma M^+$ and (d) $0.70\sigma M^+$. Colors: POPC in blue, POPS in red, M^+ in yellow.

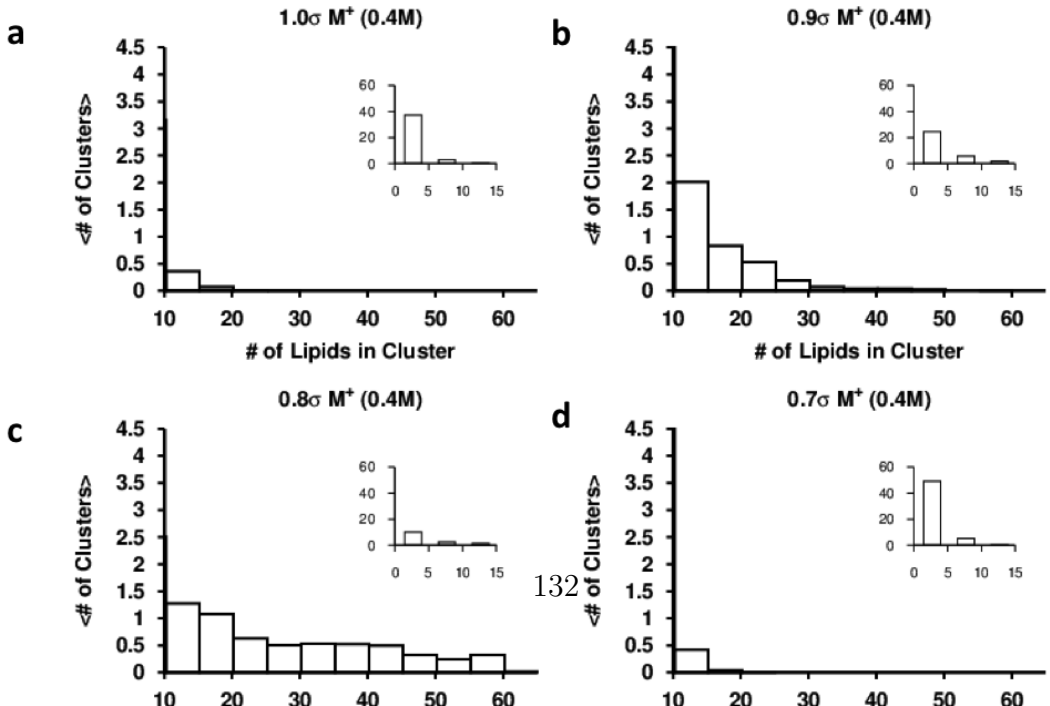

The distinction between the effect of ion sizes is more obvious by comparing snapshots of the 240 lipid bilayer at 300ns (see Figure 5.2). The blue and red lipids represented in Figure 5.2 are POPC and POPS respectively, and M^+ within 7Å of phosphate beads is represented in yellow. Table 5.1 quantifies the number of ions within 7Å of POPS PO4 and POPC PO4 for the snapshots represented in Figure 5.2 (see Figure 5.4 for data from last 100ns). With decrease in ion size, with the exception of $0.70\sigma M^+$, (a) more M^+ partition into the bilayer (also evident from Figure 5.6) and (b) M^+ preference for POPS increases.

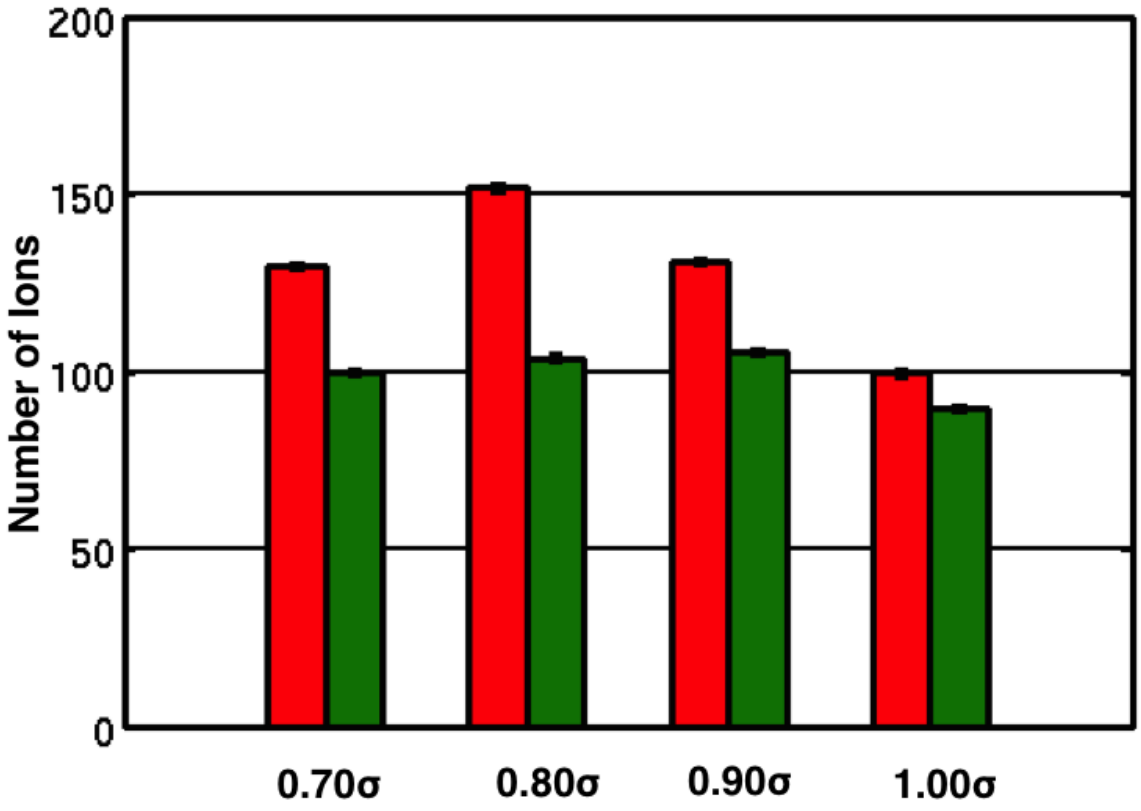

Figure 5.4: Number of differently sized ions around POPC (green) or POPS (red) over the last 100ns of data collected.

Table 5.1: Number of M^+ near POPC and POPS for Figure 5.2

Ion Size	M^+ near POPS	M^+ near POPC
1.0σ	76	47
0.90σ	109	62
0.80σ	128	36
0.70σ	118	42

5.4.2 Effect of Ion Size on Bilayer Structure Properties

We then turned to the effect of ion interaction on the properties of the bilayer. The first question to address is, if the typical properties of condensation effect follows the same trend as the cluster size evolution. The area per lipid (APL) for system with $1.00\sigma M^+$ is 60.5 ± 0.05Å , $0.90\sigma M^+$ is 58.98 ± 0.02Å , $0.80\sigma M^+$ is 57.5 ± 0.01Å and $0.70\sigma M^+$ is 59.25 ± 0.05Å showing the same expected trend in condensation. Figure 5.5 shows the change in tail order parameter for both POPC (grey curve) and POPS (black curve) lipids in the four systems. POPS tails in the system with $0.80\sigma M^+$ shows a slight increase in order compared to both (a)POPC tails in the same system and (b)POPS tails in other systems. This suggests that the binding of ion to the head group region that leads to a lipid condensation effect, also induces

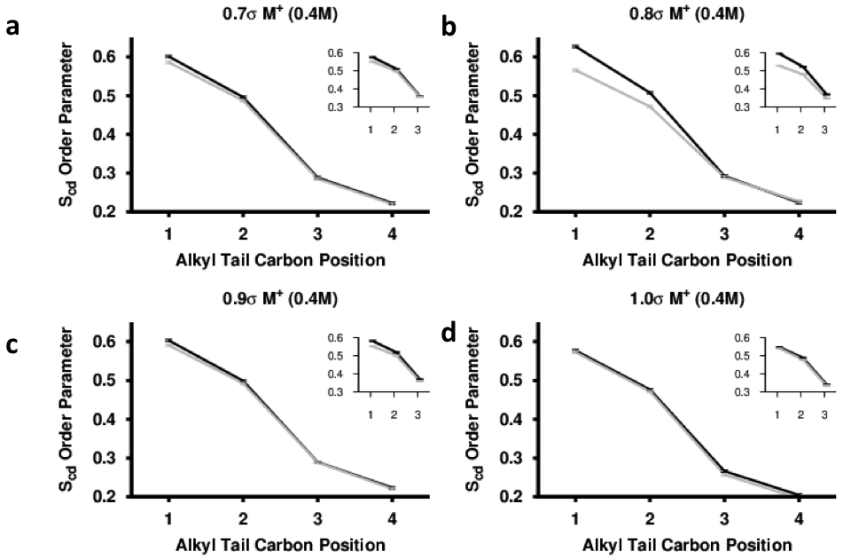

Figure 5.5: Order parameters for POPC and POPS lipids for systems with (a) $1.00\sigma M^+$, (b) $0.90\sigma M^+$, (c) $0.80\sigma M^+$ and (d) $0.70\sigma M^+$.

order in the tail region. This increase in tail order is the most significant near the head groups because of the ion interaction near this region. A MD study on the effect of monovalent ions on DPPS, shows similar trend of (a)decrease in APL with decrease in ion size, from Na^+ (54.00 $\pm$ 0.01Å), to Li^+ (51.00 $\pm$ 0.06Å), and (b) increase in tail order when Na^+ is replaced with Li^+ [231]. The same study also suggests that the presence of Li^+ decreases lipid-lipid interaction pairs only to increase lipid-ion-lipid interaction pairs.

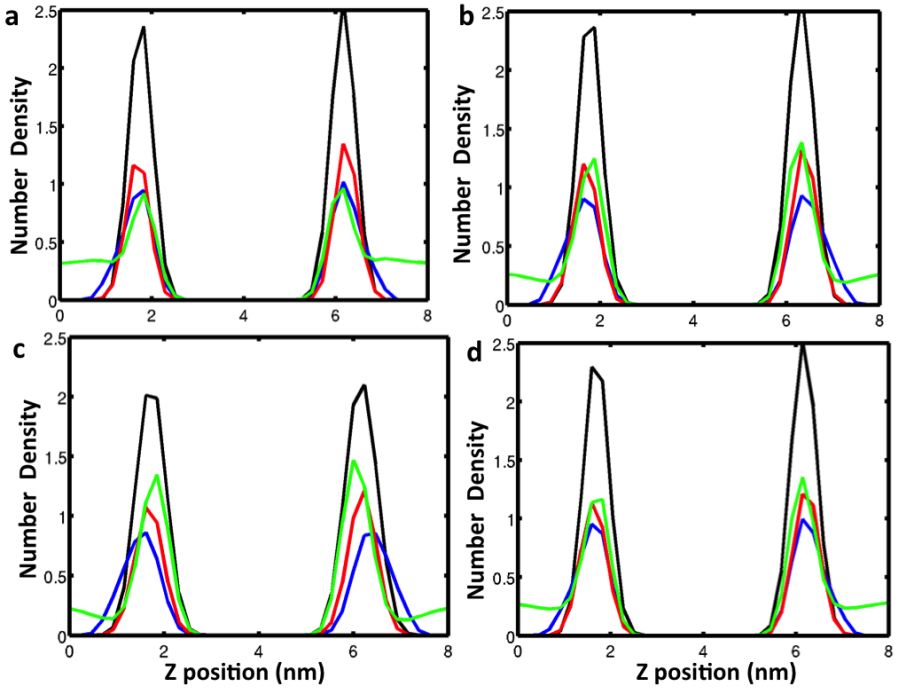

Figure 5.6: Density distribution of phosphates (black curve), CNO (red curve), M^+ (green curve) and NC3 (blue curve) for (a) $1.00\sigma M^+$, (b) $0.90\sigma M^+$, (c) $0.80\sigma M^+$ and (d) $0.70\sigma M^+$.

5.4.3 Mechanism of Lipid Cluster Formation

There is clearly a range of monovalent ion sizes where there is growth of ion mediated lipid clusters. These clusters have a characteristic decrease in APL and increase in tail order, suggesting a "condensation" like effect. But the question remains, why only 0.90σ and 0.8σ and not 1.0σ or 0.7σ exhibit lipid domain formation , what is special about the ion size range at which this condensation effect is observed. To answer this question, we looked at interaction energies and ion occupation near the lipids. On comparing Figures 5.6 a-d, it is clear that with decrease in ion size, till

0.8σ, there is both (a) a deeper ion penetration into the bilayer, as evident from the shift in ion number density curve (green curve) towards the phosphates (black curve) and (b) increase in number of ions in the bilayer. Whereas this pattern is broken for the system with $0.7\sigma M^+$, where there is less number of ions in the bilayer and more ions in water (see Figure 5.6 d). NMR studies on monovalent (Na^+, K^+, Li^+)and divalent ion (Ca^{2+}, Mg^{2+}) ion binding to 5:1 POPC: POPS mixtures suggest that divalent ions, along with Li^+ are more deeply buried into the membrane in comparison to Na^+ and K^+ [232].

To understand this difference, we looked at the number of ions around PO4 and CNO (serine) of POPS lipids for different systems. From Figures 5.7 a and b, the $0.70\sigma M^+$ is located more closer to both POPS PO4 and CNO (solid black curves), however more number of $0.80\sigma M^+$ is located near POPS PO4 and CNO. In fact, there is a higher probability of finding a $0.80\sigma M^+$ near either of the two POPS head groups than any other ion. What this suggests is that, there is a certain range of monovalent ion size, where the ion can favorably interact with both PO4 and CNO. If an ion preferentially interacts with both the PS head groups, there are more combinations of ions bridging lipids together to form larger clusters. One such cluster is represented in Figure 5.7 c, where the $0.80\sigma M^+$, shown in green is seen interacting with both POPS PO4 and CNO, thus bridging three lipids together. Infrared studies on DMPS bilayers with Li^+ and Ca^{2+} shows both ions preferentially interacting with PO4 and carboxylate groups of serine resulting in lipid aggregation [219]. This suggests that our monovalent CG ion ($0.80\sigma M^+$) shares binding mode characteristics with Li^+.

To understand the role of interaction energies, we looked at electrostatic and LJ

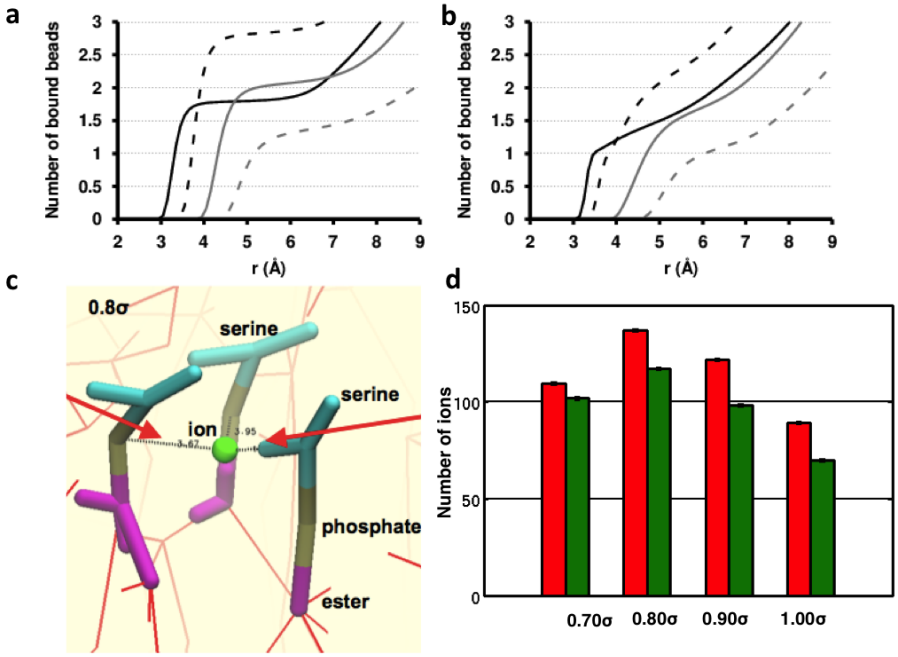

Figure 5.7: Number of ions near (a)PO4 and (b)CNO. $0.70\sigma M^+$ in solid black, $0.80\sigma M^+$ for dashed black line, $0.90\sigma M^+$ in solid grey line and $1.00\sigma M^+$ in dashed grey line. (c) Representative snapshot of typical cluster of 3 POPS lipids with $0.80\sigma M^+$, shown in green is ion, serine in cyan, phosphate in tan and ester in pink. (d) Number of differently sized ions bound to PO4 (red) and CNO (green).

contributions of ion-PO4, ion-CNO, ion-GL1 and ion-GL2, in all the four systems (Figure 5.8). With decrease in ion size, there is a decrease in energy with all the head groups, with the contribution from PO4-M^+ being the lowest, with the exception of $0.70\sigma M^+$ (see Figure 5.8 d). The role of ester-ion interaction is minimal in our model. At $0.70\sigma M^+$, the ion-CNO energy is lower than ion-PO4. This does not mean there are more ion-CNO interaction pairs, as evident from Figure 5.7 a and b, just stronger interaction. At $0.70\sigma M^+$, there is also more ion-water interaction which competes

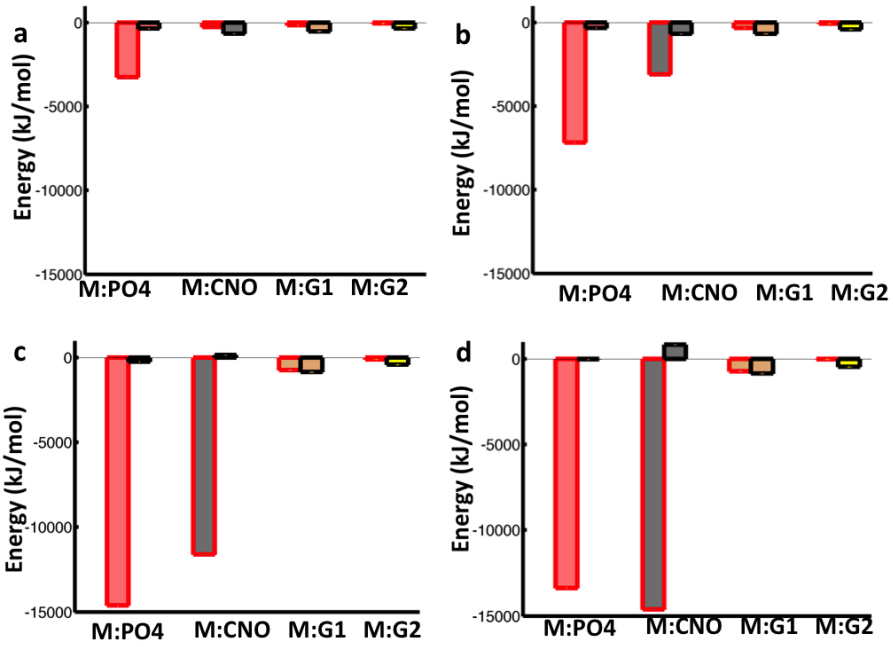

Figure 5.8: Total LJ (black bordered bars) and Coulombic energies (red bordered bars) for (a) $1.00\sigma M^+$, (b) $0.90\sigma M^+$, (c) $0.80\sigma M^+$ and (d) $0.70\sigma M^+$.

with bilayer-ion interaction, hence lesser ions partition into the bilayer, in comparison to $0.80\sigma M^+$. Also, CNO can interact with each other and with PO4 of other lipids, to have an ion interact very strongly with just CNO, can disturb the dynamics of the head group region. Whereas, at $0.80\sigma M^+$, the ion interacts with both PO4 and CNO, just enough to bridge lipids together and not cause repulsion between different beads. This suggests that there is an intricate balance in M^+-PO4 and M^+-CNO that is required for lipid domain formation. Studies on monovalent ion interaction with PS bilayers suggest that ions like Na^+ and $(NH_4)^+$ display weak interactions with PS, unlike Li^+, Ca^{2+} or Mg^{2+} [233]. One of the reasons why $0.70\sigma M^+$ interacts more with CNO is due to nature of the polarized bead, and it could be a property of

our model. Our future work will involve polarizing the PO4 bead to understand how that affects bilayer properties.

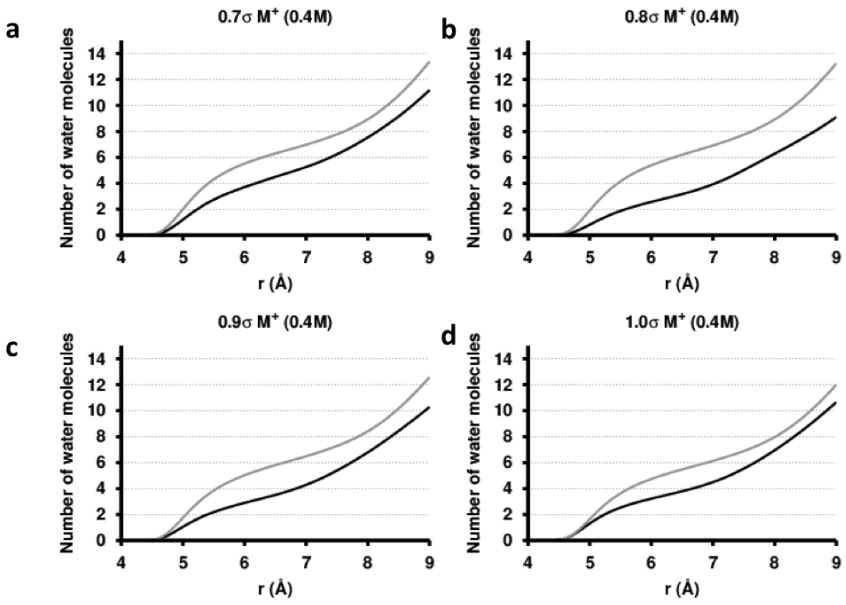

Figure 5.9: Hydration curves for POPC (grey curve) and POPS (black curve) lipids for (a) $0.70\sigma M^+$, (b) $0.80\sigma M^+$, (c) $0.90\sigma M^+$ and (d) $1.00\sigma M^+$.

And finally we looked at the effect of ion dehydration. Ions that are known to induce domain formation in PS mixtures, like calcium, exhibit a dehydration effect, displacing water bound to lipids [153,234,235]. To see if we observe a similar effect, we evaluated hydration curves for POPC and POPS lipids in all the four systems (Figure 5.9). The dehydration effect, that is, the release of lipid-bound waters from the lipid as interaction with ions increase, is most pronounced for the system with $0.80\sigma M^+$ (see Figure 5.9 b). There is both less number of waters around POPS and greater difference in dehydration between the two lipids for this system. Li^+ binding to PS

membranes is also known to cause a dehydration effect. [217–219]. This dehydration observed of POPS bilayers, in the presence of $0.80\sigma M^+$, results in a gel-like state of POPS domains.

As we decrease the size of our CG ion, we see significant changes in ion-lipid interaction. The trend seems to follow the ion behavioral trend of Na^+, K^+ and Li^+, with $0.80\sigma M^+$ exhibiting some characteristics of Li^+. However, it is important to keep in mind that these are CG ions and we cannot make direct comparisons to any real existing ion, without thermodynamic parameterization. But, even without direct comparisons, we can predict that some monovalent ions are special in the way they influence lipid structural and dynamic properties, and hence play crucial roles in biological functions.

5.5 Conclusion and Future Work

We see a monovalent ion-lipid head group driven lipid domain formation in POPC-POPS mixtures. This effect has a size dependence, that is, monovalent ions within a certain size range, exhibit selective partitioning to POPS, inducing ion mediated lipid clusters. This is, to our knowledge, one of the first MD studies to show head group driven phase separation in lipid mixtures. We are currently evaluating the effect of concentration of $0.80\sigma M^+$ on PC-PS mixtures. We are also studying the effect of system size and time scale by simulating bilayer systems with 960 lipids, and collecting microsecond data.

Chapter 6: Effect of SVS-1 Concentration on POPC and POPS Lipids

6.1 Overview

In this chapter, the role of SVS-1 concentration in lipid clustering in the presence of pure POPC lipids, and 1:1 POPC/POPS mixed lipids, is discussed.

6.2 Introduction

Antimicrobial peptides (AMPs), are short amphipathic, cationic proteins secreted by a variety of organisms. Hundreds of these peptides have been studied. They are known to kill bacteria, fungi and can even be adapted to kill cancerous cells [236]. This is because, they can interact selectively with anionic lipids in cell membranes. AMPs adopt an extended conformation in water and acquire secondary structure on interaction with cellular membranes. Upon partitioning, binding and folding, they penetrate the membrane and can induce lysis. However, the mechanism or mode of action is distinct for each peptide [236]. The literature on experimental and computational characterization of biophysical properties of AMPs is vast [145–148].

Multiple bilayer disruption mechanisms have been proposed for AMPs, all of which depend on membrane composition and the properties of peptide. Many of these

peptides are known to form pores in lipid membranes, some of them include barrel-stave, toroidal and carpet pore mechanisms [237]. In both carpet-like mechanism and toroidal pores, the integrity of membranes is lost. Whereas, in the barrel-stave model, the head groups remain on the membrane surface.

SVS-1 is one such peptide, like other AMPs, SVS-1 is disordered in the aqueous phase (bioinactive), but is fully structured upon partitioning onto an anionic interface (bioactive) [144]. This anticancer peptide is known to fold into a β-sheet on interaction with negatively charged vesicles [144]. Studies of SVS-1 with POPC and 1:1 POPC/POPS vesicles shows leakage only when anionic lipid, POPS is present in the environment [144]. CD data suggests that the peptide is folded only in the presence of POPS and not POPC, thus folding and leakage could be coupled for the action of SVS-1.

Although all-atom MD has been used to study AMPs [238], due to time and length scale concerns, CG has gained prominence, especially for the study of protein-lipid membrane interaction [239, 240]. In this work, we describe the effect of peptide concentration of SVS-1 on pure POPC (zwitterionic) and mixed POPC/POPS lipids using both (a) manually constructed bilayers and (b) self-assembly (SA) simulations. We recently developed a protein-like and a lipid CG model, WEPPROM (chapter 2) and WEPMEM (chapter 4), with roots in the martini FF [27]. We have had success reproducing lipid structural and dynamic properties, along with peptide folding and aggregation. Here, we describe the ability of SVS-1 to aggregate POPS lipids upon binding to a mixed bilayer, and the ability of the peptide to get inserted into the membrane, causing leakage, but without the presence of a pore.

6.3 Methods

6.3.1 System Setup and Simulation Protocol

Details of SVS-1 mapping, protein CG FF parameters can be found both in Chapters 2 and 4. Details of CG POPC and POPS mapping and parameters can be found in Chapter 4. For simulation parameters, refer Appendix A.

All simulations are performed with 1:25 peptide:lipid ratio [144]. For the bilayer simulations, two systems with all POPC and 1:1 POPC/POPS with a total of 240 lipids are used in this study. Simulations with bilayer are set up with 10 randomly placed peptides in water. All peptides are constrained and a 10 ns NPT simulation is performed to allow the counterions to equilibrate. Constrains are removed to collect 100 ns NPT data, all of which are analyzed. For better sampling, we run 4 randomly constructed simulations of each POPC and 1:1 POPC/POPS system. All peptides are fully extended and in water, at time t=0ns. For self assembly simulations, a box of 12nm (in x, y, z directions) is constructed with 240 randomly placed lipids, water molecules (lipid:water is 1:15), counterions and unfolded peptide conformations. 100ns NPT runs is collected for 4 distinct runs, runs where peptide was inserted into the bilayer, were extended to 300ns. Parameters listed above were used, with an exception of isotropic pressure coupling.

6.4 Results and Discussion

6.4.1 Bilayer Simulations

Figures 6.1 a-c shows the time evolution of Fr_{sheet}, L_c and CoM distance between peptide and the POPC bilayer, and Figures 6.1 d-f, the same for 1:1 POPC/POPS bilayer. It is clear from Figures 6.1 a-c, that not all peptides interact with the POPC bilayer, some of them prefer to be in water. Another set of trajectories is presented in Figure 6.3a-c. In all the runs, more than half the number of peptides remained in the water phase, while the ones on the bilayer remain extended and unfolded (see chapter 4 for more). This behavior of only certain peptides partitioning to the POPC interface is consistent in all the 4 different runs we performed. As discussed earlier in chapter 4, there is electrostatic repulsion between the NC3 head groups of choline and lysine side chain beads that results in this behavior. This electrostatic effect was not too obvious when only one peptide was present in the system. Since SVS-1 is intrinsically disordered in water (see chapter 4), some of these peptides also explore sheet-like conformations (compare magenta curves in Figures 6.1 a and c). Certain peptides in water also interact with each other, forming sheet-like patterns. Figure 6.4 shows snapshots of 3 peptides interacting in water, at different times; all lysine side chains (orange beads) are exposed to water and there are "pseudo-H-bonds" between backbone beads of the peptide.

In the system with 1:1 POPC/POPS bilayer, all the peptides present in the system, bind to the membrane within 20-30ns. Some of the bound peptides are perfectly sheet-

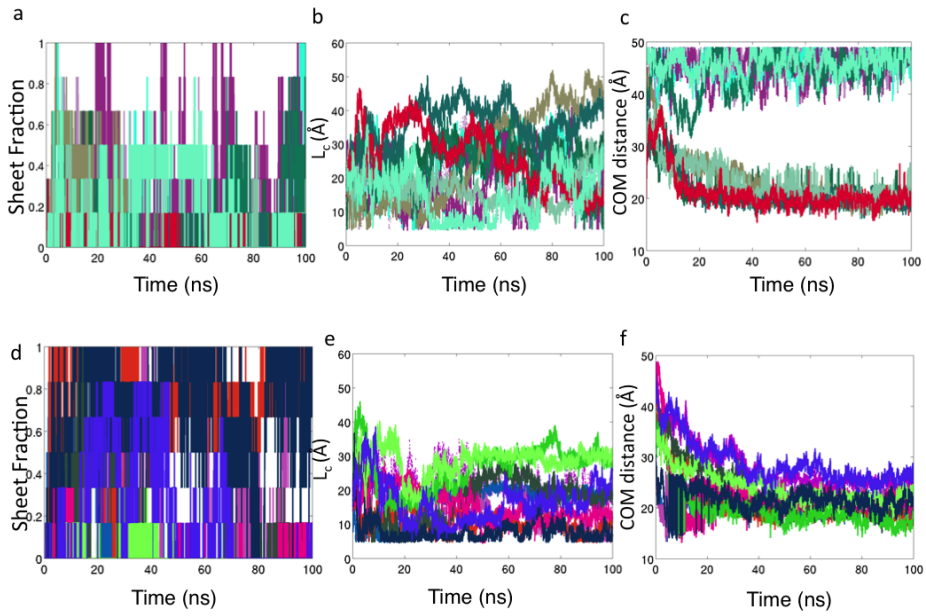

Figure 6.1: Time evolution of sheet fraction (a,d), end to end distance of peptide (b,e) and CoM distance between peptide and the bilayer for POPC and 1:1: POPC/POPS bilayer systems respectively. Different colors represent data for different peptides.

like, while some interact with each other, and others remain unfolded (see Figure 6.1 d-f). With the presence of more than one peptide in the system, there is an additional peptide-peptide interaction that contributes to the observed results. It is important to remember that we do not have any dihedral bias in the system. We then looked at the number of PO4 and alkyl residues of POPS and POPC, within 7 Å of lysines and valines of the bound peptides, for system with POPC bilayer (Figures 6.2 b) and with 1:1 POPC/POPS bilayer (Figures 6.2 a). Since the peptides interact with either bilayer within 20-30ns, the distribution of POPC PO4 and alkyl tails around peptides bound to POPC bilayer, remain constant throughout the simulation (Figures

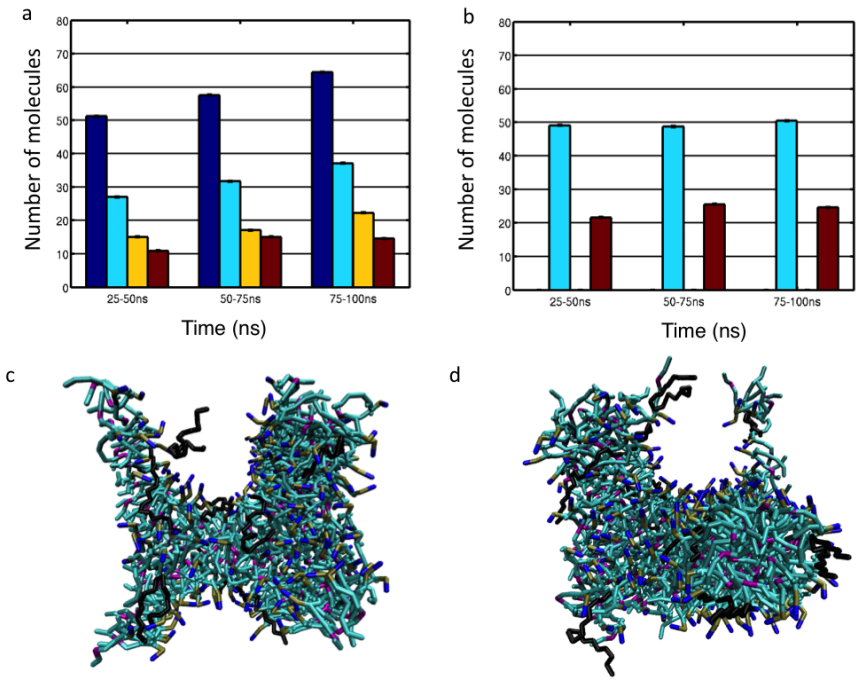

Figure 6.2: Number of POPS PO4 (blue), POPC PO4 (cyan), POPS alkyl tail (yellow), POPC alkyl tail (brown) residues around Lys and Val SC beads of SVS-1 bound to (a) 1:1 POPC/POPS bilayer and (b) POPC bilayer. Snapshot of POPC lipids with SVS-1 after 100ns of self-assembly simulation.

6.2 b). Whereas with 1:1 POPC/POPS bilayer, two main observations can be made, (a) there is preferential partition of SVS-1 into POPS lipids as seen by the increase in blue and yellow bars in comparison to cyan and brown (Figures 6.2 a), and (b) there is an increase in this association with POPS with time. This is only 100ns data, albeit promising, more data is necessary to draw any conclusions. However, the peptide's preference for POPS over POPC is obvious.

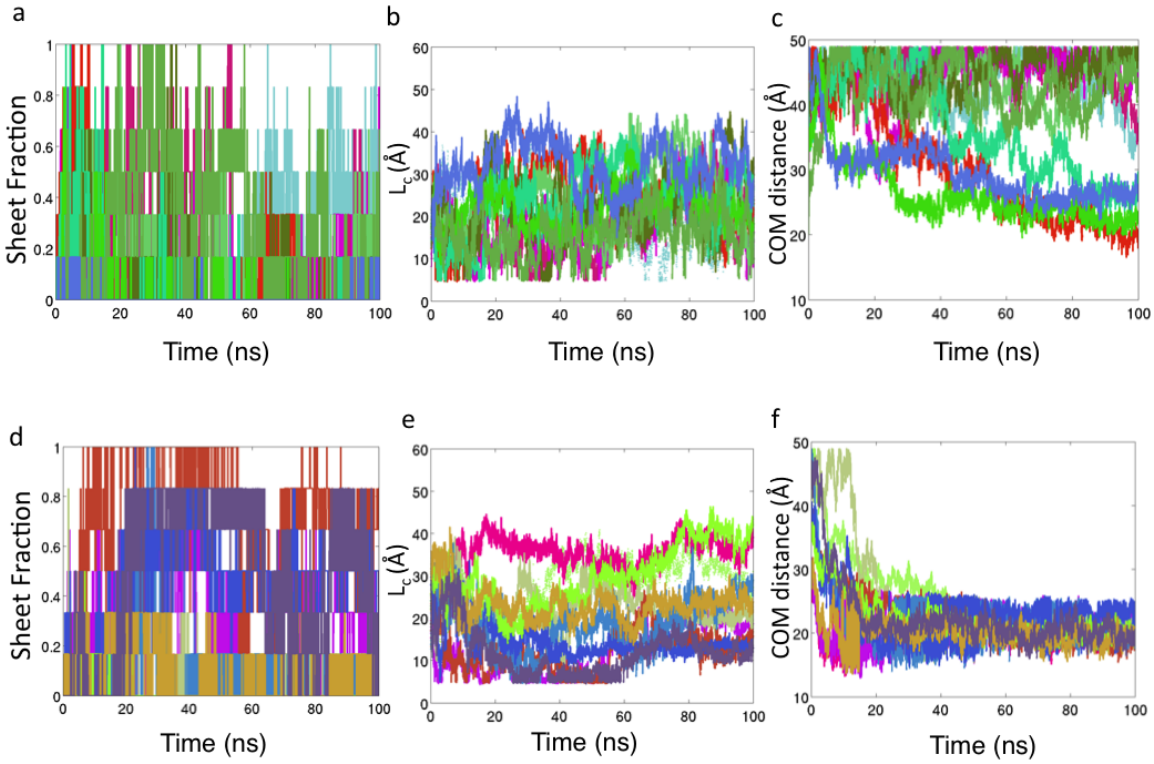

Figure 6.3: Time evolution of sheet fraction (a,d), end to end distance of peptide (b,e) and CoM distance between peptide and the bilayer for POPC and 1:1: POPC/POPS bilayer systems respectively. Different colors represent different peptides.

6.4.2 Self Assembly Simulations

We performed multiple self assembly (SA) simulations to explore various possible lipid-peptide conformations. Without peptides, the lipids self assemble into bilayers within 10ns (see chapter 4). With one peptide added to 120 POPC and 120 POPS lipids, the peptide adopts a sheet-like conformation at the interface between the polar lipid headgroups and water, with valines buried in the hydrophobic alkyl region

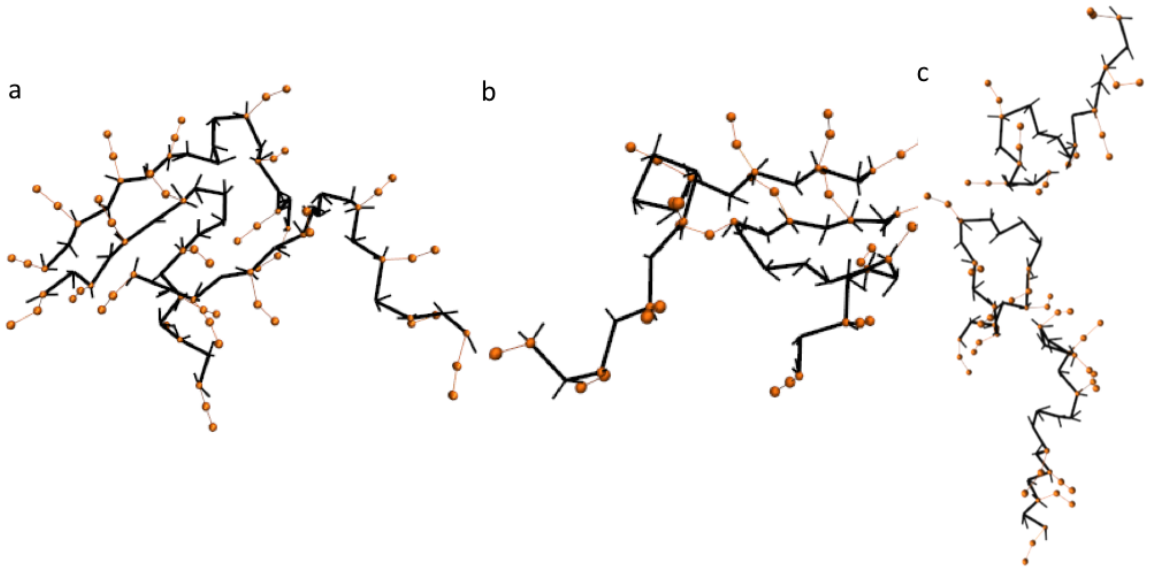

Figure 6.4: Representative SVS-1 conformations seen in water in systems with POPC bilayers. Colors: BB represented in black and LYS in orange.

(results not shown). This is consistent with our simulations with a single SVS-1 peptide and POPS bilayer (see chapter 4).

Figures 6.2 c and d represent typical conformations after 100ns NPT runs with 240 POPC and 10 SVS-1 peptides. Most of the peptides bind to the lipids, but a bilayer is not formed. Two other runs yielded consistent results. Since the initial conformation of the system is a random orientation of lipids and peptides, peptide-lipid interaction is more probable than if all the peptides were located in water above a POPC bilayer, as in the case of the bilayer simulations. This is one of the reasons we see more peptides bound to lipids in the SA runs than the bilayer runs. This also suggests that if a majority of POPC lipids is to be bound to SVS-1 peptides, then the lipids do not have the right driving forces needed to form a bilayer. Thus representing an unlikely scenario. It is also important to note that in SA simulations, due to the ratio of lipid

to water necessary to form a bilayer, there is not a very distinct bulk water phase, which also leads to more peptide-lipid interactions. In the case of 1:1 POPC/POPS, all the peptides interact with the bilayer and the bilayer is formed within 50-80ns in all the four trials (see Figure 6.5 for snapshots of one representative trajectory). In two trials, a folded peptide is seen inserted into the bilayer. This inserted peptide helps passage of water molecules from one leaflet to another, the charges on the lysines are satisfied by interactions with phosphate (PO4), serine (CNO) and choline (NC3). A representative snapshot is depicted in Figure 6.6. This inserted peptide was seen to be stable for 800ns. This suggests that having an inserted peptide in the membrane could be one of the stable states, and a pore might not be necessary for the action of SVS-1 peptides. Many AMPs are known to get inserted into membranes while preserving their secondary structure [167]. Studies on alamethicin suggests that H-bonding interactions between the polar C-terminal side chains of the peptide and the bilayer head groups, act as "anchors" to the bilayer/water interface, and help in peptide insertion [241]. Lipids around the inserted peptide are less ordered than other lipids (see Figure 6.7). POPS lipids (red curves in Figure 6.7), both around the peptide and away, are less ordered than respective POPC lipids (blue curves in Figure 6.7). This is because more POPS lipids are (a) around the inserted peptide and (b) interacting with peptide, even at the interface. We looked at lipid tail angles with the bilayer normal, and the lipids near the inserted peptide are more perpendicular to the normal (see Figure 6.8). This is also visible from red and blue lipid tails in Figure 6.6.

Figure 6.9 shows how the charge on the inserted peptide is satisfied by PO4 from

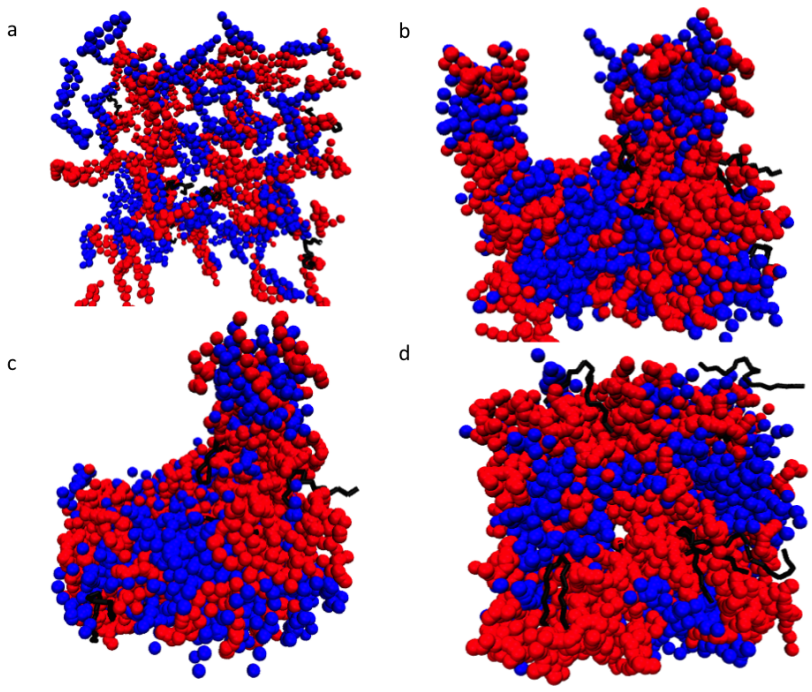

Figure 6.5: Stages in self assembly (SA) simulation with POPC, POPS and SVS-1 peptides.Front view of (a) initial conformation at time t=0ns, (b) conformation at t=20ns, (c) conformation at t=30ns and (d) top view of bilayer at t=40ns. The gap in the bilayer denotes inserted peptide. Colors: peptides in black, POPC in blue and POPS in red.

POPS lipids. The blue bars in this figure denote the number of POPS PO4, the cyan, POPC PO4, around the lysines of the peptide. The yellow and brown bars denote, number of tail beads of POPS and POPC respectively, around the valines of the peptide. The peptide is anchored to either leaflets by lysines-PO4/CNO/NC3 interactions, which makes water transport more conducive. It is also clear from Figure 6.9 that there are more POPS lipids around the peptide than POPC. This is also visually depicted in Figure 6.6. Figure 6.10 a-c shows the total number of water

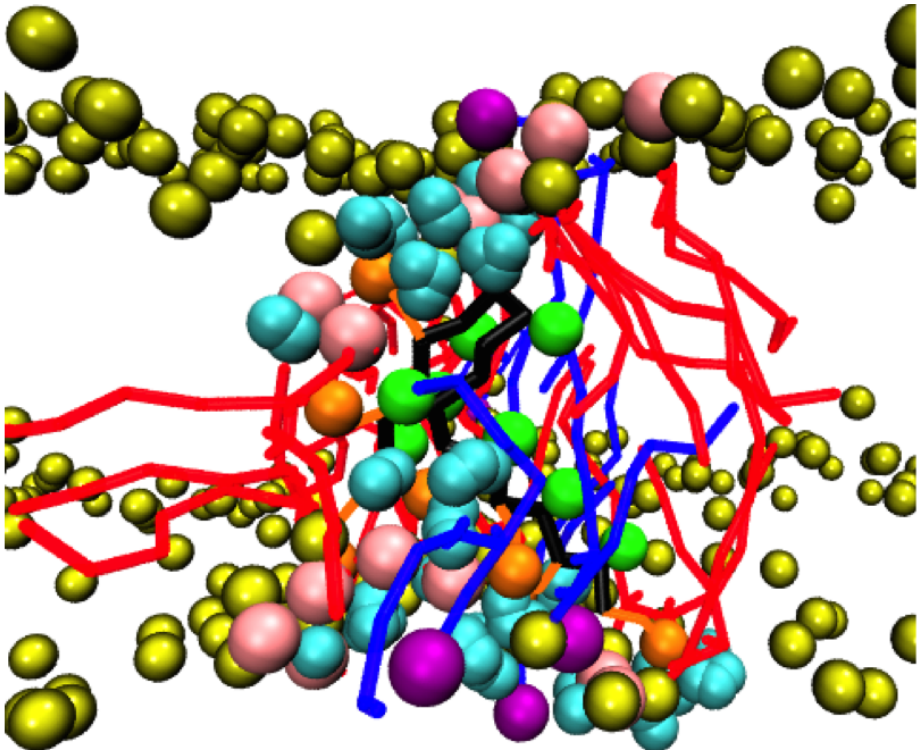

Figure 6.6: Representative snapshot of 1:1 POPC/POPS lipids with SVS-1 after 300ns of self-assembly simulation. Colors: PO4 in yellow, Lys SC in orange, Val SC in green, peptide backbone in BB, water in cyan, NC3 in purple, CNO in pink, POPS within 5 Å around peptide in red,and POPC within 5 Å around the peptide in blue.

molecules in the alkyl region, over 225-250ns, 250-275ns and 275-300ns data of the prototypical SA run with 1:1 POPC/POPS. The plot clearly indicates one distinct, long-lasting wet spot, corresponding to the inserted peptide. These results suggest that the formation of pore is not required to observe leakage or membrane disruption in the presence of SVS-1. We also see that inserted peptide maintains its secondary structure, causing disorder to lipids around the peptide.

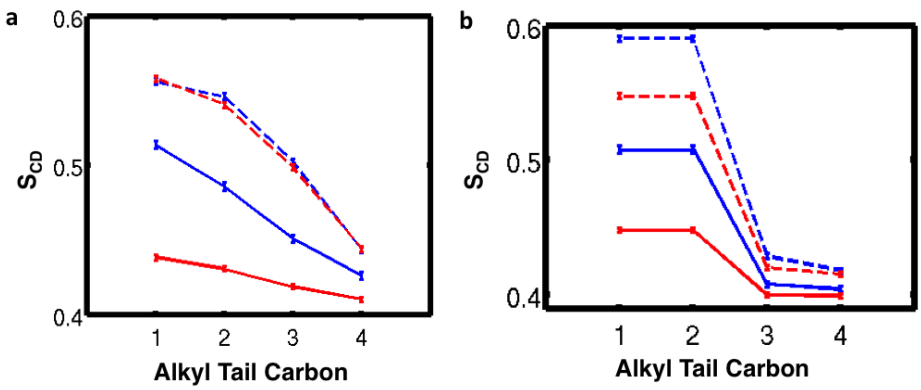

Figure 6.7: (a) Saturated and (b) Unsaturated tail order parameters for POPC near inserted peptide (blue solid curve), POPS near inserted peptide (red solid curve), POPC away from inserted peptide (blue dashed curve) and POPS away from inserted peptide (red dashed curve).

6.5 Conclusion and Future Work

We see that anticancer peptide, SVS-1, selectively partitions to POPS lipids when a mixed bilayer is present in the system. Peptide insertion is observed only with mixed lipids and not pure POPC,. The inserted peptide maintains its secondary structure content. The inserted peptide also pulls in lipids and water to the center of the bilayer, thus creating a polar patch in the bilayer assembly. This suggests that a pore is not essential to see membrane leakage with SVS-1 and anionic lipids. We are currently working on extending all simulations, and increasing sample size. We are also working on POPC and 1:1 POPC/POPS vesicles, with the same peptide:lipid ratio, to understand the role of curvature.

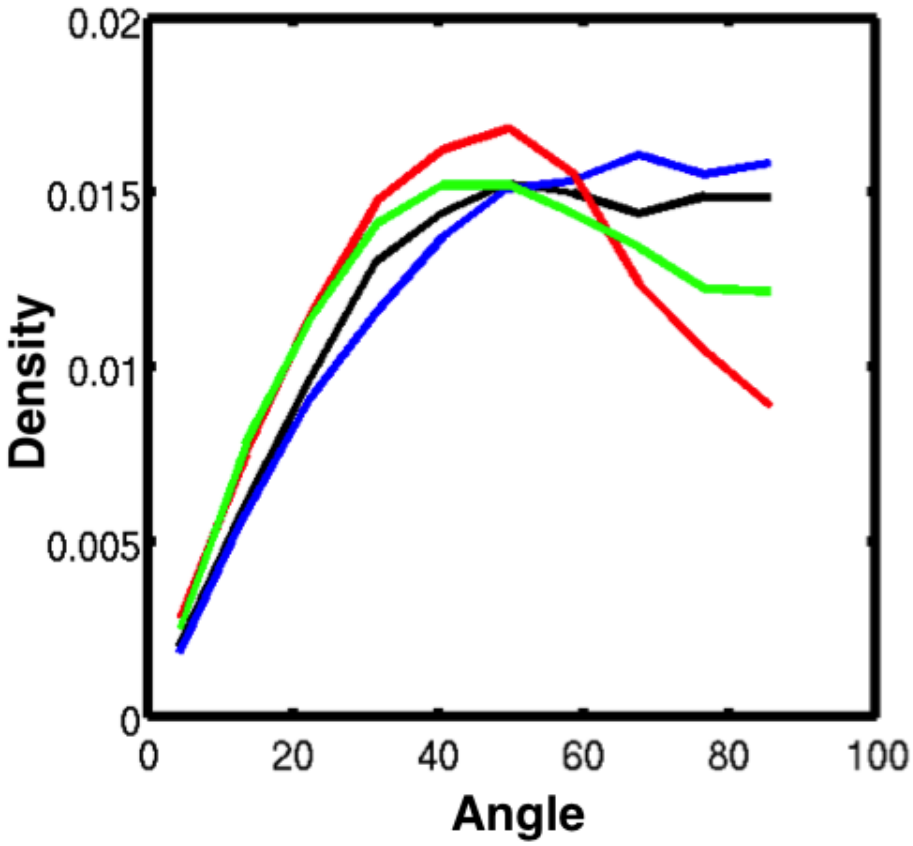

Figure 6.8: Angle distribution between tails and bilayer normal for POPC near inserted peptide (black), POPS near inserted peptide (blue), POPC away from inserted peptide (red) and POPS away from inserted peptide (green).

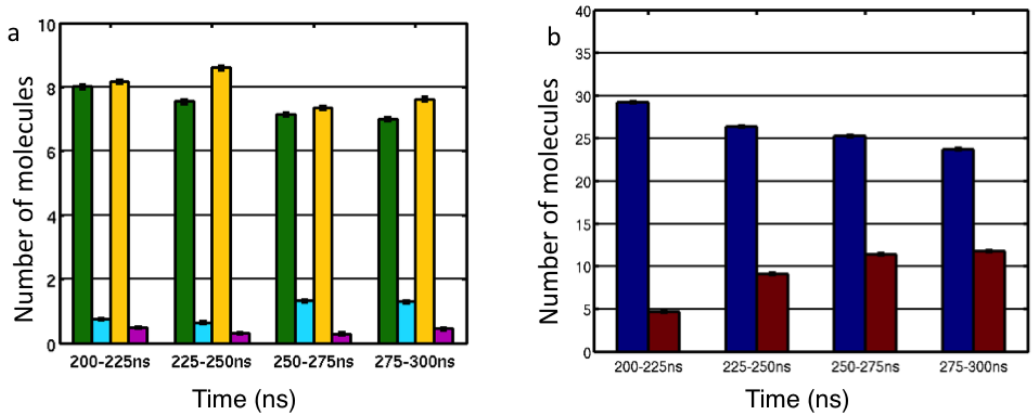

Figure 6.9: (a) Number of POPS PO4 (green), POPC PO4 (cyan), POPS CNO (yellow) and POPC NC3 (purple) around Lys SC beads of inserted SVS-1 peptide in the last 100ns of the trajectory. (b) Number of POPS alkyl tail (blue), POPC alkyl tail (red) residues around Val SC beads of inserted SVS-1 peptide (see Figure 6.6), in the last 100ns of the trajectory.

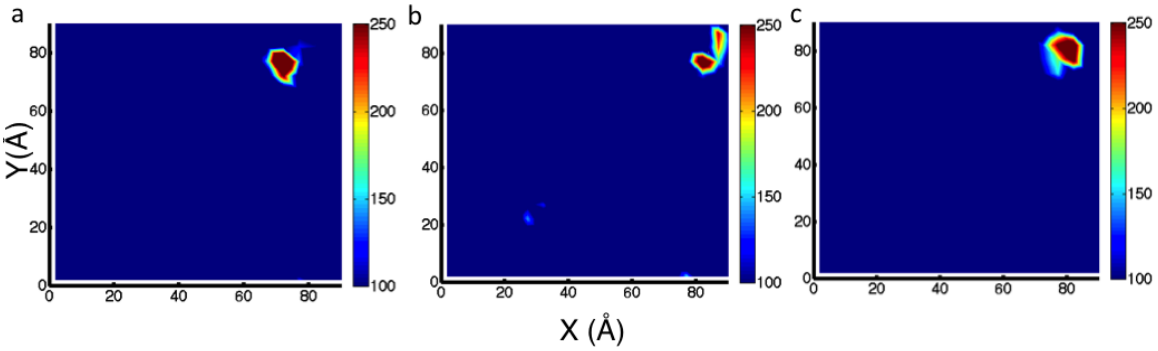

Figure 6.10: Total number of water molecules present in the alkyl region between (a) 225-250ns, (b) 250-275ns and (c) 275-300ns of the the SA simulation. Color bar denotes number of water, X and Y axis, bilayer axis.

Chapter 7: Thesis Summary

The objective of this work was to (a) develop CG models that are both transferable, and account for solvent and changes in dielectric medium; and (b) use the developed models to investigate a variety of processes including the role of dipole interactions in peptide folding, ordered aggregation, membrane properties and membrane induced peptide folding.

Chapter 2 describes the development of a minimalistic peptide model with the inclusion of dipoles in the backbone bead. Its use in studying folding of simple peptide design patterns is discussed. We found that the presence of BB dipoles increase cooperativity in the folding process, and helical conformations are more stabilized by dipoles than β-strands. Chapter 3 describes the use of the developed model in studying peptide aggregation, both in explicit water solvent and at hydrophobic-hydrophilic interface. Based on our studies, the presence of dipoles, not hydrophobicity play a key role in aggregation observed at hydrophobic interfaces. This study is a prelude to studying membrane-peptide interactions and the use of the peptide model in different environments

In Chapter 4, our lipid model is introduced, we use two typical membrane lipids, POPS and POPC as model lipids. Our developed model captures better structural,

dynamic and thermodynamic properties of the bilayer than similar existing models. We also discuss the use of the peptide model described in chapter 2, with the developed lipid model. Due to improvements in bilayer properties, we were able to capture membrane induced peptide folding of an anticancer peptide, SVS-1. This suggests that our developed model can be used to explore folding of similar antimicrobial peptides.

In Chapter 5, we discuss the role of ions in modulating membrane properties. By simply changing the size of monovalent ions, we observed difference in binding modes. Some of the observed binding modes lead to domain formation in lipid mixtures of POPC/POPS. The results presented in this chapter suggests that our model can be used to study large time scale changes in membrane properties and that lipid domains driven by head group interactions can exist in membranes.

Finally, in Chapter 6, we integrate all the tools developed so far, and the information gained from our previous studies on peptide and lipid aggregation (chapter 3 and 5), to understand the effect of SVS-1 concentration on mixed bilayer (1:1 POPC/POPS) and pure POPC. On performing self-assembly simulations, we found that SVS-1 has the potential to insert itself into POPC/POPS membranes, thus forming a polar patch. This suggests that the formation of a pore, albeit possible, is not necessary to see changes in membrane structure or integrity.

We are currently working on understanding the role of curvature in peptide-lipid interaction. Since many experimental studies on AMPs are with unilamellar vesicles, understanding the role of curvature is crucial to make direct comparisons with experimental work. In the future, the peptide model will be extended to model all 20

amino acids and the lipid model, to other lipids of biological significance.

Appendix A: Simulation Parameters

A.0.1 Simulation Parameters

All simulations were carried out using the GROMACS package [242] version 4.5.5, and visualized on VMD [243]. Nose-Hoover thermostat (time constant=1ps) and Parinello-Rahman barostat (time constant=1ps, isothermal compressibility =3e-5 (kJ mol^{-1} $nm^{-3})^{-1}$) were used to keep the temperature and pressure constant at 300K and 1bar. A time step of 5fs was used in all the simulations, and the neighbor list was updated every 10 steps. The long-range electrostatic interactions with periodic boundary conditions (xyz) were calculated by the particle-mesh Ewald method [244]. A global dielectric constant of 2.5 was used. The LINCS algorithm [245] was used to constraint the bonds of the water molecules (between the central CG site and the dipole particles).

Reprinted with permission from [30] Copyright (2014) American Chemical Society.

Bibliography

[1] Siewert J. Marrink, H. Jelger Risselada, Serge Yefimov, D. Peter Tieleman, and Alex H. De Vries. The MARTINI force field: Coarse grained model for biomolecular simulations. *J. Phys. Chem. B*, 111(27):7812–7824, 2007.

[2] Brian M Peters, Mark E Shirtliff, and Mary Ann Jabra-Rizk. Antimicrobial peptides: primeval molecules or future drugs? *PLoS Pathog*, 6(10):e1001067, 2010.

[3] Robert EW Hancock. Peptide antibiotics. *The Lancet*, 349(9049):418–422, 1997.

[4] Stephen H White and William C Wimley. Membrane protein folding and stability: physical principles. *Annu. Rev. Biophys. Biomol. Struct.*, 28(1):319–365, 1999.

[5] S Matysiak and C Clementi. Mapping folding energy landscapes with theory and experiment. *Arch. Biochem. Biophys.*, 468:29–33, 2008.

[6] T Head-Gordon and S Brown. Minimalist models for protein folding and design. *Curr. Opin. Struct. Biol.*, 13:160–167, 2003.

[7] G Bellesia, A I Jewett, and J-E Shea. Sequence periodicity and secondary structure propensity in model proteins. *Prot. Sci.*, 19:141–154, 2009.

[8] J N Onuchic, Z Luthey-Schulten, and P G Wolynes. Theory of protein folding: The energy landscape perspective. *Annu. Rev. Phys. Chem.*, 48:545–600, 1997.

[9] S Takada, Z Luthey-Schulten, and P G Wolynes. Folding dynamics with non-additive forces: A simulation study of a designed helical protein and a random heteropolymer. *J. Chem. Phys.*, 110:11616, 1999.

[10] A Irback, F Sjunnesson, and S Wallin. Three-helix-bundle protein in a ramachandran model. *Proc. Natl. Acad. Sci.*, 97:13614–13618, 2000.

[11] Y Mu and Y Q Gao. Effect of hydrophobic and dipole-dipole interactions on the conformational transitions of a model polypeptide. *J. Chem. Phys.*, 127:105102, 2007.

[12] N-Y Chen, Z-Y Su, and C-Y Mou. Effective potentials for protein folding. *Phys. Rev. Lett.*, 96:078103, 2006.

[13] T Bereau and M Deserno. Generic coarse-grained model for protein folding and aggregation. *J. Chem. Phys*, 130:235106, 2009.

[14] A Liwo, RJ Wawak, HA Scheraga, MR Pincus, and S Rackovsky. Calculation of protein backbone geometry from α-carbon coordinates based on peptide-group dipole alignment. *Protein science*, 2(10):1697–1714, 1993.

[15] Daniel R Ripoll, Jorge A Vila, and Harold A Scheraga. On the orientation of the backbone dipoles in native folds. *Proceedings of the National Academy of Sciences of the United States of America*, 102(21):7559–7564, 2005.

[16] Daniel R. Ripoll, Jorge A. Vila, and Harold A. Scheraga. On the orientation of the backbone dipoles in native folds. *Proc. Natl. Acad. Sci.*, 102(21):7559–7564, 2005.

[17] Lucjan Piela and Harold A. Scheraga. On the multiple-minima problem in the conformational analysis of polypeptides. i. backbone degrees of freedom for a perturbed -helix. *Biopolymers*, 26(S0):S33–S58, 1987.

[18] Daniel R. Ripoll and Harold A. Scheraga. On the multiple-minima problem in the conformational analysis of polypeptides. ii. an electrostatically driven monte carlo method—tests on poly(l-alanine). *Biopolymers*, 27(8):1283–1303, 1988.

[19] R.G. Ashcroft, H.G.L. Coster, and J.R. Smith. The molecular organisation of bimolecular lipid membranes. the dielectric structure of the hydrophilic/hydrophobic interface. *Biochim. Biophys. Acta, Biomembr.*, 643(1):191 – 204, 1981.

[20] Yoshiaki Kimura and Akira Ikegami. Local dielectric properties around polar region of lipid bilayer membranes. *J. Membr. Biol.*, 85(3):225–231, 1985.

[21] B Smit, PAJ Hilbers, K Esselink, LAM Rupert, NM Van Os, and AG Schlijper. Computer simulations of a water/oil interface in the presence of micelles. *Nature*, 348(6302):624–625, 1990.

[22] Wataru Shinoda, Russell DeVane, and Michael L Klein. Zwitterionic lipid assemblies: molecular dynamics studies of monolayers, bilayers, and vesicles using a new coarse grain force field. *The Journal of Physical Chemistry B*, 114(20):6836–6849, 2010.

[23] Alexander P Lyubartsev and Alexander L Rabinovich. Recent development in computer simulations of lipid bilayers. *Soft Matter*, 7(1):25–39, 2011.

[24] Sandra V Bennun, Matthew I Hoopes, Chenyue Xing, and Roland Faller. Coarse-grained modeling of lipids. *Chemistry and physics of lipids*, 159(2):59–66, 2009.

[25] B H Honig, W L Hubbell, and R F Flewelling. Electrostatic interactions in membranes and proteins. *Annu. Rev. Biophys. Biophys. Chem.*, 15(1):163–193, 1986.

[26] Howard Brockman. Dipole potential of lipid membranes. *Chem. Phys. Lipids*, 73(1â“2):57 – 79, 1994.

[27] L Monticelli, S K Kandasamy, X Periole, R G Larson, D P Tieleman, and S-J Marrink. *J. Chem. Theory Comput.*, 4:819–834, 2008.

[28] Mookyung Cheon, Iksoo Chang, and Carol K Hall. Extending the prime model for protein aggregation to all 20 amino acids. *Proteins: Struct., Funct., Bioinf.*, 78(14):2950–2960, 2010.

[29] Yassmine Chebaro, Samuela Pasquali, and Philippe Derreumaux. The coarse-grained opep force field for non-amyloid and amyloid proteins. *J. Phys. Chem. B*, 116(30):8741–8752, 2012.

[30] Sai J. Ganesan and S. Matysiak. Role of backbone dipole interactions in the formation of secondary and supersecondary structures of proteins. *J. Chem. Theory Comput.*, 10(6):2569–2576, 2014.

[31] S Matysiak and P Das. Effect of sequence and solvation on the temperature-pressure conformational landscape of proteinlike heteropolymers. *Phys. Rev. Lett.*, 111:058103, 2013.

[32] W G J Hol, L M Halie, and C Sander. *Nature*, 294:532–536, 1981.

[33] R P Sheridan and L C Allen. The electrostatic potential of the alpha helix. *Biophys. Chem.*, 11:133–136, 1980.

[34] J Aqvist, H Luecke, F A Quiocho, and A Warshel. Dipoles localized at helix termini of proteins stabilize charges. *Proc. Natl. Acad. Sci.*, 88:2026–2030, 1990.

[35] D Sali, M Bycroft, and A R Fersht. Stabilization of protein structure by interaction of α helix dipole with a charged side chain. *Nature*, 335:740–743, 1988.

[36] S Oommachen, J Ren, and M McCallum. Stabilizing helical polyalanine peptides with negative polarity or charge:capping with cysteine. *J. Phys. Chem.*, 112:740–743, 2008.

[37] M W West and M E Hecht. Binary patterning of polar and nonpolar amino acids in the sequences and structures of native proteins. *Prot. Sci.*, 4:2032–2039, 1995.

[38] Semen O. Yesylevskyy, Lars V. Schäfer, Durba Sengupta, and Siewert J. Marrink. Polarizable water model for the coarse-grained martini force field. *PLoS Comput. Biol.*, 6(6):e1000810, 2010.

[39] Thomas E. Creighton. *Proteins: Structures and Molecular Properties (2nd edition)*. W. H. Freeman, 1992.

[40] Walter RP Scott, Philippe H Hünenberger, Ilario G Tironi, Alan E Mark, Salomon R Billeter, Jens Fennen, Andrew E Torda, Thomas Huber, Peter Krüger, and Wilfred F van Gunsteren. The gromos biomolecular simulation program package. *J. Phys. Chem. A*, 103(19):3596–3607, 1999.

[41] Scott Brown, Nicolas J Fawzi, and Teresa Head-Gordon. Coarse-grained sequences for protein folding and design. *Proc. Natl. Acad. Sci.*, 100(19):10712–10717, 2003.

[42] C Narayanan and C L Dias. Hydrophobic interactions and hydrogen bonds in β sheet formation. *J. Chem. Phys.*, 139:115103, 2013.

[43] S. Kamtekar, J. M. Schiffer, H. Xiong, J. M. Babik, and M. H. Hecht. Protein design by binary patterning of polar and nonpolar amino acids. *Science*, 262(5140):1680–1685, 1993.

[44] Yinan Wei, Tun Liu, Stephen L. Sazinsky, David A. Moffet, István Pelczer, and Michael H. Hecht. Stably folded de novo proteins from a designed combinatorial library. *Prot. Sci.*, 12(1):92–102, 2003.

[45] Sushmita Roy, Gayathri Ratnaswamy, Judith A Boice, Robert Fairman, George McLendon, and Michael H Hecht. A protein designed by binary patterning of polar and nonpolar amino acids displays native-like properties. *J. Am. Chem. Soc.*, 119(23):5302–5306, 1997.

[46] Josh P Kemp and Zheng Yu Chen. Formation of helical states in wormlike polymer chains. *Phys. Rev. Lett.*, 81(18):3880, 1998.

[47] R Aurora and GD Rose. Helix capping. *Prot. Sci.*, 7(1):21, 1998.

[48] Behrouz Forood, Eva J Feliciano, and Krishnan P Nambiar. Stabilization of alpha-helical structures in short peptides via end capping. *Proc. Natl. Acad. Sci.*, 90(3):838–842, 1993.

[49] Andrew J Doig and Robert L Baldwin. N-and c-capping preferences for all 20 amino acids in α-helical peptides. *Prot. Sci.*, 4(7):1325–1336, 1995.

[50] CM Wilmot and JM Thornton. Analysis and prediction of the different types of β-turn in proteins. *J. Mol. Biol.*, 203(1):221–232, 1988.

[51] Alexander V. Efimov. Patterns of loop regions in proteins. *Curr. Opin. Struct. Biol.*, 3(3):379 – 384, 1993.

[52] Michael W. West, Weixun Wang, Jennifer Patterson, Joseph D. Mancias, James R. Beasley, and Michael H. Hecht. De novo amyloid proteins from designed combinatorial libraries. *Proc. Natl. Acad. Sci.*, 96(20):11211–11216, 1999.

[53] N. D. Clarke, C. R. Kissinger, J. Desjarlais, G. L. Gilliland, and C. O. Pabo. Structural studies of the engrailed homeodomain. *Prot. Sci.*, 3(10):1779–1787, 1994.

[54] Valerie Daggett and Alan R Fersht. Is there a unifying mechanism for protein folding? *Trends Biochem. Sci.*, 28(1):18–25, 2003.

[55] Yongjin Zhu, Darwin O. V. Alonso, Kosuke Maki, Cheng-Yen Huang, Steven J. Lahr, Valerie Daggett, Heinrich Roder, William F. DeGrado, and Feng Gai. Ultrafast folding of alpha3d: a de novo designed three-helix bundle protein. *Proc. Natl. Acad. Sci.*, 100(26):15486–15491, 2003.

[56] Benjamin J. Cole and Christopher Bystroff. Alpha helical crossovers favor right-handed supersecondary structures by kinetic trapping: the phone cord effect in protein folding. *Prot. Sci.*, 18(8):1602–1608, 2009.

[57] R P Sheridan, R M Levy, and F R Salemme. α helix dipole model and electrostatic stabilization of 4 α helical proteins. *Proc. Natl. Acad. Sci.*, 79:4545–4549, 1982.

[58] H E Stanger and S H Gellman. Rules for antiparallel, -sheet design: D-pro-gly is superior to l-asn-gly for, -hairpin nucleation. *J. Am. Chem. Soc.*, 120:4236–4237, 1998.

[59] Eva De Alba, Jorge Santoro, Manuel Rico, and M. Angeles Jiménez. De novo design of a monomeric three-stranded antiparallel -sheet. *Prot. Sci.*, 8(4):854–865, 1999.

[60] Samuel H Gellman. Minimal model systems for -sheet secondary structure in proteins. *Curr. Opin. Struct. Biol.*, 2(6):717 – 725, 1998.

[61] Sergei V. Krivov, Stefanie Muff, Amedeo Caflisch, and Martin Karplus. One-dimensional barrier-preserving free-energy projections of a beta-sheet miniprotein: new insights into the folding process. *J. Phys. Chem. B*, 112(29):8701–8714, 2008.

[62] Joanne M. Carr and David J. Wales. Folding pathways and rates for the three-stranded beta-sheet peptide beta3s using discrete path sampling. *J. Phys. Chem. B*, 112(29):8760–8769, 2008.

[63] Giovanni Bellesia and Joan-Emma Shea. Self-assembly of β-sheet forming peptides into chiral fibrillar aggregates. *J. Chem. Phys.*, 126(24):245104, 2007.

[64] Sai J Ganesan and Silvina Matysiak. Interplay between the hydrophobic effect and dipole interactions in peptide aggregation at interfaces. *Phys. Chem. Chem. Phys.*, 2016.

[65] Debra Burdick, Brian Soreghan, Michael Kwon, Joseph Kosmoski, Mary Knauer, Agnes Henschen, J Yates, C Cotman, and C Glabe. Assembly and aggregation properties of synthetic alzheimer's a4/beta amyloid peptide analogs. *J. Biol. Chem.*, 267(1):546–554, 1992.

[66] Eberhard Scherzinger, Annie Sittler, Katja Schweiger, Volker Heiser, Rudi Lurz, Renate Hasenbank, Gillian P Bates, Hans Lehrach, and Erich E Wanker. Self-assembly of polyglutamine-containing huntingtin fragments into amyloid-like fibrils: implications for huntington's disease pathology. *Proc. Natl. Acad. Sci. USA*, 96(8):4604–4609, 1999.

[67] Fabrizio Chiti and Christopher M Dobson. Protein misfolding, functional amyloid, and human disease. *Annu. Rev. Biochem.*, 75:333–366, 2006.

[68] D Thirumalai, DK Klimov, and RI Dima. Emerging ideas on the molecular basis of protein and peptide aggregation. *Curr. Opin. Struct. Biol.*, 13(2):146–159, 2003.

[69] Massimo Stefani and Christopher M Dobson. Protein aggregation and aggregate toxicity: new insights into protein folding, misfolding diseases and biological evolution. *J. Mol. Med.*, 81(11):678–699, 2003.

[70] Christopher M Dobson. Principles of protein folding, misfolding and aggregation. In *Semin. Cell Dev. Biol.*, volume 15, pages 3–16. Elsevier, 2004.

[71] M Fändrich. On the structural definition of amyloid fibrils and other polypeptide aggregates. *Cell. Mol. Life Sci.*, 64(16):2066–2078, 2007.

[72] Shae B Padrick and Andrew D Miranker. Islet amyloid: phase partitioning and secondary nucleation are central to the mechanism of fibrillogenesis. *Biochemistry*, 41(14):4694–4703, 2002.

[73] James D Harper and Peter T Lansbury Jr. Models of amyloid seeding in alzheimer's disease and scrapie: mechanistic truths and physiological consequences of the time-dependent solubility of amyloid proteins. *Annu. Rev. Biochem.*, 66(1):385–407, 1997.

[74] Tricia R Serio, Anil G Cashikar, Anthony S Kowal, George J Sawicki, Jahan J Moslehi, Louise Serpell, Morton F Arnsdorf, and Susan L Lindquist. Nucleated conformational conversion and the replication of conformational information by a prion determinant. *Science*, 289(5483):1317–1321, 2000.

[75] Mary P Lambert, AK Barlow, Brett A Chromy, C Edwards, R Freed, M Liosatos, TE Morgan, I Rozovsky, B Trommer, Kirsten L Viola, et al. Diffusible, nonfibrillar ligands derived from aβ1–42 are potent central nervous system neurotoxins. *Proc. Natl. Acad. Sci. USA*, 95(11):6448–6453, 1998.

[76] Natàlia Carulla, Min Zhou, Muriel Arimon, Margarida Gairí, Ernest Giralt, Carol V Robinson, and Christopher M Dobson. Experimental characterization of disordered and ordered aggregates populated during the process of amyloid fibril formation. *Proc. Natl. Acad. Sci. USA*, 106(19):7828–7833, 2009.

[77] Christian Haass and Dennis J Selkoe. Soluble protein oligomers in neurodegeneration: lessons from the alzheimer's amyloid β-peptide. *Nat. Rev. Mol. Cell*

Biol., 8(2):101–112, 2007.

[78] Stefan Auer, Filip Meersman, Christopher M Dobson, and Michele Vendruscolo. A generic mechanism of emergence of amyloid protofilaments from disordered oligomeric aggregates. *PLoS Comput. Biol.*, 4(11):e1000222, 2008.

[79] Min Zhu, Pierre O Souillac, Cristian Ionescu-Zanetti, Sue A Carter, and Anthony L Fink. Surface-catalyzed amyloid fibril formation. *J. Biol. Chem.*, 277(52):50914–50922, 2002.

[80] Riccardo Pellarin and Amedeo Caflisch. Interpreting the aggregation kinetics of amyloid peptides. *J. Mol. Biol.*, 360(4):882–892, 2006.

[81] Hung D Nguyen and Carol K Hall. Molecular dynamics simulations of spontaneous fibril formation by random-coil peptides. *Proc. Natl. Acad. Sci. USA*, 101(46):16180–16185, 2004.

[82] Buyong Ma and Ruth Nussinov. Simulations as analytical tools to understand protein aggregation and predict amyloid conformation. *Curr. Opin. Chem. Biol.*, 10(5):445–452, 2006.

[83] Indu Kheterpal, Shaolian Zhou, Kelsey D Cook, and Ronald Wetzel. Aβ amyloid fibrils possess a core structure highly resistant to hydrogen exchange. *Proc. Natl. Acad. Sci. USA*, 97(25):13597–13601, 2000.

[84] David J Gordon and Stephen C Meredith. Probing the role of backbone hydrogen bonding in β-amyloid fibrils with inhibitor peptides containing ester bonds at alternate positions. *Biochemistry*, 42(2):475–485, 2003.

[85] Anthony W Fitzpatrick, Tuomas PJ Knowles, Christopher A Waudby, Michele Vendruscolo, and Christopher M Dobson. Inversion of the balance between hydrophobic and hydrogen bonding interactions in protein folding and aggregation. *PLoS Comput. Biol.*, 7(10):e1002169, 2011.

[86] Sandeep Kumar, Buyong Ma, Chung-Jung Tsai, Neeti Sinha, and Ruth Nussinov. Folding and binding cascades: dynamic landscapes and population shifts. *Prot. Sci.*, 9(1):10–19, 2000.

[87] Kiril Tsemekhman, Lukasz Goldschmidt, David Eisenberg, and David Baker. Cooperative hydrogen bonding in amyloid formation. *Prot. Sci.*, 16(4):761–764, 2007.

[88] Kathleen A Burke, Elizabeth A Yates, and Justin Legleiter. Biophysical insights into how surfaces, including lipid membranes, modulate protein aggregation related to neurodegeneration. *Front Neurol*, 4:7, 2013.

[89] Alex Morriss-Andrews and Joan-Emma Shea. Kinetic pathways to peptide aggregation on surfaces: The effects of β-sheet propensity and surface attraction. *J. Chem. Phys.*, 136(6):065103, 2012.

[90] Mikhail Y Golovko, Nils J Faergeman, Nelson B Cole, Paula I Castagnet, Robert L Nussbaum, and Eric J Murphy. α-synuclein gene deletion decreases brain palmitate uptake and alters the palmitate metabolism in the absence of α-synuclein palmitate binding. *Biochemistry*, 44(23):8251–8259, 2005.

[91] Stefan Auer, Christopher M Dobson, and Michele Vendruscolo. Characterization of the nucleation barriers for protein aggregation and amyloid formation. *HFSP J.*, 1(2):137–146, 2007.

[92] Sang-Il Kim, Jae-Sung Yi, and Young-Gyu Ko. Amyloid β oligomerization is induced by brain lipid rafts. *J. Cell. Biochem.*, 99(3):878–889, 2006.

[93] Ralph Zahn. The octapeptide repeats in mammalian prion protein constitute a ph-dependent folding and aggregation site. *J. Mol. Biol.*, 334(3):477–488, 2003.

[94] Shuiliang Yu, Shaoman Yin, Nancy Pham, Poki Wong, Shin-Chung Kang, Robert B Petersen, Chaoyang Li, and Man-Sun Sy. Ligand binding promotes prion protein aggregation–role of the octapeptide repeats. *FEBS J.*, 275(22):5564–5575, 2008.

[95] Jacqueline S Capes, Patrick J Kiley, and Alan H Windle. Investigating the effect of ph on the aggregation of two surfactant-like octapeptides. *Langmuir*, 26(8):5637–5644, 2010.

[96] Atanu Biswas, Prashant Kurkute, Batakrishna Jana, Aparna Laskar, and Surajit Ghosh. An amyloid inhibitor octapeptide forms amyloid type fibrous aggregates and affects microtubule motility. *Chem. Commun.*, 50(20):2604–2607, 2014.

[97] Li Fei and Sarah Perrett. New insights into the molecular mechanism of amyloid formation from cysteine scanning. *Prion*, 4(1):9–12, 2010.

[98] Richard M Venable, Yuhong Zhang, Barry J Hardy, and Richard W Pastor. Molecular dynamics simulations of a lipid bilayer and of hexadecane: an investigation of membrane fluidity. *Science*, 262(5131):223–226, 1993.

[99] Ming Miao, Catherine M Bellingham, Richard J Stahl, Eva E Sitarz, Christopher J Lane, and Fred W Keeley. Sequence and structure determinants for the self-aggregation of recombinant polypeptides modeled after human elastin. *J. Biol. Chem.*, 278(49):48553–48562, 2003.

[100] Mikyung Seo, Sarah Rauscher, Régis Pomès, and D Peter Tieleman. Improving internal peptide dynamics in the coarse-grained martini model: toward large-scale simulations of amyloid-and elastin-like peptides. *J. Chem. Theory Comput.*, 8(5):1774–1785, 2012.

[101] Nikolay V Dokholyan. Studies of folding and misfolding using simplified models. *Curr. Opin. Struct. Biol.*, 16(1):79–85, 2006.

[102] Rachel L Redler, David Shirvanyants, Onur Dagliyan, Feng Ding, Doo Nam Kim, Pradeep Kota, Elizabeth A Proctor, Srinivas Ramachandran, Arpit Tandon, and Nikolay V Dokholyan. Computational approaches to understanding protein aggregation in neurodegeneration. *J. Mol. Cell. Biol.*, 6(2):104–115, 2014.

[103] Alex Morriss-Andrews and Joan-Emma Shea. Computational studies of protein aggregation: Methods and applications. *Annu. Rev. Phys. Chem.*, 66(1):643–666, 2015.

[104] Gal Bitan, Marina D Kirkitadze, Aleksey Lomakin, Sabrina S Vollers, George B Benedek, and David B Teplow. Amyloid β-protein (aβ) assembly: Aβ40 and aβ42 oligomerize through distinct pathways. *Proc. Natl. Acad. Sci. USA*, 100(1):330–335, 2003.

[105] Chun Wu and Joan-Emma Shea. Structural similarities and differences between amyloidogenic and non-amyloidogenic islet amyloid polypeptide (iapp) sequences and implications for the dual physiological and pathological activities of these peptides. *PLoS Comput. Biol.*, 9(8):e1003211, 2013.

[106] Sanne Abeln, Michele Vendruscolo, Christopher M Dobson, and Daan Frenkel. A simple lattice model that captures protein folding, aggregation and amyloid formation. *PloS ONE*, 9(1):e85185, 2014.

[107] Hung D Nguyen and Carol K Hall. Molecular dynamics simulations of spontaneous fibril formation by random-coil peptides. *Proc. Natl. Acad. Sci. USA*, 101(46):16180–16185, 2004.

[108] Riccardo Pellarin and Amedeo Caflisch. Interpreting the aggregation kinetics of amyloid peptides. *J. Mol. Biol.*, 360(4):882–892, 2006.

[109] Giovanni Bellesia and Joan-Emma Shea. Effect of beta-sheet propensity on peptide aggregation. *J. Chem. Phys.*, 130(14):145103–145103, 2009.

[110] Sai J. Ganesan and S. Matysiak. Role of backbone dipole interactions in the formation of secondary and supersecondary structures of proteins. *J. Chem. Theory Comput.*, 10(6):2569–2576, 2014.

[111] Slawomir J Grabowski, W Andrzej Sokalski, and Jerzy Leszczynski. The possible covalent nature of nh o hydrogen bonds in formamide dimer and related systems: An ab initio study. *The Journal of Physical Chemistry A*, 110(14):4772–4779, 2006.

[112] ED Isaacs, A Shukla, PM Platzman, DR Hamann, B Barbiellini, and CA Tulk. Compton scattering evidence for covalency of the hydrogen bond in ice. *Journal of Physics and Chemistry of Solids*, 61(3):403–406, 2000.

[113] Henry S Frank and Wen-Yang Wen. Ion-solvent interaction. structural aspects of ion-solvent interaction in aqueous solutions: a suggested picture of water structure. *Discussions of the Faraday Society*, 24:133–140, 1957.

[114] Xiuquan Sun and J Daniel Gezelter. Dipolar ordering in the ripple phases of molecular-scale models of lipid membranes. *J. Phys. Chem. B*, 112(7):1968–1975, 2008.

[115] Michael J Stephen and Joseph P Straley. Physics of liquid crystals. *Rev. Mod. Phys.*, 46(4):617, 1974.

[116] M Cecchini, F Rao, M Seeber, and A Caflisch. Replica exchange molecular dynamics simulations of amyloid peptide aggregation. *J. Chem. Phys.*, 121(21):10748–10756, 2004.

[117] Phuong H Nguyen, Mai Suan Li, Gerhard Stock, John E Straub, and D Thirumalai. Monomer adds to preformed structured oligomers of aβ-peptides by a

two-stage dock–lock mechanism. *Proc. Natl. Acad. Sci. USA*, 104(1):111–116, 2007.

[118] Victoria A Wagoner, Mookyung Cheon, Iksoo Chang, and Carol K Hall. Impact of sequence on the molecular assembly of short amyloid peptides. *Proteins*, 82(7):1469–1483, 2014.

[119] Rebecca Nelson, Michael R Sawaya, Melinda Balbirnie, Anders Ø Madsen, Christian Riekel, Robert Grothe, and David Eisenberg. Structure of the cross-β spine of amyloid-like fibrils. *Nature*, 435(7043):773–778, 2005.

[120] Daniel R Ripoll, Jorge A Vila, and Harold A Scheraga. On the orientation of the backbone dipoles in native folds. *Proc. Natl. Acad. Sci. USA*, 102(21):7559–7564, 2005.

[121] Mookyung Cheon, Iksoo Chang, Sandipan Mohanty, Leila M Luheshi, Christopher M Dobson, Michele Vendruscolo, and Giorgio Favrin. Structural reorganisation and potential toxicity of oligomeric species formed during the assembly of amyloid fibrils. *PLoS Comput. Biol.*, 3(9):e173, 2007.

[122] Trinh Xuan Hoang, Antonio Trovato, Flavio Seno, Jayanth R Banavar, and Amos Maritan. Geometry and symmetry presculpt the free-energy landscape of proteins. *Proc. Natl. Acad. Sci. USA*, 101(21):7960–7964, 2004.

[123] Anthony WP Fitzpatrick, Galia T Debelouchina, Marvin J Bayro, Daniel K Clare, Marc A Caporini, Vikram S Bajaj, Christopher P Jaroniec, Luchun Wang, Vladimir Ladizhansky, Shirley A Müller, et al. Atomic structure and

hierarchical assembly of a cross-β amyloid fibril. *Proc. Natl. Acad. Sci. USA*, 110(14):5468–5473, 2013.

[124] Margaret Sunde, Louise C Serpell, Mark Bartlam, Paul E Fraser, Mark B Pepys, and Colin CF Blake. Common core structure of amyloid fibrils by synchrotron x-ray diffraction. *J. Mol. Biol.*, 273(3):729–739, 1997.

[125] Michael R Sawaya, Shilpa Sambashivan, Rebecca Nelson, Magdalena I Ivanova, Stuart A Sievers, Marcin I Apostol, Michael J Thompson, Melinda Balbirnie, Jed JW Wiltzius, Heather T McFarlane, et al. Atomic structures of amyloid cross-&bgr; spines reveal varied steric zippers. *Nature*, 447(7143):453–457, 2007.

[126] Christopher Aisenbrey, Tomasz Borowik, Roberth Byström, Marcus Bokvist, Fredrick Lindström, Hanna Misiak, Marc-Antoine Sani, and Gerhard Gröbner. How is protein aggregation in amyloidogenic diseases modulated by biological membranes? *Eur. Biophys. J*, 37(3):247–255, 2008.

[127] Herschel M Watkins, Alexis Vallée-Bélisle, Francesco Ricci, Dmitrii E Makarov, and Kevin W Plaxco. Entropic and electrostatic effects on the folding free energy of a surface-attached biomolecule: an experimental and theoretical study. *J. Am. Chem. Soc.*, 134(4):2120–2126, 2012.

[128] Linus Pauling and Robert B Corey. The pleated sheet, a new layer configuration of polypeptide chains. *Proc. Natl. Acad. Sci. USA*, 37(5):251–256, 1951.

[129] Valerie Daggett. α-sheet: the toxic conformer in amyloid diseases? *Acc. Chem. Res.*, 39(9):594–602, 2006.

[130] Roger S Armen, Mari L DeMarco, Darwin OV Alonso, and Valerie Daggett. Pauling and corey's α-pleated sheet structure may define the prefibrillar amyloidogenic intermediate in amyloid disease. *Proc. Natl. Acad. Sci. USA*, 101(32):11622–11627, 2004.

[131] Guido WM Vandermeulen, Kyoung Taek Kim, Zhuo Wang, and Ian Manners. Metallopolymer-peptide conjugates: synthesis and self-assembly of polyferrocenylsilane graft and block copolymers containing a β-sheet forming gly-ala-gly-ala tetrapeptide segment. *Biomacromolecules*, 7(4):1005–1010, 2006.

[132] Mookyung Cheon, Iksoo Chang, and Carol K Hall. Spontaneous formation of twisted aβ 16-22 fibrils in large-scale molecular-dynamics simulations. *Biophys. J.*, 101(10):2493–2501, 2011.

[133] Mookyung Cheon, Iksoo Chang, and Carol K Hall. Influence of temperature on formation of perfect tau fragment fibrils using prime20/dmd simulations. *Protein Sci.*, 21(10):1514–1527, 2012.

[134] Joerg Gsponer and Michele Vendruscolo. Theoretical approaches to protein aggregation. *Protein Pept. Lett.*, 13(3):287–293, 2006.

[135] Yun-Ru Chen and Charles G Glabe. Distinct early folding and aggregation properties of alzheimer amyloid-β peptides aβ40 and aβ42 stable trimer or tetramer formation by aβ42. *J. Biol. Chem.*, 281(34):24414–24422, 2006.

[136] Summer L Bernstein, Nicholas F Dupuis, Noel D Lazo, Thomas Wyttenbach, Margaret M Condron, Gal Bitan, David B Teplow, Joan-Emma Shea, Brandon T Ruotolo, Carol V Robinson, et al. Amyloid-β protein oligomerization and the importance of tetramers and dodecamers in the aetiology of alzheimer's disease. *Nat. Chem.*, 1(4):326–331, 2009.

[137] Peter A Leventis and Sergio Grinstein. The distribution and function of phosphatidylserine in cellular membranes. *Annu. Rev. Biophys.*, 39:407–27, January 2010.

[138] Jens Schamberger and Ronald J Clarke. Hydrophobic ion hydration and the magnitude of the dipole potential. *Biophys. J.*, 82(6):3081–3088, 2002.

[139] V. M. Aguilella and S. M. Bezrukov. Alamethicin channel conductance modified by lipid charge. *Eur. Biophys. J.*, 30(4):233–241, 2001.

[140] Stephen H. White, Alexey S. Ladokhin, Sajith Jayasinghe, and Kalina Hristova. How membranes shape protein structure. *J. Biol. Chem.*, 276(35):32395–32398, 2001.

[141] William C Wimley and Stephen H White. Experimentally determined hydrophobicity scale for proteins at membrane interfaces. *Nat. Struct. Mol. Biol.*, 3(10):842–848, 1996.

[142] Alexey S Ladokhin and Stephen H White. Folding of amphipathic alpha helices on membranes: energetics of helix formation by melittin. *J. Mol. Biol.*, 285(4):1363–1369, 1999.

[143] W C Wimley, K Hristova, A S Ladokhin, L Silvestro, P H Axelsen, and S H White. Folding of beta-sheet membrane proteins: a hydrophobic hexapeptide model. *J. Mol. Biol.*, 277(5):1091–1110, 1998.

[144] Chomdao Sinthuvanich, Ana Salomé Veiga, Kshitij Gupta, Diana Gaspar, Robert Blumenthal, and Joel P Schneider. Anticancer β-hairpin peptides: membrane-induced folding triggers activity. *Journal of the American Chemical Society*, 134(14):6210–6217, 2012.

[145] Edit Matyus, Christian Kandt, and D Peter Tieleman. Computer simulation of antimicrobial peptides. *Curr. Med. Chem.*, 14(26):2789–2798, 2007.

[146] Dejun Lin and Alan Grossfield. Thermodynamics of antimicrobial lipopeptide binding to membranes: origins of affinity and selectivity. *Biophys. J.*, 107(8):1862–1872, 2014.

[147] Dorit Avrahami and Yechiel Shai. Conjugation of a magainin analogue with lipophilic acids controls hydrophobicity, solution assembly, and cell selectivity. *Biochemistry*, 41(7):2254–2263, 2002.

[148] E Gazit, I R Miller, P C Biggin, M S Sansom, and Y Shai. Structure and orientation of the mammalian antibacterial peptide cecropin P1 within phospholipid membranes. *J. Mol. Biol.*, 258(5):860–870, 1996.

[149] Paulo F Almeida, Alexey S Ladokhin, and Stephen H White. Hydrogen-bond energetics drive helix formation in membrane interfaces. *Biochim. Biophys. Acta, Biomembr.*, 1818(2):178–182, 2012.

[150] Ewan M Tytler, GM Anantharamaiah, Donald E Walker, Vinod K Mishra, MN Palgunachari, and Jere P Segrest. Molecular basis for prokaryotic specificity of magainin-induced lysis. *Biochemistry*, 34(13):4393–4401, 1995.

[151] Katsumi Matsuzaki, Kenichi Sugishita, Nobutaka Fujii, and Koichiro Miyajima. Molecular basis for membrane selectivity of an antimicrobial peptide, magainin 2. *Biochemistry*, 34(10):3423–3429, 1995.

[152] Wei Zhao, Tomasz Róg, Andrey A Gurtovenko, Ilpo Vattulainen, and Mikko Karttunen. Atomic-scale structure and electrostatics of anionic palmitoyloleoylphosphatidylglycerol lipid bilayers with Na^+ counterions. *Biophys. J.*, 92(4):1114–24, February 2007.

[153] Alberto Martín-Molina, César Rodríguez-Beas, and Jordi Faraudo. Effect of calcium and magnesium on phosphatidylserine membranes: experiments and all-atomic simulations. *Biophysical journal*, 102(9):2095–2103, 2012.

[154] Jianjun Pan, Xiaolin Cheng, Luca Monticelli, Frederick A Heberle, Norbert Kučerka, D Peter Tieleman, and John Katsaras. The molecular structure of a phosphatidylserine bilayer determined by scattering and molecular dynamics simulations. *Soft Matter*, 10(21):3716–25, June 2014.

[155] Jonathan N Sachs, Hirsh Nanda, Horia I Petrache, and Thomas B Woolf. Changes in phosphatidylcholine headgroup tilt and water order induced by monovalent salts: molecular dynamics simulations. *Biophys. J.*, 86(6):3772–82, June 2004.

[156] Sagar A Pandit and Max L Berkowitz. Molecular dynamics simulation of dipalmitoylphosphatidylserine bilayer with Na^+ counterions. *Biophys. J.*, 82(4):1818–27, April 2002.

[157] John M. Boettcher, Rebecca L. Davis-Harrison, Mary C. Clay, Andrew J. Nieuwkoop, Y. Zenmei Ohkubo, Emad Tajkhorshid, James H. Morrissey, and Chad M. Rienstra. Atomic view of calcium-induced clustering of phosphatidylserine in mixed lipid bilayers. *Biochemistry*, 50(12):2264–2273, 2011.

[158] Parag Mukhopadhyay, Luca Monticelli, and D Peter Tieleman. Molecular dynamics simulation of a palmitoyl-oleoyl phosphatidylserine bilayer with Na^+ counterions and NaCl. *Biophys. J.*, 86(3):1601–1609, 2004.

[159] Sun-Joo Lee, Yuhua Song, and Nathan A Baker. Molecular dynamics simulations of asymmetric NaCl and KCl solutions separated by phosphatidylcholine bilayers: potential drops and structural changes induced by strong Na^+-lipid interactions and finite size effects. *Biophys. J.*, 94(9):3565–3576, 2008.

[160] Manuela Menke, Volker Gerke, and Claudia Steinem. Phosphatidylserine membrane domain clustering induced by annexin A2/S100A10 heterotetramer. *Biochemistry*, 44(46):15296–15303, 2005.

[161] Maddalena Venturoli, Maria Maddalena Sperotto, Marieke Kranenburg, and Berend Smit. Mesoscopic models of biological membranes. *Phys. Rep.*, 437(1-2):1–54, 2006.

[162] Qaiser Waheed, Richard Tjörnhammar, and Olle Edholm. Phase transitions in coarse-grained lipid bilayers containing cholesterol by molecular dynamics simulations. *Biophys. J.*, 103(10):2125–2133, 2012.

[163] H Jelger Risselada and Siewert J Marrink. The molecular face of lipid rafts in model membranes. *Proc. Natl. Acad. Sci. U. S. A.*, 105(45):17367–17372, 2008.

[164] Mark J. Stevens. Coarse-grained simulations of lipid bilayers. *J. Chem. Phys.*, 121(23):11942–11948, 2004.

[165] Zun-Jing Wang and Markus Deserno. Systematic implicit solvent coarse-graining of bilayer membranes: lipid and phase transferability of the force field. *New journal of physics*, 12(9):095004, 2010.

[166] Emily M Curtis and Carol K Hall. Molecular dynamics simulations of dppc bilayers using "lime", a new coarse-grained model. *J. Phys. Chem. B*, 117(17):5019–5030, 2013.

[167] Carlos F Lopez, Steven O Nielsen, Goundla Srinivas, William F DeGrado, and Michael L Klein. Probing membrane insertion activity of antimicrobial polymers via coarse-grain molecular dynamics. *Journal of chemical theory and computation*, 2(3):649–655, 2006.

[168] L Monticelli, S K Kandasamy, X Periole, R G Larson, D P Tieleman, and S J Marrink. The MARTINI coarse grained force field: extension to proteins. *J. Chem. Theory Comput.*, 4:819–834, 2008.

[169] Semen O Yesylevskyy, Lars V Schäfer, Durba Sengupta, and Siewert J Marrink. Polarizable water model for the coarse-grained MARTINI force field. *PLoS Comput. Biol.*, 6(6):e1000810, June 2010.

[170] Pavel A Golubkov, Johnny C Wu, and Pengyu Ren. A transferable coarse-grained model for hydrogen-bonding liquids. *Phys. Chem. Chem. Phys.*, 10(15):2050–2057, 2008.

[171] Diana Gaspar, Ana Salomé Veiga, Chomdao Sinthuvanich, Joel P. Schneider, and Miguel A R B Castanho. Anticancer peptide SVS-1: Efficacy precedes membrane neutralization. *Biochemistry*, 51(32):6263–6265, 2012.

[172] Kshitij Gupta, Hyunbum Jang, Kevin Harlen, Anu Puri, Ruth Nussinov, Joel P. Schneider, and Robert Blumenthal. Mechanism of membrane permeation induced by synthetic β-hairpin peptides. *Biophys. J.*, 105(9):2093–2103, 2013.

[173] Bernard R. Brooks, Robert E. Bruccoleri, Barry D. Olafson, David J. States, S. Swaminathan, and Martin Karplus. CHARMM: A program for macromolecular energy, minimization, and dynamics calculations. *J. Comput. Chem.*, 4(2):187–217, 1983.

[174] Giovanni Bellesia, Andrew Iain Jewett, and Joan Emma Shea. Sequence periodicity and secondary structure propensity in model proteins. *Protein Sci.*, 19(1):141–154, 2010.

[175] Chris Oostenbrink, Alessandra Villa, Lan Mark, and Wilfred Van Gunsteren. A biomolecular force field based on the free enthalpy of hydration and solvation:

The GROMOS force-field parameter sets 53A5 and 53A6. *J. Comput. Chem.*, 25:1656–1676, 2004.

[176] Ryogo Kubo, Mario Yokota, and Sadao Nakajima. Statistical-mechanical theory of irreversible processes. II. Response to thermal disturbance. *J. Phys. Soc. Jpn.*, 12(11):1203–1211, 1957.

[177] Frank Y Jiang, Yann Bouret, and James T Kindt. Molecular dynamics simulations of the lipid bilayer edge. *Biophys. J.*, 87(1):182–192, 2004.

[178] Berk Hess, Carsen Kutzner, David Van Der Spoel, and Erik Lindahl. Gromacs 4: Algorithms for highly efficient, load-balanced, and scalable molecular simulation. *J. Chem. Theory Comput.*, 4(3):435–447, 2008.

[179] Aric A. Hagberg, Daniel A. Schult, and Pieter J. Swart. Exploring network structure, dynamics, and function using NetworkX. In *Proceedings of the 7th Python in Science Conference (SciPy2008)*, pages 11–15, Pasadena, CA USA, August 2008.

[180] Alenka Luzar and David Chandler. Hydrogen-bond kinetics in liquid water. *Nature*, 379(6560):55–57, 1996.

[181] Andrey A. Gurtovenko and Ilpo Vattulainen. Membrane potential and electrostatics of phospholipid bilayers with asymmetric transmembrane distribution of anionic lipids. *J. Phys. Chem. B*, 112(15):4629–4634, 2008.

[182] G Cevc, A Watts, and D Marsh. Titration of the phase transition of phosphatidylserine bilayer membranes. Effects of pH, surface electrostatics, ion binding, and head-group hydration. *Biochemistry*, 20(17):4955–4965, 1981.

[183] Norbert Kučerka, Mu Ping Nieh, and John Katsaras. Fluid phase lipid areas and bilayer thicknesses of commonly used phosphatidylcholines as a function of temperature. *Biochim. Biophys. Acta, Biomembr.*, 1808(11):2761–2771, 2011.

[184] Norbert Kučerka, Yufeng Liu, Nanjun Chu, Horia I. Petrache, Stephanie Tristram-Nagle, and John F. Nagle. Structure of Fully Hydrated Fluid Phase DMPC and DLPC Lipid Bilayers Using X-Ray Scattering from Oriented Multilamellar Arrays and from Unilamellar Vesicles. *Biophys. J.*, 88(4):2626–2637, 2005.

[185] B König, U Dietrich, and G Klose. Hydration and structural properties of mixed lipid/surfactant model membranes. *Langmuir*, 13(3):525–532, 1997.

[186] J M Smaby, M M Momsen, H L Brockman, and R E Brown. Phosphatidylcholine acyl unsaturation modulates the decrease in interfacial elasticity induced by cholesterol. *Biophys. J.*, 73(3):1492–1505, 1997.

[187] Jussi Aittoniemi, Perttu S Niemelä, Marja T Hyvönen, Mikko Karttunen, and Ilpo Vattulainen. Insight into the putative specific interactions between cholesterol, sphingomyelin, and palmitoyl-oleoyl phosphatidylcholine. *Biophys. J.*, 92(4):1125–1137, 2007.

[188] Rainer A Böckmann, Agnieszka Hac, Thomas Heimburg, and Helmut Grubmüller. Effect of sodium chloride on a lipid bilayer. *Biophys. J.*, 85(3):1647–1655, 2003.

[189] Piotr Jurkiewicz, Lukasz Cwiklik, Alžběta Vojtíšková, Pavel Jungwirth, and Martin Hof. Structure, dynamics, and hydration of POPC/POPS bilayers suspended in NaCl, KCl, and CsCl solutions. *Biochim. Biophys. Acta, Biomembr.*, 1818(3):609–616, 2012.

[190] Richard M Venable, Yun Luo, Klaus Gawrisch, Benoît Roux, and Richard W Pastor. Simulations of anionic lipid membranes: Development of interaction-specific ion parameters and validation using nmr data. *The Journal of Physical Chemistry B*, 117(35):10183–10192, 2013.

[191] Ji-Xin Cheng, Sophie Pautot, David A Weitz, and X Sunney Xie. Ordering of water molecules between phospholipid bilayers visualized by coherent anti-stokes raman scattering microscopy. *Proc. Natl. Acad. Sci. U. S. A.*, 100(17):9826–9830, 2003.

[192] Mario Orsi, David Y. Haubertin, Wendy E. Sanderson, and Jonathan W. Essex. A quantitative coarse-grain model for lipid bilayers. *J. Phys. Chem. B*, 112(3):802–815, 2008.

[193] S J Slater, C Ho, F J Taddeo, M B Kelly, and C D Stubbs. Contribution of hydrogen bonding to lipid-lipid interactions in membranes and the role of lipid

order: effects of cholesterol, increased phospholipid unsaturation, and ethanol. *Biochemistry*, 32(14):3714–3721, 1993.

[194] D. V. Zhelev and D. Needham. Tension-stabilized pores in giant vesicles: Determination of pore size and pore line tension. *Biochim. Biophys. Acta, Biomembr.*, 1147(1):89–104, 1993.

[195] Erdem Karatekin, Olivier Sandre, Hicham Guitouni, Nicolas Borghi, Pierre-Henri Puech, and Françoise Brochard-Wyart. Cascades of transient pores in giant vesicles: line tension and transport. *Biophys. J.*, 84(3):1734–1749, 2003.

[196] Satwik Kamtekar, Jarad M Schiffer, Huayu Xiong, Jennifer M Babik, and Michael H Hecht. Protein design by binary patterning of polar and nonpolar amino acids. *Science*, 262(5140):1680–1685, 1993.

[197] Yechiel Shai. Mechanism of the binding, insertion and destabilization of phospholipid bilayer membranes by α-helical antimicrobial and cell non-selective membrane-lytic peptides. *Biochim. Biophys. Acta, Biomembr.*, 1462(1):55–70, 1999.

[198] Stephen H White and William C Wimley. Membrane protein folding and stability: physical principles. *Annu. Rev. Biophys. Biomol. Struct.*, 28(1):319–365, 1999.

[199] Hiromi Sato and Jimmy B Feix. Peptide–membrane interactions and mechanisms of membrane destruction by amphipathic α-helical antimicrobial peptides. *Biochim. Biophys. Acta, Biomembr.*, 1758(9):1245–1256, 2006.

[200] Yuji Ishitsuka, Duy S Pham, Alan J Waring, Robert I Lehrer, and Ka Yee C Lee. Insertion selectivity of antimicrobial peptide protegrin-1 into lipid monolayers: effect of head group electrostatics and tail group packing. *Biochim. Biophys. Acta, Biomembr.*, 1758(9):1450–1460, 2006.

[201] Themis Lazaridis, Yi He, and Lidia Prieto. Membrane interactions and pore formation by the antimicrobial peptide protegrin. *Biophys. J.*, 104(3):633–642, 2013.

[202] Ayyalusamy Ramamoorthy, Sathiah Thennarasu, Anmin Tan, Kiran Gottipati, Sreeja Sreekumar, Deborah L Heyl, Florence YP An, and Charles E Shelburne. Deletion of all cysteines in tachyplesin I abolishes hemolytic activity and retains antimicrobial activity and lipopolysaccharide selective binding. *Biochemistry*, 45(20):6529–6540, 2006.

[203] Henry D Herce and Angel E Garcia. Molecular dynamics simulations suggest a mechanism for translocation of the hiv-1 tat peptide across lipid membranes. *Proc. Natl. Acad. Sci. USA*, 104(52):20805–20810, 2007.

[204] Semen Yesylevskyy, Siewert-Jan Marrink, and Alan E Mark. Alternative mechanisms for the interaction of the cell-penetrating peptides penetratin and the tat peptide with lipid bilayers. *Biophys. J.*, 97(1):40–49, 2009.

[205] Shuhei Kawamoto, Masako Takasu, Takeshi Miyakawa, Ryota Morikawa, Tatsuki Oda, Shiroh Futaki, and Hidemi Nagao. Binding of tat peptides on dopc

and dopg lipid bilayer membrane studied by molecular dynamics simulations. *Mol. Simul.*, 38(5):366–368, 2012.

[206] Kiyotaka Akabori, Kun Huang, Bradley W Treece, Michael S Jablin, Brian Maranville, Arthur Woll, John F Nagle, Angel E Garcia, and Stephanie Tristram-Nagle. Hiv-1 tat membrane interactions probed using x-ray and neutron scattering, cd spectroscopy and md simulations. *Biochim. Biophys. Acta, Biomembr.*, 1838(12):3078–3087, 2014.

[207] Zhe Wu, Qiang Cui, and Arun Yethiraj. A new coarse-grained model for water: the importance of electrostatic interactions. *J. Phys. Chem. B*, 114(32):10524–10529, 2010.

[208] H-L Lee, EA Dubikovskaya, H Hwang, AN Semyonov, H Wang, LR Jones, RJ Twieg, WE Moerner, and PA Wender. Single-molecule motions of oligoarginine transporter conjugates on the plasma membrane of chinese hamster ovary cells. *J. Am. Chem. Soc.*, 130(29):9364–9370, 2008.

[209] Zdzislaw Salamon, Göran Lindblom, and Gordon Tollin. Plasmon-waveguide resonance and impedance spectroscopy studies of the interaction between penetratin and supported lipid bilayer membranes. *Biophys. J.*, 84(3):1796–1807, 2003.

[210] Justin L MacCallum, WF Drew Bennett, and D Peter Tieleman. Distribution of amino acids in a lipid bilayer from computer simulations. *Biophysical journal*, 94(9):3393–3404, 2008.

[211] Donald M Engelman. Membranes are more mosaic than fluid. *Nature*, 438(7068):578–580, 2005.

[212] Erwin London. Insights into lipid raft structure and formation from experiments in model membranes. *Current opinion in structural biology*, 12(4):480–486, 2002.

[213] Jiang Zhao, Jing Wu, Frederick A Heberle, Thalia T Mills, Paul Klawitter, Grace Huang, Greg Costanza, and Gerald W Feigenson. Phase studies of model biomembranes: complex behavior of dspc/dopc/cholesterol. *Biochimica et Biophysica Acta (BBA)-Biomembranes*, 1768(11):2764–2776, 2007.

[214] Jason D Perlmutter and Jonathan N Sachs. Interleaflet interaction and asymmetry in phase separated lipid bilayers: molecular dynamics simulations. *Journal of the American Chemical Society*, 133(17):6563–6577, 2011.

[215] Davit Hakobyan and Andreas Heuer. Phase separation in a lipid/cholesterol system: comparison of coarse-grained and united-atom simulations. *The Journal of Physical Chemistry B*, 117(14):3841–3851, 2013.

[216] Hans Binder and Olaf Zschörnig. The effect of metal cations on the phase behavior and hydration characteristics of phospholipid membranes. *Chemistry and physics of lipids*, 115(1):39–61, 2002.

[217] Helmut Hauser and G Graham Shipley. Interactions of monovalent cations with phosphatidylserine bilayer membranes. *Biochemistry*, 22(9):2171–2178, 1983.

[218] H Hauser and G Graham Shipley. Crystallization of phosphatidylserine bilayers induced by lithium. *Journal of Biological Chemistry*, 256(22):11377–11380, 1981.

[219] HL Casal, HH Mantsch, and H Hauser. Infrared studies of fully hydrated saturated phosphatidylserine bilayers. effect of lithium and calcium. *Biochemistry*, 26(14):4408–4416, 1987.

[220] GP Hartigan. The use of lithium salts in affective disorders. *The British Journal of Psychiatry*, 109(463):810–814, 1963.

[221] Hee-Yong Kim, Bill X Huang, and Arthur A Spector. Phosphatidylserine in the brain: metabolism and function. *Progress in lipid research*, 56:1–18, 2014.

[222] Juyang Huang and Gerald W Feigenson. Monte carlo simulation of lipid mixtures: finding phase separation. *Biophysical journal*, 65(5):1788, 1993.

[223] Stefan Obst and Hans Bradaczek. Molecular dynamics study of the structure and dynamics of the hydration shell of alkaline and alkaline-earth metal cations. *The Journal of Physical Chemistry*, 100(39):15677–15687, 1996.

[224] Shuichi Nosé. A unified formulation of the constant temperature molecular dynamics methods. *J. Chem. Phys.*, 81(1):511–519, 1984.

[225] William Hoover. Canonical dynamics: Equilibrium phase-space distributions. *Phys. Rev. A*, 31(3):1695–1697, 1985.

[226] M. Parrinello and A. Rahman. Polymorphic transitions in single crystals: A new molecular dynamics method. *J. Appl. Phys.*, 52:7182–7190, 1981.

[227] Tom Darden, Darrin York, and Lee Pedersen. Particle mesh Ewald: An N log(N) method for Ewald sums in large systems. *J. Chem. Phys.*, 98(12):10089–10092, 1993.

[228] Berk Hess, Henk Bekker, Herman JC Berendsen, and Johannes G. E. M. Fraaije. LINCS: a linear constraint solver for molecular simulations. *J. Comput. Chem.*, 18(12):1463–1472, 1997.

[229] William J Allen, Justin A Lemkul, and David R Bevan. Gridmat-md: A grid-based membrane analysis tool for use with molecular dynamics. *Journal of computational chemistry*, 30(12):1952–1958, 2009.

[230] Scott E Feller, Richard M Venable, and Richard W Pastor. Computer simulation of a dppc phospholipid bilayer: structural changes as a function of molecular surface area. *Langmuir*, 13(24):6555–6561, 1997.

[231] JJ Lopez Cascales and J Garcia de la Torre. Effect of lithium and sodium ions on a charged membrane of dipalmitoylphosphatidylserine: a study by molecular dynamics simulation. *Biochimica et Biophysica Acta (BBA)-Biomembranes*, 1330(2):145–156, 1997.

[232] Michel Roux and Myer Bloom. Calcium, magnesium, lithium, sodium, and potassium distributions in the headgroup region of binary membranes of phos-

phatidylcholine and phosphatidylserine as seen by deuterium nmr. *Biochemistry*, 29(30):7077–7089, 1990.

[233] Jairajh Mattai, Helmut Hauser, Rudy A Demel, and G Graham Shipley. Interactions of metal ions with phosphatidylserine bilayer membranes: effect of hydrocarbon chain unsaturation. *Biochemistry*, 28(5):2322–2330, 1989.

[234] M Roux and M Bloom. Calcium binding by phosphatidylserine headgroups. deuterium nmr study. *Biophysical journal*, 60(1):38, 1991.

[235] Cornelia G Sinn, Markus Antonietti, and Rumiana Dimova. Binding of calcium to phosphatidylcholine–phosphatidylserine membranes. *Colloids and Surfaces A: Physicochemical and Engineering Aspects*, 282:410–419, 2006.

[236] Kim A Brogden. Antimicrobial peptides: pore formers or metabolic inhibitors in bacteria? *Nature Reviews Microbiology*, 3(3):238–250, 2005.

[237] Manuel N Melo, Rafael Ferre, and Miguel ARB Castanho. Antimicrobial peptides: linking partition, activity and high membrane-bound concentrations. *Nature Reviews Microbiology*, 7(3):245–250, 2009.

[238] James Gumbart, Yi Wang, Alekseij Aksimentiev, Emad Tajkhorshid, and Klaus Schulten. Molecular dynamics simulations of proteins in lipid bilayers. *Current opinion in structural biology*, 15(4):423–431, 2005.

[239] Peter J Bond, John Holyoake, Anthony Ivetac, Syma Khalid, and Mark SP Sansom. Coarse-grained molecular dynamics simulations of membrane proteins and peptides. *Journal of structural biology*, 157(3):593–605, 2007.

[240] Peter J Bond, Daniel L Parton, James F Clark, and Mark SP Sansom. Coarse-grained simulations of the membrane-active antimicrobial peptide maculatin 1.1. *Biophysical journal*, 95(8):3802–3815, 2008.

[241] D Peter Tieleman, Mark SP Sansom, and Herman JC Berendsen. Alamethicin helices in a bilayer and in solution: molecular dynamics simulations. *Biophysical journal*, 76(1):40–49, 1999.

[242] Berk Hess, Carsten Kutzner, David Van Der Spoel, and Erik Lindahl. Gromacs 4: Algorithms for highly efficient, load-balanced, and scalable molecular simulation. *J. Chem. Theory Comput.*, 4(3):435–447, 2008.

[243] William Humphrey, Andrew Dalke, and Klaus Schulten. Vmd: visual molecular dynamics. *J. Mol. Graph.*, 14(1):33–38, 1996.

[244] T Darden, D York, and L Pedersen. Particle mesh ewald: an n log(n) method for ewald sums in large systems. *J. Chem. Phys.*, 98:10089–10092, 1993.

[245] B Hess, H Bekker, H J C Berendsen, and J G E M Fraaije. Lincs: A linear constraint solver for molecular simulations. *J. Comput. Chem.*, 18:33–38, 1997.